This is to certify that the
dissertation entitled

ELASTOHYDRODYNAMIC MODELING AND
MEASUREMENT OF CYLINDER-KIT ASSEMBLY
TRIBOLOGICAL PERFORMANCE

presented by

BOON-KEAT CHUI

has been accepted towards fulfillment
of the requirements for the

PH.D degree in MECHANICAL ENGINEERING

Harold J. Schock
Major Professor's Signature

June 10, 2005

Date

ELASTOHYDRODYNAMIC MODELING AND MEASUREMENT OF CYLINDER-KIT ASSEMBLY TRIBOLOGICAL PERFORMANCE

By

Boon-Keat Chui

A DISSERTATION

Submitted to
Michigan State University
in partial fulfillment of the requirements
for the degree of

DOCTOR OF PHILOSOPHY

Department of Mechanical Engineering

2005

ABSTRACT

ELASTOHYDRODYNAMIC MODELING AND MEASUREMENT OF CYLINDER-KIT ASSEMBLY TRIBOLOGICAL PERFORMANCE

By

Boon-Keat Chui

Engine tribology is becoming a major focus in modern engine development due to the rising demand for engines with lower energy loss and greater durability. The cylinder-kit assembly of an internal combustion engine comprises some of the most crucial components that affect the engine quality in the two areas mentioned above. This dissertation features the computational modeling of the engine cylinder-kit assembly tribology, and its implementation into an existing engine simulation program, CASE, in particular the three-dimensional elastohydrodynamic lubrication (EHL) system at the sliding interfaces of piston/ bore and piston ring/bore.

A numerical methodology is proposed to develop a three-dimensional model of the top compression ring lubrication that accounts for the partially flooded condition coupled with the oil evaporative effect. This model adopts the Reynolds equation, and Greenwood and Tripp equation to solve simultaneously for the hydrodynamic and the asperity contact lubrication, satisfying both the force equilibrium at ring/bore conformability and oil transport continuity. It is capable of accounting for five distinctive conditions that can potentially exist at the ring/bore lubrication interface. The ring/bore wear is also computed. Applying it in a specific diesel engine problem has demonstrated its unique capability in capturing a

tribological phenomenon that fails to be captured by other approaches. A three-dimensional piston EHL model is developed to simulate the dynamics of a piston that allows its structure to deform elastically within the cylinder bore over an engine cycle. Using the finite element approach, the piston solid model is automatically constructed, meshed, and used in the elastic deformation analyses under the variation of boundary loads throughout the engine cycle. In the computation of the hydrodynamic lubricant film pressures, the 3-D finite element domain is transformed locally into a 2-D domain over the entire piston skirt surface area. The calculated lubricant pressures on the thrust and anti-thrust sides of the piston are then adopted as external loads for the entire piston EHL analysis.

Experimental measurements for validating the computational results are performed using a sapphire-bore optical engine system constructed under the collaborative effort between MSU ARES and Mid Michigan Research. The laser-induced-fluorescent (LIF) technique is adopted in the oil film thickness measurement. The IR telemetric technique is employed in the measurement of the piston ring pack gas pressure and the piston temperature using wireless pressure transducers and thermocouples. Comparing and analyzing the prediction and the measurement shows that this computational model is a very practical CAE tool in the engine design and analysis. Further understanding of the engine tribology has been gained, and recommendations for future improvement of the computational and experimental techniques have been proposed.

To my Lord Jesus Christ.

To my wife, my daughter,
and my parents

ACKNOWLEDGEMENTS

This dissertation would not have been completed without the support and assistance of many individuals. I am thankful to all who have contributed, in any way, to the completion of this dissertation. Among them are a few that deserve special appreciation.

I would like to thank my advisor Professor Harold J. Schock, for his guidance, ideas, and supports throughout this work. His sharing of experience and advice are particularly appreciated.

Special mention must be made to Andy and Jeremiah of Mid Michigan Research, Tom and Ed from MSU Engine Research Lab for their technical assistance.

I greatly acknowledge the aid and co-operation of Dr. Mikhail Ejakov from Ford Motor Co. and of Dr. Lawrence Brombolich from Compu-Tec in the development of computational engine system.

Finally, my greatest appreciation and love go to my family and friends. Special thanks goes to my wife for her love, support and prayer. My admiration goes to my daughter for the happiness she brings me. My sincerest thanks go to Jim and Karen for their constant love and prayer.

TABLE OF CONTENTS

LIST OF TABLES

LIST OF FIGURES

KEY TO SYMBOLS AND ABBREVIATIONS

α	Thermal expansion coefficient, Ring twist angle
β	Radius of curvature of asperity summit
β_p	Piston rotation angle
$\dot{\beta}_p$	Piston angular velocity
$\ddot{\beta}_p$	Piston angular acceleration
η	Surface density of asperity peaks
θ	Crank rotation angle
λ	Wave length
μ	Oil viscosity
ν	Poisson's ratio
ρ	Density
σ, R_a	Surface roughness
τ	Shear stress
ψ	Wear rate, Piston tilt angle
ΔA	Instantaneous area of exposure of cylinder bore oil film in combustion chamber
ΔQ_{evap}	Incremental volume of vaporization of oil from the cylinder bore
Δt	Time of exposure of cylinder bore oil film in combustion chamber
$\Phi(\xi)$	Standardized height distribution (Gaussian)
ϕ	Flow factor
ϕ_{rod}	Connecting rod rotation angle
$\dot{\phi}_{rod}$	Connecting rod angular velocity
$\ddot{\phi}_{rod}$	Connecting rod angular acceleration
E_c	Composite elastic modulus
E_1, E_2	Elastic modulus of first and second surfaces
F_a	Lubrication load from asperity contact component
F_{gas}	Load due to gas pressure behind ring

F_h	Load due to hydrodynamic lubrication
F_{LUB}, F_L	Total lubrication load
F_R	Combined applied load
$F_{tension}$	Load from ring tension
H	Material hardness
$P_{cylinder}$	Cylinder gas pressure
P_2	2nd land gas pressure
$T_{cylinder}$	Cylinder gas temperature
U, V, W	Velocity
W_a	Asperity contact load
h	Nominal clearance between two contact surfaces
$h(x), h(x)^*$	Oil film thickness across ring face profile
h_b	Critical oil film thickness at which full boundary lubrication occurs
h_{min}, h_{min}^*	Minimum oil film thickness
h_o	Oil film thickness at the location of $\partial p/\partial x = 0$
$\bar{h}$	Supplied oil film thickness
k	Wear coefficient
m''_{evap}	Evaporative mass flux of vaporized oil
p_a, P_a	Contact pressure from elastically deformed asperity
p_h, p, P_h	Hydrodynamic pressure
$\bar{q}, q$	Lubricant flow rate
t	Time
u	Velocity profile across gap between two sliding surfaces
x_1	Distance of film separation point
EHL	Elastohydrodynamic lubrication
BDC	Bottom dead center
TDC	Top dead center
TRR	Top ring reversal position

F_1	Top contact force (positive on thrust side, negative on antithrust side)
F_2	Bottom contact force (positive on thrust side, negative on antithrust side)
F_3	Lubricant force on thrust side
F_4	Lubricant force on antithrust side
F_5	Friction force at top contact point (positive on thrust side, negative on antithrust side)
F_6	Friction force at bottom contact point (positive on thrust side, negative on antithrust side)
F_7	Lubricant friction force on thrust side
F_8	Lubricant friction force on antithrust side
M_{pin}	Moment developed between piston pin and piston due to friction
P_v	Vertical component of combustion gas pressure load
P_H	Horizontal component of combustion gas pressure load
d_p	piston pin diameter
μ	Coefficient of friction at contact points
m_2	Mass of piston pin
m_3	Mass of piston
m_{rod}	Mass of connecting rod
I_3	Mass moment of inertia of piston, I_{pis}
I_{rod}	Mass moment of inertia of connecting rod
a-f, h, s, u, L_1,L_2, ***R***	Geometrical dimension of piston assembly (refer to Fig. 48)

CHAPTER 1 ENGINE CYLINDER-KIT TRIBOLOGY MODELING

1.1 Introduction

Knowledge in engine tribology is very important to the development of any modern engines that involve mechanism of motions and contact of surfaces. What is tribology? A definition according to Ludema [66] is as follows:

> *Tribology is the 'ology' or science of 'tribein.' The word comes from the same greek root as 'tribulation.' A faithful translation defines tribology as the study of rubbing or sliding. The modern and broadest meaning is the study of friction, lubrication and wear.*

Indeed, engine tribology contributes to a very wide area of disciplines in engine study, ranging from fluid mechanics, heat and mass transfer, solid mechanics, to engine kinematics and dynamics. The understanding of engine tribology explains what happens at the frictional components of a reciprocating internal combustion engine (bearings, piston assembly and valve train), or at the rotational components (shafts and bearing) of a turbo engine or an electric motor in a hybrid engine, in which these components dictate predominantly the efficiency of the engines. Engine tribology long has been researched by those pioneering in engine development decades ago in an effort to look for more efficient engines that run smoother, faster and longer. In recent years, a methodology that emerges to the focus of engine tribology research is the computational method. The advanced computer has motivated many to employ

this methodology since it has been proven effective and useful. For instance, at the availability of computationally systematized calculation methods, a significant amount of lead time and cost have been reduced for a new vehicle from the conceptual phase to the production phase. Many alternative designs can be evaluated through computational models before one is selected, and this means that the selected design is often much more likely to be right and to perform better in operations.

1.2 Motivations and Objectives

Despite many advantages of the computational method, it must be integrated into a broader engineering strategy that allows a computational product to be verified and gives confidence to engineers, which is suggested by Parker [81] as a principle in the verified predictive technique. A computational model development often starts with experimental measurement, particularly where a phenomenon of interest is intricate. From collected data, an insight into what is actually happening is useful, if not crucial, in the proposition and construction of a mathematical model. Then, the developed model can be run to simulate results to be compared with other measurements, a procedure that often leads to improvements to the model in an attempt to minimize the discrepancy between its predictions and experimental observations. Likewise, gradual application of the model to real design situations provides feedback from engine running experience, which increases the reliability of its use and further allows its scope to be extended.

Making use of the advantages of the computational method, this dissertation attempts to establish a comprehensive engine simulation system that has its predictions being verified or validated to some extent by experimental observations. This dissertation focuses on the development, implementation and application of engine tribological systems that simulates elastohydrodynamic lubrication (EHL), friction and wear at the frictional cylinder-kit components (piston skirt and ring) and a distorted cylinder bore under conscientious backing from experimental observations. The ultimate goal is to produce a comprehensive tool that computationally integrates the complex coupled systems in a cylinder-kit system (piston, piston rings, cylinder bore, and connecting rod) in order that a complete engine design analysis can be simulated efficiently in the aspect of computational effort and time. Three specific major accomplishments achieved in this dissertation are:

1.) Implemented the models of three-dimensional piston ring/liner wear, and three-dimensional piston skirt elastohydrodynamic lubrication into an existing engine simulation program;

2.) Constructed and implemented a ring/bore lubrication model that accounts for the partially flooded analysis coupled with the oil vaporization analysis; and

3.) Validated the predicted results with measurements obtained from an optically accessible engine system.

1.3 Synopsis

An existing engine simulation program, CASE, under the sponsorship of Mid Michigan Research, is used as a foundation for the development of the new computational models of this dissertation. The CASE system is a computational program used for the analysis and design of pistons, rings and other cylinder-kit components. The existing CASE system allows for the computations of phenomena such as piston ring pack gas flow, ring/liner lubrication, piston and ring dynamics for an entire engine cycle. Although it is a rather complete and stand-alone program, it does allow new models to be implemented into it for better and more accurate prediction of engine performance. More detailed background of the CASE system is given in Chapter 2.

As piston rings slide against the bore liner in an engine, lubricated contact occurs either in the regime of hydrodynamic, boundary or mixed. The boundary contact induced from the asperity-to-asperity interaction between two surfaces often causes surface deformation or wear. An improved piston assembly lubrication and wear model has been developed and implemented into the CASE system. This model couples the physics of the ring/liner conformation and lubrication, and the effect of surface microstructures in the determination of piston ring/liner wear. Potential lubrication conditions due to partially flooded condition are also simulated using a starved lubrication model which numerically derives the hydrodynamic film separation points through the satisfaction of global load equilibrium and flow continuity at the ring/bore interface. More detail of the implementation and application of this model will be given in Chapter 3.

Starved or partially flooded condition is commonly believed as a factor in determining the piston ring/bore lubrication. The ring/bore interface is not always filled with lubricant entirely - known as fully flooded condition, despite being assumed to be such in many early lubrication models. As a top compression ring slides towards the bottom dead center (BDC), a lubricant film is left behind on the cylinder bore and exposed to the combustion chamber environment. Any heat and mass transfer process, such as oil vaporization, will reduce the cylinder bore film thickness. As the top compression ring returns during compressing strokes (towards TDC), the bore oil film thickness becomes the supplied lubricant that enters the leading edge of the ring face, and dictates flooded condition at the interface. Hence, there is a very close interaction between the heat and mass transfer process and the lubrication process at the ring/bore interface. A model of oil vaporization that accounts for local variation of boundary conditions, in particular the bore temperature, distortion and hydrodynamic pressure across the bore surface, is developed and implemented into CASE to account for the temperature-induced starved condition at the piston ring/bore lubricated interface. More detail of this model will be presented in Chapter 4.

Piston modeling using the computational approach has become a vital part in today's automotive engine development. In recent years, due to the advancement of computer technology, more efforts have been seen in the development of 3-D piston models, which are used in simulating the complicated system of dynamics and tribology at the piston/cylinder-bore conjunction. Chapter 5 presents a newly developed/stand-alone piston software that is capable

of automatically constructing a 3-D finite element (FE) piston model and solving the coupled interaction between the piston skirt elastohydrodynamic and the piston trajectory over the entire four-stroke engine cycle. The software is also implemented with FEA solvers to solve for the thermal and mechanical distortion, and the elastohydrodynamic lubrication of the piston. Comparison of some of the computation results with another commercial software is also presented for the purpose of validation. The application of this software is conducted over an operating engine to demonstrate its capability in predicting the piston skirt lubrication and dynamics. More detail of its implementation and application will be given in this chapter.

An experimental rig is constructed under the joint-effort between Mid Michigan Research and Michigan State University to perform experimental measurements of the cylinder-kit oil film thickness, temperature and pressures. The experiment rig includes an optically accessible engine and optic devices constructed in line with the technique of laser-induced fluorescence (LIF). Measured and predicted results are compared and analyzed. More description of this experiment will be provided in Chapter 6.

Finally, the conclusions and recommendations of this present dissertation will be given in Chapter 7 to summarize how each part is significant to this present work, with conclusions from the integration of all parts.

1.4 Literature Review

Many previous works have been committed to the study of the tribology at the piston ring/bore and the piston/bore interfaces in internal combustion engines because of the common belief that the tribological interaction at these two primary interfaces accounts for a substantial influence on engine efficiency [7,22,51,89,92,94].

Over the past few decades, much research has been conducted to study and understand the lubricating mechanism at the piston ring/bore sliding interface. This is a very challenging field because an engine, in particular the IC engine, can operate over a huge range of operating conditions. Fully flooded or starved conditions in hydrodynamic, boundary or mixed regimes can all potentially occur in a running engine, and each posts a unique problem. Thus, researchers in piston ring pack lubrication often conduct studies by imposing constraints through limiting experimental operating ranges or through imposing specific assumptions.

Early diligent efforts to investigate the basic principles of the piston ring lubrication, both experimental and theoretical, have been reported between the year of 1925 and 1944, according to Grice [46]. Many early mathematical models adopted the Reynolds equation, named after Osborne Reynolds. He derived this equation from the full expression of hydrodynamics, known as the Navier-Stokes equation [11,12,50,38], to solve for the hydrodynamic lubrication at the sliding interaction between piston rings and cylinder bore. Many assumptions were made to simplify their models, such as the use of the laminar and Newtonian flow for the

lubricant and the smooth surface contact. Castleman found good correlation of his theoretical prediction of piston ring lubrication with results of an experiment in which the comparison of the oil film thickness was taken at distances away from the dead centers of piston stroke [15]. He concluded that the hydrodynamic theory was sufficient to represent the piston ring lubrication even without the boundary lubrication analysis. Eilon and Sanders [27] also developed a hydrodynamic theory of the piston ring, without the squeeze film term, derived from their experimental study of the lubrication between a single-ring piston assembly and a cylinder. Their experimental apparatus consists of a stationary piston and a reciprocating liner. Reasonably good agreement between the theoretical and experimental results was claimed.

Without the squeeze film effect, it is rather inadequate to represent the piston ring lubrication at the dead centers of the piston stroke. Here, sliding velocity is zero and surface metallic contact and the squeeze film effect are important. An improved hydrodynamic model was introduced by Furuhama [39] along with his experimental effort [40], in which an apparatus like that of Eilon and Sanders was adopted. He showed the importance of the inclusion of the squeeze film effect in the hydrodynamic theory, in particular at the TDC and BDC where the piston ring velocity is zero. Furuhama et al. [41] later introduced another method for measuring the oil film thickness through the monitoring of the variation of ring endgap. Furuhama's finding was also supported by Lloyd's work [65] in which he solved the Reynolds equation numerically using a computerized system. The advancement of calculation speed with the computer allowed him to conduct

design evaluation of the piston ring profile on the cyclic lubrication performance. His effort was followed by Baker et al. [5] in the investigation of the piston ring design on the piston ring performance. They also recommended the importance of including the non-uniform nature of circumferential ring loading and multi-ring pack system for the piston ring lubrication modeling.

In contrast to early experiments that adopted the stationary ring and reciprocating cylinder liner, various experimental approaches that conducted direct measurement of piston ring in an operating engine have been reported in the 1970's. Wing et al. [127] reported a technique using inductive proximity transducers and thermocouple in the measurement of oil film thickness and temperature of the piston rings, in order to investigate the thermal and vibrational behavior of piston rings, which was considered a better approach for understanding the piston ring lubrication mechanism. Hamilton et al. [48] also reported a technique of oil film thickness measurement using capacitance transducers. Unlike Wing's method, which had the measuring devices mounted on the ring that caused instability in the signal output, Hamilton et al. [49] had the capacitance transducers mounted at several locations on the cylinder liner to measure the oil film thickness of the ring pack that passes the locations. They later introduced a numerical solution to the classical Reynolds equation assuming Reynolds' boundary conditions and fully flooded condition [49]. When compared with experimental measurements, the numerical solution overpredicted the oil film thickness, which led to the belief that the oil starvation could potentially exist in the piston ring lubrication.

The rapid development of computerized technology in 1970's has motivated greater and more extensive efforts in piston ring tribological study. More complicated analyses have been incorporated into the piston ring lubrication model. Ting and Mayer [117,118,119] presented a comprehensive ring pack model that simulates a more inclusive piston ring pack analysis, which includes ring pack gas flow dynamics using the orifice volume method, mixed lubrication, and adhesive cylinder bore wear. Ring elastic characteristics were also considered. Ruddy et al. [96,97,98] also conducted a comprehensive study of piston ring lubrication by including the effects of ring orientation due to twisting and dynamics, and the thermal distortion and wear of ring groove.

Later works by Allen [1], Brown and Hamilton [9], Dowson et al. [23], and Moore and Hamilton [75] suggested the importance of including the starvation effect in piston ring lubrication as proven by their improved results in comparison with the experimental measurements. Dowson et al. [23] extends the starved lubrication analysis to a multi-ring pack computation. Their work showed how the starved lubrication of a ring is related to the deposition of oil transport from the preceding ring in a ring pack. They also concluded that because of the flow continuity of the inter-ring oil transport mechanism, the minimum oil film thickness experienced by all the ring must be similar under the criteria that the ring face profiles did not have extreme difference.

A review by McGeehan [73] has suggested that hydrodynamic lubrication predominantly contributes to the overall friction at the ring/bore interface except at

the TDC and BDC, which implies that mixed lubrication is basically not an important factor to be considered in the ring/bore lubrication analysis. In spite of that, many studies have recognized that surface roughness plays important roles in lubrication, in particular in the regime of mixed lubrication as it has the same order of magnitude as the average film thickness. In efforts to account for the global effect of surface roughness, an averaging technique has been adopted because most engineering surfaces display random characteristics. Among these, Patir and Cheng (PC) [82] have proposed an average flow model using pressure and shear flow factors as correction terms in an equation derived from the classical Reynolds equation to solve for slider bearing equation on two rough surfaces that slide against each other. Greenwood and Tripp (GT) [45] derived a theoretical model that describes the asperity contact of two nominally flat rough surfaces.

A mixed lubrication model for the piston ring was presented by Rohde [93], which studied the sharing of frictional contact load between the hydrodynamic and the asperity contact pressure. Adopting the PC-averaged Reynolds equation and the GT asperity model, the effects of surface topography on lubrication and friction were studied in detail. His results showed the dominance of asperity contact at TDC and BDC, and that contributes to high friction loss. He concluded that the piston ring power loss is dependent on the surface topography and lubricant properties, in particular during low engine speeds. A more specific application of the PC and GT models was conducted by Ruddy et al. [98] on modeling a twin-land oil control ring lubrication.

Another important aspect of the piston ring lubrication is the elastic characteristics of the piston ring in cylinder bore. Dowson et al. [24] discussed the necessity to consider both the rigid body motion and the rate of change of the local elastic compression of piston rings in the squeeze film contribution to hydrodynamic action in the piston ring/bore interaction. Elastohydrodynamic action was suggested as an important factor to the tribological performance of the piston seal, particularly near TDC, in which it is believed to be able to improve the oil film thickness at TDC and reduce the friction. Sun [106] attempted to solve the nonuniform contact problem of the ring/bore conformability using the elastic theory incorporated with the thermal elasticity. He also [105] proposed a generic computational solution for the slider lubrication problems. His solution addressed the complicated issues of the flow continuity and the attachment/detachment of the oil film on the sliding interface.

The introduction of optical measurement technology with the application of the laser beam has motivated several efforts in the measurement of piston ring oil film thickness. Ting in 1980 [120] published his first effort in piston ring oil film thickness measurement using a laser fluorescence technique, and demonstrated the potential of this technique to achieve more precise measurement. Unlike the conventional electronic method, the optical technique does not require any device to be mounted on the piston ring or the cylinder liner and therefore reduces the possibility of external disturbance on the piston ring dynamics and lubrication to minimal. Another advantage is that it allows visual observation to be done instantaneously during the measurement, and therefore allows more insight into

piston ring dynamics and lubrication. However, due to the pulsing effect in most laser source, the calibration of the laser source needs to be done carefully in order to achieve accurate measurement as reported by Hoult [52]. Richardson [90] applied an improved optical technique, which is called the laser induced fluorescence (LIF) technique, in the measurement of piston ring oil film thickness along with his modeling effort in piston ring lubrication. Other efforts using LIF are found in the works of Takiguchi [109], Nakayama et al. [78] and Suguru [103]. Other measurement techniques are also found in Liu et al. [64], who conducted the measurement of the piston ring lubrication under motoring conditions using Eddy Current Sensors which are mounted on the liner; and in Takiguchi et al. [110], who adopted the capacitance method to measure a three-ring pack oil film thickness in an operating diesel engine.

The need to consider the circumferential variation in the ring/bore interaction have been raised by McGeehan [74] and Ting [121]. McGeehan, in his survey of the mechanical design factors that affect engine oil consumption, pointed out the significance of bore distortion on oil transport along the ring/bore interface. Ting's review of piston ring tribology indicated that the ring/bore conformability is an important issue to be considered in the piston ring lubrication.

Grice [46] developed a three-dimensional model of piston ring lubrication that accounts for the circumferential variations that exist between a piston ring and cylinder liner, in order to represent accurately the physics of the oil transport, friction and lubrication film thickness more correctly. His theoretical prediction was

compared with experimental measurement using an improved capacitance technique that allows both the oil film thickness and friction to be measured.

With the major advancement of computers in the 1990's, computational time is becoming a lesser issue in piston ring modeling. Hence, several computational models of three-dimensional piston ring lubrication analysis have been reported. Ma et al. [68,69,70,71,72] reported a comprehensive three-dimensional model of piston ring lubrication that accounts for bore out-of-roundness and starved condition. The full Reynolds equation is solved cyclically using the finite difference method. The lubricant was assumed to be incompressible, Newtonian and laminar. However, the model did not consider surface roughness effect and secondary ring motion. They concluded that the piston ring performance, energy loss and oil transportation are significantly affected by the bore shape and the ring lateral displacement. Their starved lubrication analysis shows that the relative ring locations in a ring pack are crucial in determining the oil availability to the rings of a ring pack, and starved condition was observed on all compression rings throughout the engine cycle, in which only 10-40% of ring face is regularly covered with the full oil film. In addition, the increase of the bore temperature seems to be able to reduce the average power loss and the net oil transport of the ring pack. A significant degree of agreement was claimed by Ma et al. in their comparison with other earlier measurement by Brown and Hamilton [9], and Hamilton and More [49]. Tian et al. [112,113,114,115,116] also presented a similar piston ring pack system that displays similar capability as Ma et al., but with the addition of mixed lubrication

and more application efforts in production IC engines along with validation from their experimental measurements.

Ejakov [34] developed a three-dimensional piston ring pack lubrication model that accounts for load sharing between the hydrodynamic and asperity contact pressure at the ring/bore interface. His earlier work in the three-dimensional modeling of the piston ring twist [28,32] was incorporated with this model along with a piston dynamic model [13] to illustrate the importance of including ring/bore conformability, piston ring twisting motion, piston tilting motion and bore distortion in the analyses of piston ring pack lubrication, gas flow and dynamics.

Despite the continuous effort in the three-dimensional modeling, the two-dimensional theory is still being employed in several piston ring lubrication studies [131,132,102,104] that usually combine the theoretical prediction and experimental measurement because the two-dimensional theory is still reliable. This is supported by many previous reports, provided the non-uniformability of the ring/bore interaction is small. The efforts to include the non-Newtonian behavior of the lubricant in the piston ring lubrication model were also reported by Taylor et al. [111] and Tian et al. [113], in which the shear thinning effect on the lubricant viscosity is considered in additional to the temperature effect.

The efforts in mixed lubrication lead to the implementation of the ring/bore wear modeling [18,19,20,21,61,66,84,119]. A fundamental law of adhesive wear discussed by J. F. Archard [2] has been adopted or modified in the calculation of

surface wear at the sliding interaction between the piston assemblies and the cylinder bore. Chung et al. [21] developed a mathematical model to predict fire ring wear using a linear relationship between ring wear and the contact friction, and compared the results with experimental measurement [101]. Pint et al. [89] developed a model for 3-D piston ring wear accounting for surface topography on the ring wear using Abott FireStone Curve (AFC) to account for surface change affected by wear. Chui [20,21] conducted continuous cyclic analysis on piston ring wear and its effect on oil consumption. Different piston ring wear measurement techniques have been reported [6,53,67,101,123]. Among those is the radioactive tracer technique that provides higher accuracy of ring wear measurement, which has radioactive material implanted on the piston ring surface, and any amount surface loss can be detected. Barkman [6], Treuhaft et al. [123] and Schneider et al. [101] conducted the piston ring wear measurement using the radioactive tracer technique. A general agreement on the predicted and the measured ring wear is in the transient progression of the piston ring wear rate, in which the piston ring wear rate begins with high value initially and decreases in an exponential trend, and ultimately reaches a steady state value.

Compared with piston ring tribology, the efforts in piston tribology appears to be very few. One reason is that the complexity to solve for the Reynolds equation on the piston skirt surface area requires substantial amount of computational power. The difficulty of solving for the three-dimensional solid deformation is another reason.

Early piston models were developed primarily to investigate piston dynamics and its impact on the cylinder bore that results in engine noise and vibration, in particular the piston slap phenomenon. The effects from the lubrication and the piston skirt elasticity on the piston dynamics were either not considered or assumed insignificant [25,37,47,60,76,79,85,99,108,124]. Nevertheless, valuable insights and principles obtained from these studies regarding piston dynamics have contributed to the later efforts that attempt to couple lubrication and piston flexibility into piston dynamics. By considering the piston skirt lubrication and flexibility, the real physics of an operating piston can be better represented. Knoll and Peekan [58], Li et al. [63], Goenka [44], Keribar [56] introduced piston skirt hydrodynamic lubrication models that solve for the two dimensional Reynolds equation over the piston skirt surface.

The elastic characteristic of the thin piston skirt was first considered in the piston dynamic analysis by Li [62]. Integrating piston skirt elastic behavior into hydrodynamic lubrication has formed the elastohydrodynamic lubrication analysis, which is considered by most of the recent efforts [26,57,59,80,129,133,134]. Among these, Oh et al. [80], Zhu et al. [133, 134] and Dursunkaya et al. [26] have contributed to solving the elastic deformation of the piston using the finite element method and its integration in the calculation of piston trajectory and lubrication as functions of crank angle. The finite element piston analysis is solved by a separate finite element solver, and the calculated coefficient matrices or the compliance matrices are input into the piston model of lubrication and dynamics in order to reduce computational time. However, this approach may result in the lost

of crucial numerical information because of the transfer of the nodal information between the 3-D FE model and the 2-D piston skirt lubrication model that each posses different mesh resolution, particularly when there exist sharp gradients between two nodes.

CHAPTER 2 COMPUTATIONAL ENGINE MODEL - CASE

The Cylinder-kit Analysis System for Engines (CASE) [13,14], under the sponsorship of Mid Michigan Research, is used as the foundation for the development of the new computational models proposed in this present work. This engine simulator has been well established for years and consistently undergoes refinement at the availability of the advancement of engine technology and knowledge. CASE can be used in the engine design and analysis tasks for given engine configurations and operating conditions. The parametric study for engine optimization can be performed at a relatively time and cost efficient manner by using CASE. CASE also has flexibility for other computational routines to be incorporated or integrated for more complicated engine simulation. The reliability of CASE has been proven from its application and development in a number of practical applications in the past [8,18,19,20,21,28,29,30,31,32,33,34, 35,84,85].

CASE contains coupled computational models of several important systems in an internal combustion engine. Those systems are the piston and piston ring dynamics, heat and mass transfer system of engine working fluids, the solid mechanics, and the tribology at the relative sliding surface contacts - piston skirt/liner and piston ring/liner, which are indeed some of the most crucial engine systems that affect the overall engine performance, fuel and oil consumption, and engine durability. The basic structure of CASE is shown in Fig. 1. TWIST, RING and PISTON are three main CASE programs and the integration of them allows a

complete engine simulation even though each can be run independently for a more specific engine analysis. The highlighted engine subsystems in Fig. 1 are the focus of this dissertation, where improvement and implementation of these models were conducted.

The RING and TWIST programs contain computational models for the piston ring system while PISTON applies to the piston system. The piston ring system, as shown in Fig. 2, includes the piston ring dynamics within piston grooves, both axial and twisting behaviors under the influence of inertia force, combustion gas pressure, and ring tension. It also includes the gas dynamics of the combustion gas trapped within the piston ring pack, and the piston ring tribology such as ring/liner lubrication, friction loss due to viscous lubricant and asperities contact, and mechanical wear. The gas dynamics analysis is a two-dimensional model that computes the average gas flow across the inner piston ring grooves and lands using the orifice volume approach without considering the circumferential variation at the ring/bore interface. However, when the ring twist analysis is included, because of its three-dimensional nature that affects the gas flow path dimension axially and circumferentially, the gas flow analysis can be considered three-dimensional. The piston ring lubrication model is a three-dimensional model that accounts for both axial and circumferential variations of boundary conditions namely bore distortion, bore temperature, piston tilting and ring twisting. In addition, it accounts for the mixed lubrication of the piston ring that comprises the Reynolds hydrodynamic and asperity contact lubrication. The latest

developments contributed from this dissertation are three-dimensional ring/bore wear, partially flooded lubrication (oil transportation) and oil vaporization.

The piston system, as shown in Fig. 3, includes piston dynamics in the engine cylinder under the influence of combustion gas pressure, inertia and contact forces from friction and lubrication. In addition, it also includes piston solid mechanics and piston skirt/liner tribology elastohydrodynamic lubrication.

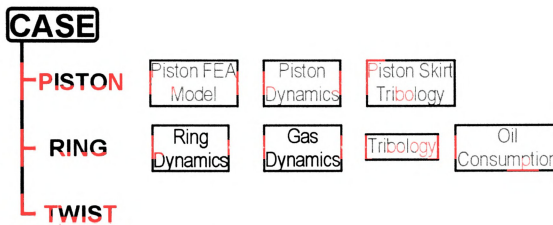

FIGURE 1. CASE structure

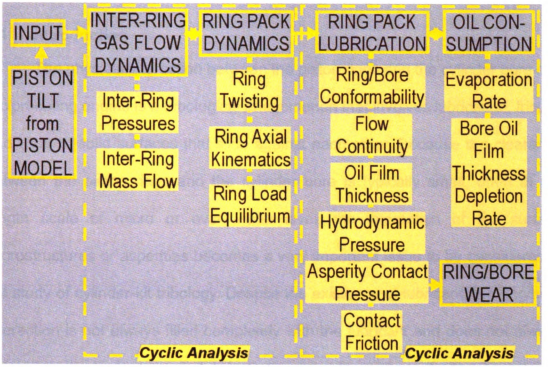

FIGURE 2. Piston ring program structure

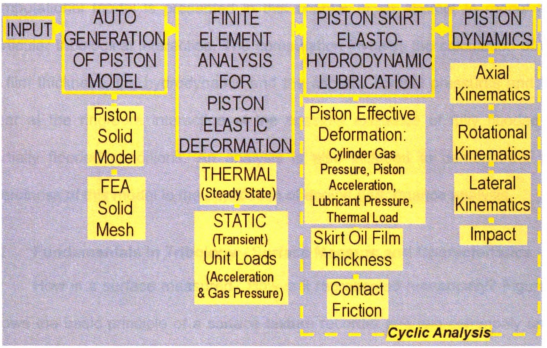

FIGURE 3. Piston program structure

CHAPTER 3 RING/BORE LUBRICATION AND WEAR

3.1 Introduction

The physical interaction between the piston rings and the cylinder bore of a reciprocating engine is a tribological phenomenon that involves lubrication, friction and wear of solid surfaces that slide against each other. Because the clearance between the piston rings and the cylinder bore is typically small, often at the length scale of micro or even nano level, the interaction of the surface microstructures or asperities becomes a very important issue to be considered in the study of cylinder-kit tribology. Despite the existence of lubricant, the ring/bore interaction is not always filled completely with the lubricant and does not always operate in the hydrodynamic lubrication regime. In contrary, it often operates in the mixed lubrication regime and in the partially flooded condition. A computational model is presented in this chapter in an attempt to model this particular tribological interaction. The computation involves the calculation of the oil film thickness, the hydrodynamic and the asperity contact pressures and the wear at the ring/bore interaction at the possible existence of fully flooded or partially flooded conditions. An analysis is also included to demonstrate the usefulness of this model in the application of engine performance analysis.

3.2 Fundamentals in Tribology - Surface Measure and Characteristics

How is a surface measured? How is it represented numerically? Figure 4 shows the basic principle of a surface texture recorder and two commonly used measured parameters - surface roughness and waviness. A real surface is often complicated enough that two parameters are not sufficient to characterize it

accurately. In order to represent a surface more correctly, additional statistical parameters such as the probability density of asperities, the standard deviation of the roughness height, the surface profile across surface lay (distinctly directional pattern due to machining) and asperity peak radius, are used. In many applications, surfaces are often considered to have a symmetrical Gaussian distribution in their microstructure (asperities), even though asymmetrical characteristics do exist in common surfaces. A asymmetrical surface is more complicated and involves additional surface parameters such as skewness - measure of the symmetry of the profile about the mean line, and kurtosis - measure of shape (sharpness) of the amplitude distribution curve. The use of statistical parameters, along with magnitudal parameters, allows a surface to be represented mathematically for the tribological calculation.

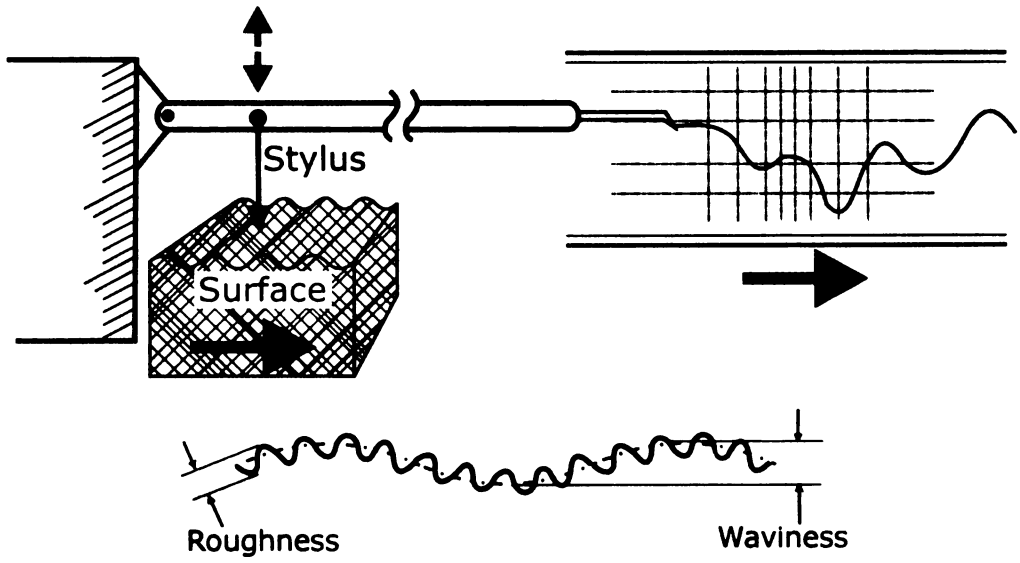

FIGURE 4. Surface measurement and parameters

This equation requires statistical parameters of surface that can be obtained from high precision surface measurement equipment [107]. Statistical parameters can better represent a surface since most surfaces have complex and randomly distributed geometrical structure. In engine studies, although most interacting components begin with engineered surfaces, the tribological impact after thousands of engine cycles may turn the surfaces into unpredictable forms. The statistical parameters used in this equation are the combined surface roughness σ, the summit density η, and the estimated average asperity peak radius of curvature β.

3.3 Wear Mechanism

When two surfaces come into a motion contact, a certain degree of wear is expected to occur. There are three common types of wear mechanism - corrosive, abrasive and adhesive. Corrosive wear occurs when there is a chemical interaction of surface-to-surface or the surface-to-contact medium at the surface interaction. Abrasive wear occurs when a surface interaction results in the existence of hard abrasive substances or particles (being able to be felt abrasive to the fingers) in a system, and the interaction causes scratching on a worn surface. Adhesive wear occurs when a surface interaction produces none or negligible abrasive substances and there is a tangential sliding of one clean surface over another [66]. In adhesive wear, the existence of oxides and adsorbed substances are usually ignored. Due to the complexity of accounting for chemical interaction as well as the particle-to-particle and particle-to-surface interaction, corrosion and abrasion are not considered in the calculation of ring/bore wear.

3.3.1 Adhesive Equation for Piston Ring/Bore Wear

According to Archad, the wear rate of two surfaces that slide against one another is proportional to the sliding speed and normal contact load and inversely proportional to the surface hardness. Eq. 1 shows the wear equation

$$\psi = k\left(\frac{W_a V}{H}\right) \tag{1}$$

where the wear coefficient, k, is determined empirical solution. In the application to the sliding interaction at piston rings and cylinder bore conjunction, the applied load, W_a, is the boundary contact force at the interaction; the sliding speed, V, is the magnitude of the piston reciprocating velocity, and the material hardness, H, is the combined hardness of the interacting surfaces. The finding of all the terms in Eq. (1) for a piston ring/bore wear analysis is rather a straightforward process except the applied load term, W_a. The finding of W_a requires the solving of the elastohydrodynamic mechanism between piston rings and cylinder bore, which is presented in the following section.

3.4 Piston Ring/Bore Lubrication

Piston rings operate under a wide range of lubrication conditions. In most cases, the lubrication can be categorized into the regime of hydrodynamic, boundary and the mixture of the two, according to the popularly adopted Stribeck Diagram. However, in the application of a reciprocating piston assembly system, two potential oil transport conditions can emerge at the ring/bore interface, resulting in a total of five lubrication conditions, which are

1.)Fully flooded hydrodynamic,

2.)Partially flooded hydrodynamic,

3.)Fully flooded mixed,

4.)Partially flooded mixed, and

5.)Full boundary.

The chance of occurrence for each lubrication condition depends on the relative magnitude difference between surface roughness and ring/bore clearance, and the sufficiency of oil for lubrication.

3.4.1 Hydrodynamic Lubrication

At the piston ring/bore sliding interface, oil film that separates the contact surfaces is generated by pressures arising from the shearing of a viscous lubricant during their relative sliding motion. This kind of pressure is often defined as hydrodynamic pressure. One of the most extensively used formulas to solve for the ring/bore hydrodynamic lubrication is the Reynolds equation. The classical Reynolds equation is as follows:

$$\frac{\partial}{\partial x}\left(\frac{h^3}{\mu}\frac{\partial p}{\partial x}\right)+\frac{\partial}{\partial z}\left(\frac{h^3}{\mu}\frac{\partial p}{\partial z}\right) = 6U\frac{\partial h}{\partial x}+6W\frac{\partial h}{\partial z}+12V \qquad (2)$$

Consider the nature of piston ring/bore lubrication. The axial velocity of the ring, U, is much higher than the rotational velocity, W; and at the ring/bore clearance, the circumferential dimension is much larger than the radial dimension.

Thus,

$$\frac{\partial p}{\partial x} \gg \frac{\partial p}{\partial z} \tag{3}$$

This unique circumstance allows the ring/bore lubrication to be considered as a quasi-1D problem, which can be represented by the following equation:

$$\frac{\partial}{\partial x}\frac{h^3}{\mu}\frac{\partial p}{\partial x} = 6U\frac{\partial h}{\partial x} + 12\frac{dh_{min}}{dt} \tag{4}$$

where $\frac{dh_{min}}{dt} = V$ is the squeeze film motion.

In spite of its proven reliability, the classical Reynolds equation is inadequate to address the effect of surface microstructure on hydrodynamic pressure development because the surface roughness is not being considered. For this reason, efforts to include surface roughness effect have been carried out [82,83,122], among which the modified Reynolds model developed by Patir and Cheng [82] has been widely adopted in the effort of modeling piston assembly lubrication. The governing equation for the model is actually a modified version of the classical Reynolds equation but is defined in terms of shear and pressure flow factors, which are functions of the ratio between surface roughness and nominal clearance between two surfaces. It can be applied into the partially lubricated interaction between two rough surfaces when the effect of roughness is most crucial [82]. The partial differential equation is

$$\frac{\partial}{\partial x}\left(\phi_x \frac{h^3}{\mu}\frac{\partial p}{\partial x}\right) = 6U\frac{\partial h}{\partial x} - 6U\sigma\frac{\partial \phi_s}{\partial x} + 12\frac{dh_{min}}{dt} \tag{5}$$

where according to Zhu et al. [133], the simplified pressure and stress flow factors are

$$\phi_x = \left[1 - \left(\frac{\sigma}{h}\right)^2\right]^2 \tag{6}$$

$$\phi_s = \frac{\sigma}{h} \tag{7}$$

3.4.2 Hydrodynamic Boundary Conditions

In general, the solution of piston ring/bore lubrication can be obtained using one of three types of pressure boundary conditions: 1.) Sommerfeld, 2.)Half-Sommerfeld, and 3.)Reynolds conditions. The boundary conditions of each type can be expressed as the following respectively:

$$\begin{aligned} p &= p_1 \quad at \quad x = 0 \\ p &= p_2 \quad at \quad x = b \end{aligned} \tag{8}$$

$$\begin{aligned} p &= p_1 \quad at \quad x = 0 \\ p &= p_2 \quad at \quad x = b \\ p &= 0 \quad if \quad p(x) < 0 \end{aligned} \tag{9}$$

$$\begin{aligned} p = p_1 \quad and \quad \frac{dp}{dx} = 0 \quad at \quad x = 0 \\ p = p_2 \quad at \quad x = b \end{aligned} \tag{10}$$

The boundary conditions are illustrated in Figure 5.

Despite some shortcomings [119,90], Half-Sommerfeld boundary conditions are the simplest to apply [90] and are widely used for obtaining a reasonable hydrodynamic load estimation [119].

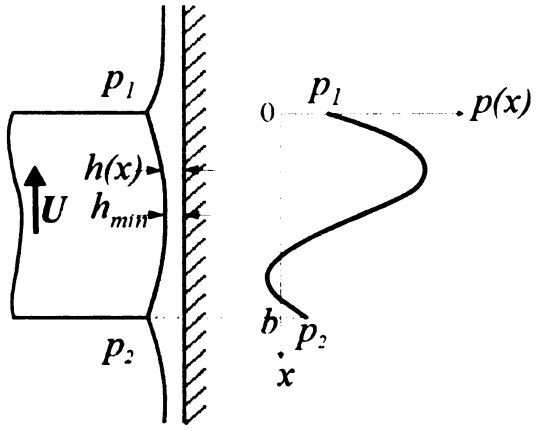

(a) Full-Sommerfeld Boundary Conditions

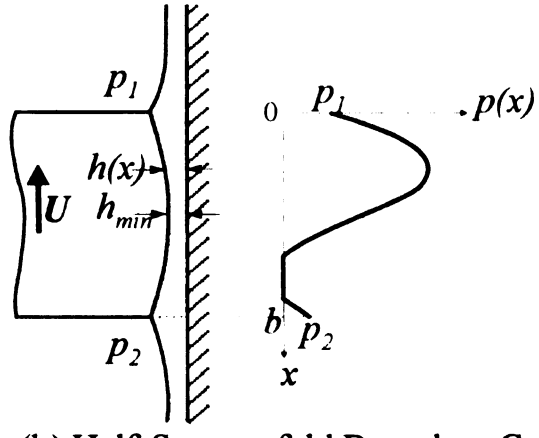

(b) Half-Sommerfeld Boundary Conditions

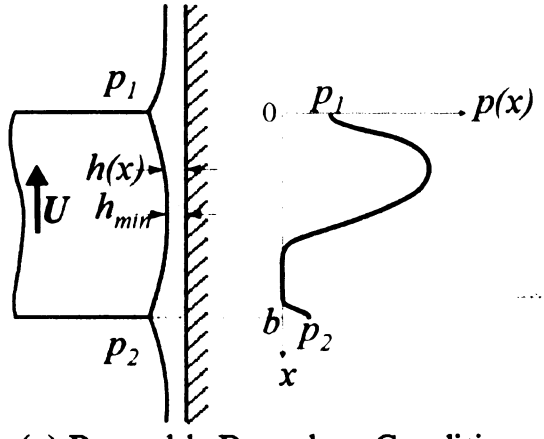

(c) Reynolds Boundary Conditions

FIGURE 5. Lubricant film pressure and boundary conditions

3.4.3 Boundary Lubrication

Carefully defined surface microstructure data is particularly important in the computation of the boundary lubrication that occurs at the sliding contact between two surfaces. The theoretical model describing the asperity contact of two nominally flat rough surfaces has been proposed by Greenwood and Tripp [45]. Even though the deformation of asperities can be both elastic and inelastic, it is noted that plastic deformation is usually permanent after a surface has been run-in, and it is reasonable to assume that an elastic effect is likely to be experienced predominantly by surfaces during steady state operation. The nominal pressure per unit area carried by asperities at the contact derived from the model is expressed as:

$$p_a(h) = \frac{16\sqrt{2}\pi}{15}(\sigma\beta\eta)^2 E_c \sqrt{\frac{\sigma}{\beta}} F_{\frac{5}{2}}\left(\frac{h}{\sigma}\right) \tag{11}$$

where

$$E_c = \frac{1}{\left(\frac{1-\nu_1^{\,2}}{E_1} + \frac{1-\nu_2^{\,2}}{E_2}\right)} \tag{12}$$

$$F_{\frac{5}{2}}\left(\frac{h}{\sigma}\right) = \frac{1}{\sqrt{2\pi}} \int_{\frac{h}{\sigma}}^{\infty} \left(\xi - \frac{h}{\sigma}\right)^{\frac{5}{2}} \Phi(\xi) d\xi \tag{13}$$

Integrating the nominal pressure in Eq. 11 over the surface in the sliding direction results in the load carried by the asperities:

$$W = \frac{16\sqrt{2}\pi}{15}(\sigma\beta\eta)^2 E_c \sqrt{\frac{\sigma}{\beta}} \int F_{\frac{5}{2}}\left(\frac{h}{\sigma}\right) dx. \tag{14}$$

3.4.4 Ring Elastic Conformability in a Distorted Bore

In the piston ring/bore wear modeling, the primary step involved is solving a non-linear elastic ring conformability inside a distorted cylinder bore. The details of this computation can be found in the mixed lubrication model implemented in RING [13]. The piston ring is discretized into a 91-node 3-D finite element beam model (see Fig. 6), and the displacement of each node relative to the bore surface is solved iteratively without violating the spatial constraints within the piston groove and distorted bore under the tensional load from the piston ring stiffness, the gas pressure load from behind the piston ring, coupled with the hydrodynamic film pressure load from the lubricant and the contact load from the elastically deformed asperities.

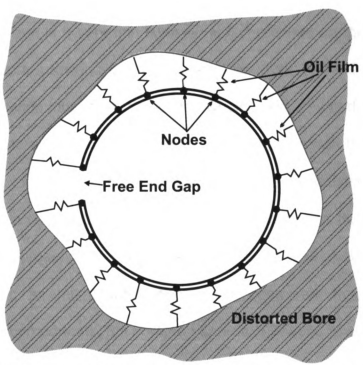

FIGURE 6. Ring structural FEA and oil lubrication model [34]

Convergence of the solution is reached when global and local force equilibrium is achieved at each node with a predicted nodal displacement or clearance between the node and the cylinder bore. Under the assumption of fully flooded ring pack lubrication, the clearance is also the same as the oil film thickness.

3.5 Starved Lubrication Analysis for the Top Ring

For a multi-ring piston assembly, the fully flooded assumption is applied to all piston rings underneath the top ring. In comparison to other piston rings, the top compression ring is one of the least lubricated components in the cylinder-kit assembly of an internal combustion engine due to its direct interaction with combustion gas and extreme temperature environment. When the top compression ring slides towards the top dead center, the only supplied oil to the front of the ring face is a very thin layer of oil film retained on the cylinder bore, which is left from previous downward strokes. This thin oil layer is often insufficient to provide lubrication across the whole ring/bore interface. A common approach in modeling a partially flooded lubrication is through the finding of the film attachment location on the ring face where the hydrodynamic interaction begins to develop so that the criteria of load equilibrium and flow continuity are satisfied. This approach is found to be useful for a hydrodynamic lubrication model. However, for mixed lubrication, which comprises hydrodynamic and asperity contact components, the common approach needed to be modified. This paper introduces a modified computational approach that is capable of addressing five possible lubrication conditions encountered by the top ring during its upstroke

motion. The three-dimensional feature of this model allows a variation of boundary conditions to be considered across bore circumference and axial direction.

This present work introduces a computational methodology to deal with the problem of the mixed ring/bore lubrication by modifying an existing three-dimensional lubrication model of CASE [13]. The existing model assumes that the top compression ring is always operating under a fully flooded condition. This assumption will not be appropriate in the analysis for severe engine operating conditions such as high engine speeds and loads when ring/bore metallic contact and oil starvation is more likely to occur. To account for the potential occurrence of partially flooded condition at the top ring/bore interaction due to film breakdown during its upstroke movement, a numerical scheme is introduced. This numerical scheme has the capability to account for five distinct lubrication conditions at the top ring/bore interface. For secondary rings in a multi-ring pack system, the fully flooded assumption is applied.

3.5.1 Numerical Scheme

Developing a computational model for the top piston ring/bore lubrication requires the solving of multiple systems prior to it, although in reality, all these systems operate almost simultaneously. For this reason, several existing routines of CASE are employed, which are the gas dynamics and the fully flooded ring/bore lubrication. The flow chart in Figure 7 shows the fundamental structure of the piston ring/bore lubrication system.

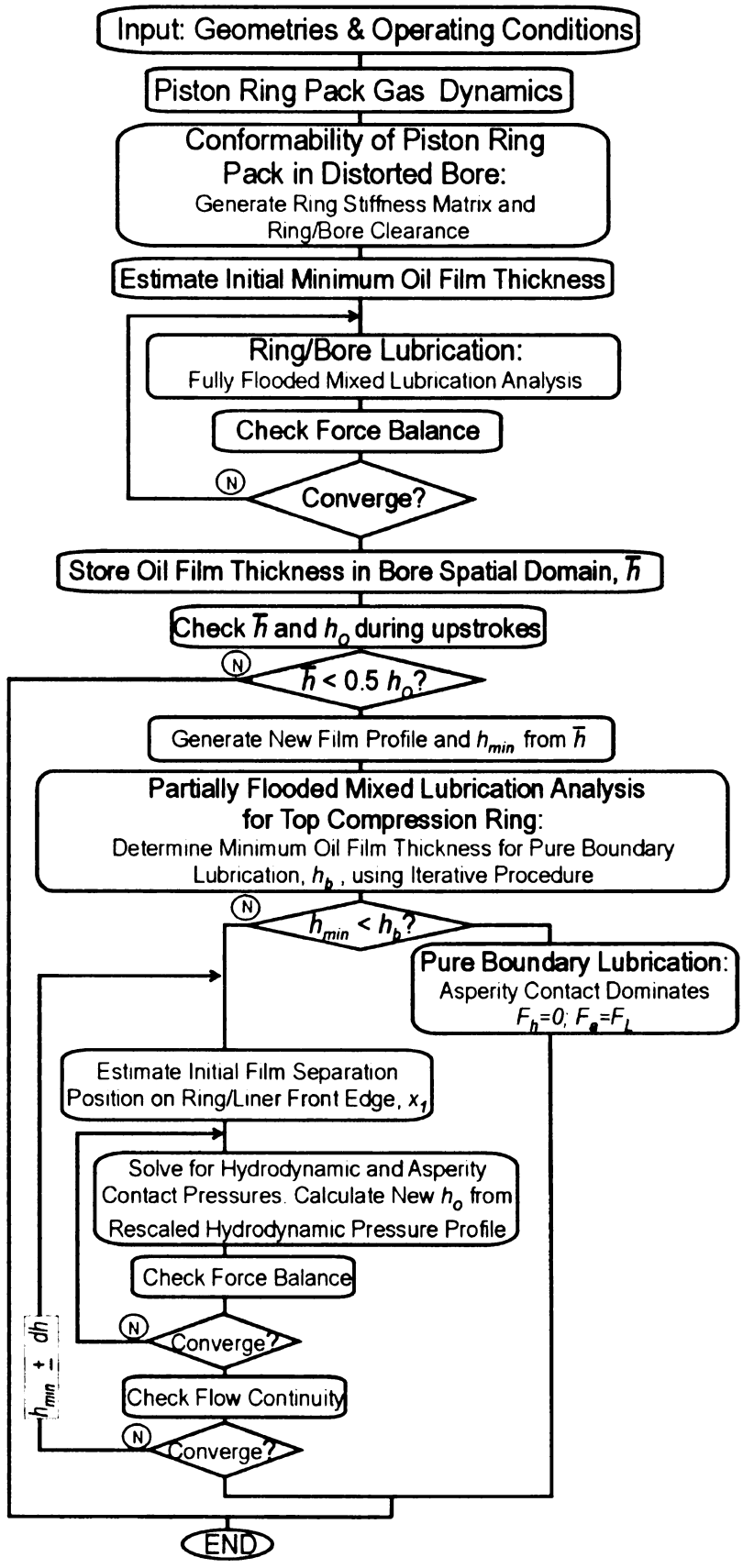

FIGURE 7. Program flow diagram

The input for the model consists of engine geometrical parameters, material properties and boundary conditions of a studied engine analysis. Because this is a three-dimensional model, the variation along the circumference of a piston assembly such as piston secondary motion (tilt), bore asymmetric distortion and temperature, piston ovality, and ring twisting motion can be included in the input. The gas flow of the piston ring pack coupled with piston ring dynamics is first computed to generate ring pack pressures for all piston grooves and lands for an entire engine cycle. The data in every crank angle increment are stored to serve as boundary conditions for other analyses in successive simulation loops.

In a new engine cycle loop, the ring/bore conformability analysis is conducted. Each piston ring is modeled as a three-dimensional FEA beam model with 91 nodes along the circumference. A standard FEA method is employed to obtain the ring stiffness and displacement of a piston ring in a distorted bore, first under dry lubrication, meaning that each piston ring node is only loaded with ring tension from input and previously calculated groove pressure forces [13,34]. The ring stiffness is due to the structural deflection of the ring as it is fitted into a distorted bore. Then, at the same time interval, the fully flooded lubricated ring/ bore interaction is conducted where the lubricant film loads due to hydrodynamics and asperity contact are generated. The dry and lubricated ring/bore interactions are coupled to obtain the effective clearance between piston rings and cylinder bore using an iterative procedure. Under the fully flooded assumption, the effective clearance is the same as the oil film thickness. The effective clearance is

obtained when the nodal force equilibrium state at the ring/bore interface is achieved by satisfying

$$F_R = F_{LUB} \tag{15}$$

where

$$F_R = F_{gas} + F_{tension} \tag{16}$$

and

$$F_R = F_h + F_a + F_r \tag{17}$$

If the computational time step falls within the piston upstroke duration (compression and exhaust strokes) the partially flooded lubrication for the top ring will be performed. During downstroke, the top ring is assumed to have sufficient supplied lubricant from the inter-ring region to operate in a fully flooded condition. During its upward movement, the lubricant supplied to the top ring/bore interface can be obtained either from an input of film thickness of the cylinder bore, or from the stored film thickness left from the top ring in its previous downward stroke. The ability to include measured bore film thickness is particularly useful in the application for the optical engine system constructed under the collaborative effort between MSU and MMR, at the Michigan State University Engine Research Laboratory, where ring/bore oil film thickness over the entire bore surface can be measured using the Laser-Induced Fluorescence (LIF) method. When the top compression ring slides towards top dead center, it can encounter five possible

lubrication conditions. If the supplied oil film thickness, $\bar{h}$, is less than twice the oil film thickness, h_o, which is obtained from the initial fully flooded hydrodynamic pressure solution, the partially flooded analysis will be performed; otherwise, the fully flooded analysis computed previously applies. If the oil film thickness at the top ring/bore interface, $h(x)$, is much higher than the combined surface roughness, R_a, the asperity pressure may be reduced to zero and the hydrodynamic component becomes the sole lubrication load. Figure 8 shows the schematic representation of fully and partially flooded hydrodynamic lubrications. If $h(x)$ is comparable with R_a, the mixed lubrication condition will occur since both hydrodynamic and asperity contact components are involved in sharing the lubrication load. Figure 9 shows the schematic representation of fully and partially flooded mixed lubrication.

In dealing with the partially flooded mixed condition as opposed to the partially flooded hydrodynamic condition, an additional parameter is needed to determine if pure boundary lubrication exists. As the new oil film profile $h(x)^*$ across the ring/bore interface is now a function of $\bar{h}$ in the partially flooded condition, one must obtain a critical minimum oil film thickness, h_b, at which asperity contact completely dominates in the lubrication load. The value of h_b is obtained using an iterative procedure by solving Eq. (11) until load equilibrium is satisfied according to Eq. (15). When the new minimum oil film thickness, $h_{min}{}^*$, is less than h_b, pure boundary lubrication is assumed, as shown in Figure 10. The

oil film thickness will be set to h_b in order not to violate Eq. (15). It is to be noted here that when surface roughness is involved in a lubrication analysis, the oil film thickness definition is no longer referred to as the thickness of lubricant, but the nominal clearance between two surfaces, which is the combination of lubricant thickness and asperity height.

When the partially flooded lubrication occurs, a solution needs to reach numerical convergence for two constraints: the lubricant flow continuity in the oil transport mechanism, and the load equilibrium in the elastohydrodynamic interaction at each node of the top ring. For this reason, every cross section of piston ring face across the circumference is discretized into 101 nodes as shown in Fig. 11. This implies that at every time interval the computational task will involve a total number of 91 x 101 nodes. The moving grid method is applied on the meshing of the ring oil film profile in which the first node is always at the estimated separation point, x_1, of the oil film from the ring face. It is to be noted here that the film profile at the ring/bore interface is dependent on the ring face profile and its orientation under the influence of ring twisting (α) and piston tilting (ψ) motion, and oil film is assumed to attach constantly to the cylinder bore. The 101-node resolution is essential for the solving of Reynolds hydrodynamic pressure through Eq. (5) as well as for the flow continuity analysis.

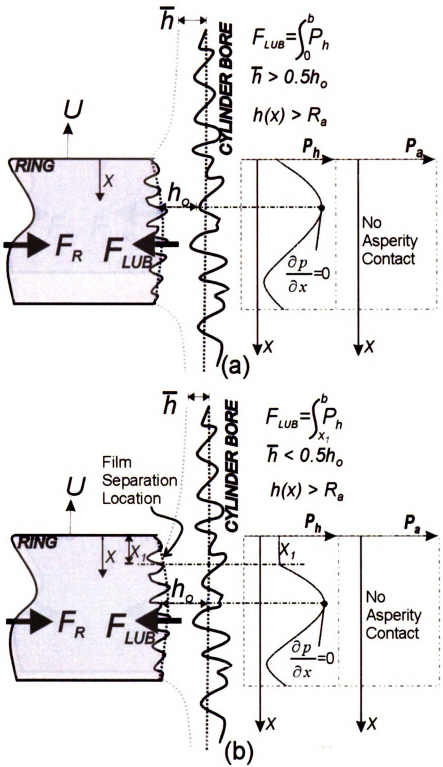

FIGURE 8. (a) Fully and (b) partially flooded hydrodynamic lubrication

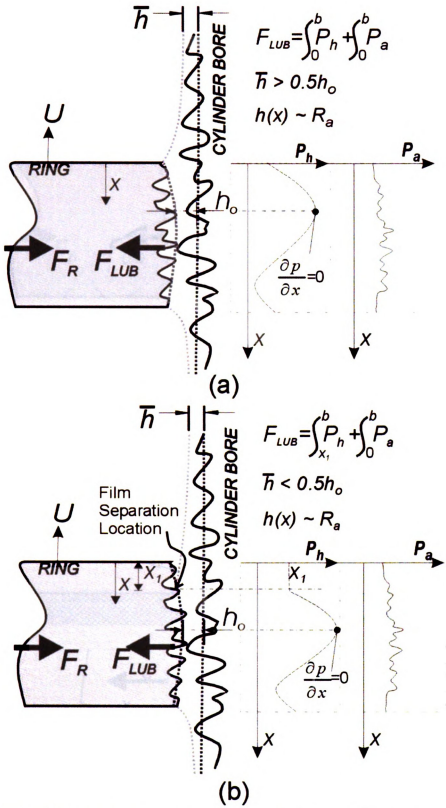

FIGURE 9. (a) Fully and (b) partially flooded mixed lubrication

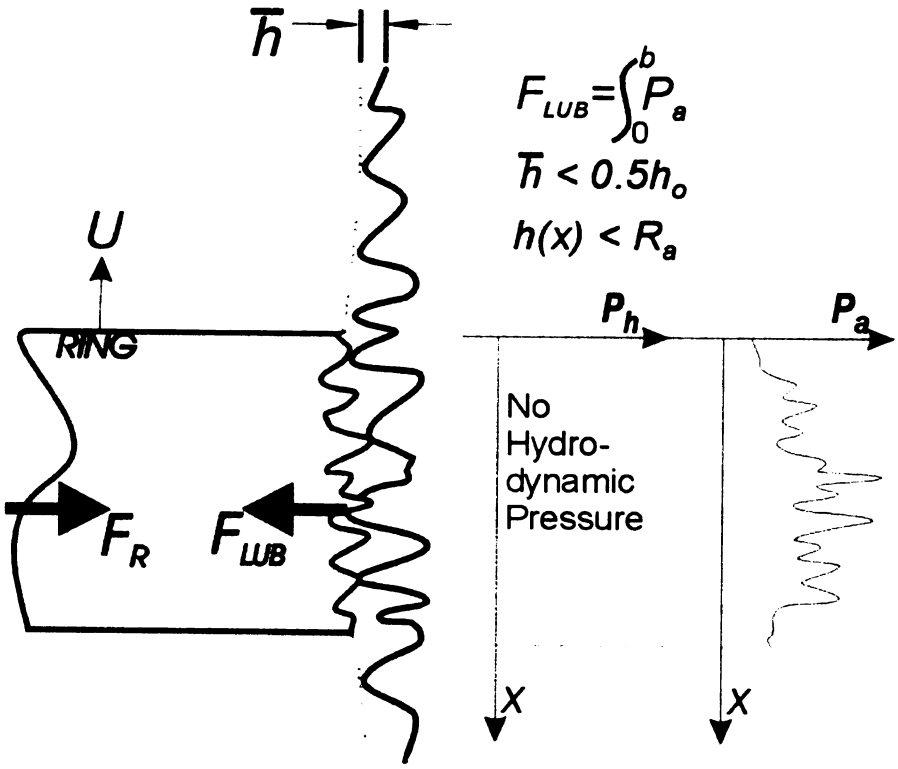

FIGURE 10. Full boundary lubrication

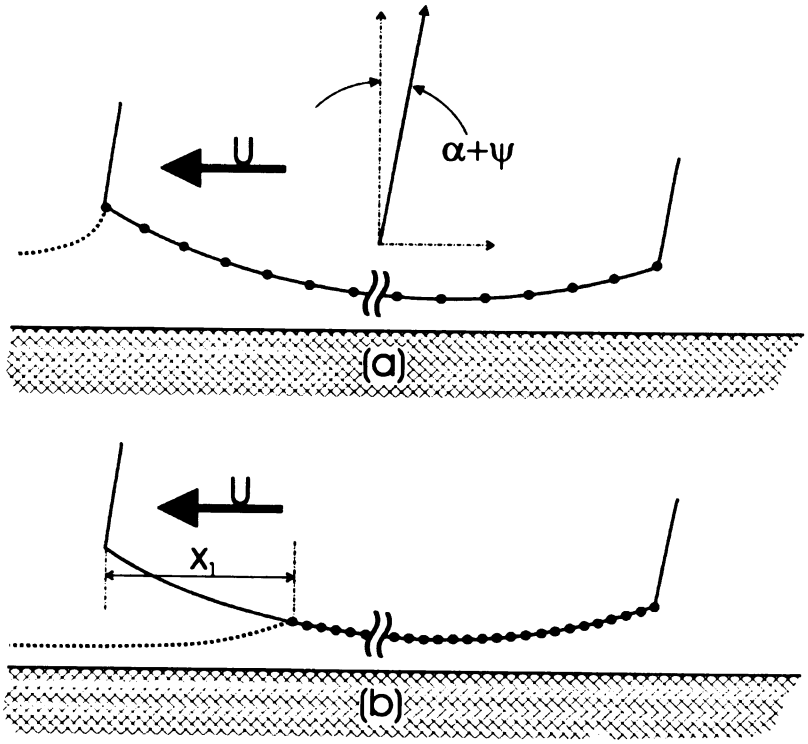

FIGURE 11. Ring face discretization at (a) fully flooded and (b) partially flooded condition

3.5.2 Flow Continuity

To ensure flow continuity, lubricant flow across the top ring/bore front interface is treated as the combination of Couette and Pouiseille flows. Consider Figure 8 that shows a schematic drawing of hydrodynamic lubrication, and a common Reynolds hydrodynamic pressure distribution along the ring face that can be obtained through the numerical solving of Eq. (5). If the piston ring and the bore are treated as two bodies sliding at a relative velocity of U, at the point where $\partial p/\partial x = 0$, only Couette flow exists, and the film thickness is designated as h_o at the location. A general Couette flow equation as shown in [77] is

$$u = U\frac{y}{h(x)} + \frac{1}{2\mu}\left(\frac{\partial p}{\partial x}\right)(y^2 - h(x)y) \tag{18}$$

In the case of $\partial p/\partial x = 0$ at h_o, the equation above simply reduces to

$$u = U\frac{y}{h_o} \tag{19}$$

The average flow past h_o can be represented by

$$q = \frac{U}{2}h_o \tag{20}$$

Assuming steady oil film that enters the ring/bore front edge, designated as $\bar{h}$, the average flow is given as

$$\bar{q} = U\bar{h} \tag{21}$$

Since $\bar{q} = q$ for continuous flow, it results in

$$\bar{h} = \frac{1}{2} h_o \tag{22}$$

Without considering the details of how the oil transport evolves across the ring/bore interface, the flow continuity in this numerical scheme is ensured through the satisfaction of the condition in Eq. (22). The condition in this equation is also used to check for oil sufficiency for the development of hydrodynamic pressure across the entire face of the piston ring. If the lubricant film on the cylinder bore $\bar{h}$ is greater than or equal to $0.5h_o$, a fully flooded condition will exist. Otherwise, sufficient lubricant will not be available to the ring to develop fully the Reynolds hydrodynamic pressure across its face. This is referred to as lubricant starvation or partially flooded condition. An assumption used in the model for the simplification of computation is that the second land between the top and the second rings is always in flooded condition. The mass conservation scheme at the trailing edge can be included in the later improvement of this model.

3.5.3 Load Equilibrium

The insufficiency of the supplied oil to the ring/bore interface will result in the reduction of oil film thickness in the partially flooded condition. In order to ensure load equilibrium in a starved condition, the following procedure is employed:

1. Consider that when lubricant starvation occurs, h_o should be set twice the $\bar{h}$ value according to Eq. (22) in order to ensure oil flow continuity.

2. In the numerical solution of Equations (5) and (11), lower minimum oil film thickness will result in the increase of the lubrication force (F_L), which is greater than the applied force (F_R). In order to reduce the lubrication force, one way is through the correction of the hydrodynamic component by adjusting the location at which the hydrodynamic pressure begins (film separation point at ring face). The location is moved from the leading edge of the ring to a location some distance from the leading edge (x=x_1) and the value of x_1 is determined by adjusting it until Eq. (15) is satisfied. This adjustment will not affect the asperity component because the asperity contact equation is indeed only a function of the ring/bore clearance regardless of whether it is fully flooded or partially flooded.

3. The new film profile $h(x)$* will be rescaled beginning with x_1, and the location of the maximum pressure where $\partial p/\partial x = 0$ is again determined. This location will be different from where it was originally calculated as illustrated in Figures 8 and 9.

4. The new minimum oil film thickness is adjusted by δh within bounded criteria of pure hydrodynamic and pure boundary lubrication, and once again, h_o is set twice the $\bar{h}$ value according to Eq. (22). The process in steps 2 and 3 is repeated until Equations (15) and (22) are satisfied simultaneously.

3.6 Model Application

In order to demonstrate the potential of this present model in simulating various lubrication conditions, it is applied to a hypothetical engine operating condition. A single-ring piston assembly system utilizing the measured cylinder pressure trace of an engine, which operates at 2900RPM rated running condition, is selected for this analysis because it provides unique boundary conditions at a particular time interval for the instantaneous emergence of various lubrication conditions across the ring circumference. The impact from piston secondary motion (tilting) is also included to create an asymmetrical ring/bore interaction across ring circumference. The selected top compression ring has a barrel face profile, and the cylinder bore oil film thickness exposed to the combustion chamber is maintained at 2.5 micron. This bore oil film thickness value will serve as the supplied oil to the front edge of ring/bore interface during piston upward strokes. The ring surface coordinate system shown in Figure 12 is employed in the plotting of the results. The ring circumferential direction begins from the thrust side, and the normalized axial direction begins from ring edge that faces the combustion chamber.

The results shown in Figures 13 to 18 are captured at crank angle of 348 degree when the ring is approaching TDC during the compression stroke. Figure 13 illustrates the film attached/detached characteristics at the ring surface. The partially flooded condition is observed across the ring front edge. At about 78, 136, 220 and 284 degrees across ring circumference, the partially flooded condition extends across the entire ring width. Observation from the oil film thickness result in Figure 14 shows that these areas are where the oil film detaches from the ring face, and minimum lubrication is maintained merely by the surface roughness, which define the full boundary condition. On top of that, there are four regions fully filled with lubricant at about the circumferential degrees of 60, 120, 240 and 300. The circumferential variation of the lubrication condition is due to the piston tilting effect as well as the conformed ring tension pressure pattern. It is also noted that the variation of the film attached/detached profile follows a rather symmetrical pattern across ring circumference, which illustrates the symmetrical effect from the piston tilting motion about the piston pin axis.

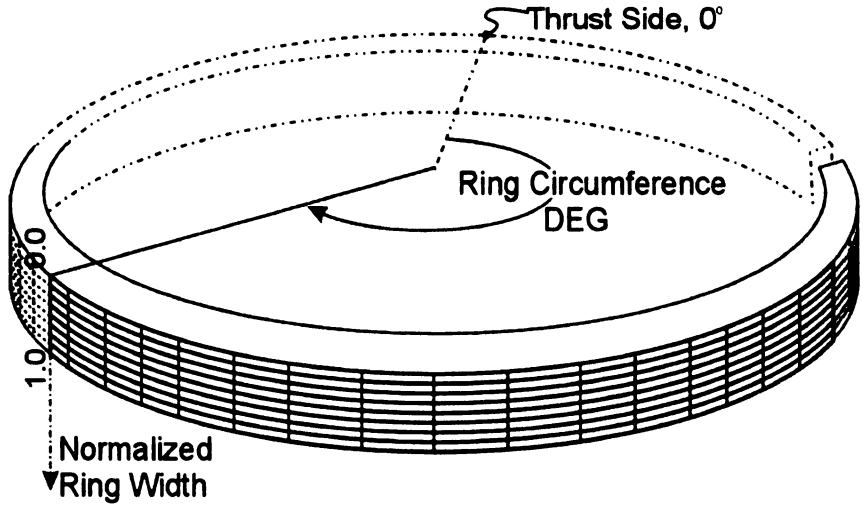

FIGURE 12. Ring surface coordinate system

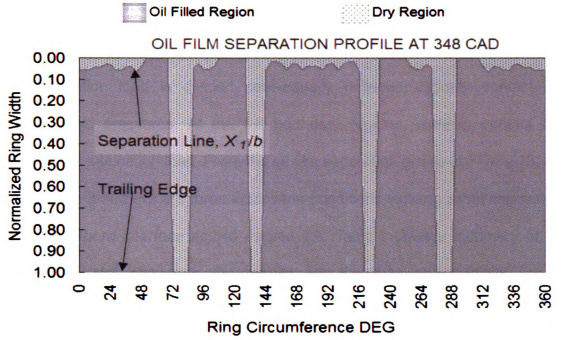

FIGURE 13. Oil film distribution across top ring surface near TDC

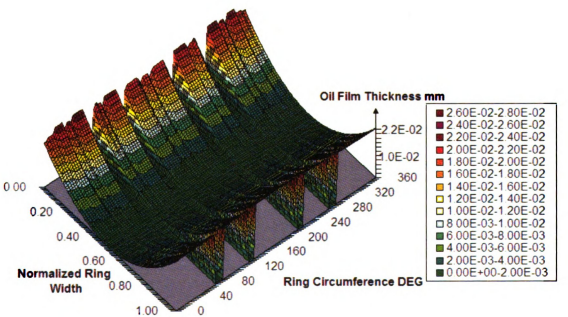

FIGURE 14. Oil film thickness magnitude across top ring surface near TDC

Figure 15 shows how the hydrodynamic and asperity contact pressures share the role in supporting the lubrication load at 348 degree CA. Except at the full boundary regions, (about circumferential degree of 78, 136, 220 and 284), the total lubrication load is divided near-equally between asperity contact and hydrodynamic pressures. At the full boundary regions, asperity contact fully supports the lubrication load. From the oil film separation profile in Figure 13, one can observe that there are three lubrication conditions existing simultaneously at the top ring/bore interface at 348 degree CA. Table 1 gives a summary of this observation. Not shown in the results are the fully and partially flooded hydrodynamic conditions, which are similar to mixed condition except without the contribution of asperity contact to the lubrication load when the oil film thickness is an order higher than the asperity height. The present analysis can be easily altered by using a higher value of the bore oil film thickness as an input in order to simulate pure hydrodynamic conditions.

TABLE 1. Ring/bore lubrication types at 348 degree CA

Condition	Region across Circumference (DEG)
Fully Flooded Mixed	52-68, 108-128, 232-252, 292-308
Partially Flooded Mixed	0-48, 88-104, 144-216, 256-272, 312-360
Full Boundary	72-84, 132-140, 220-228, 276-288

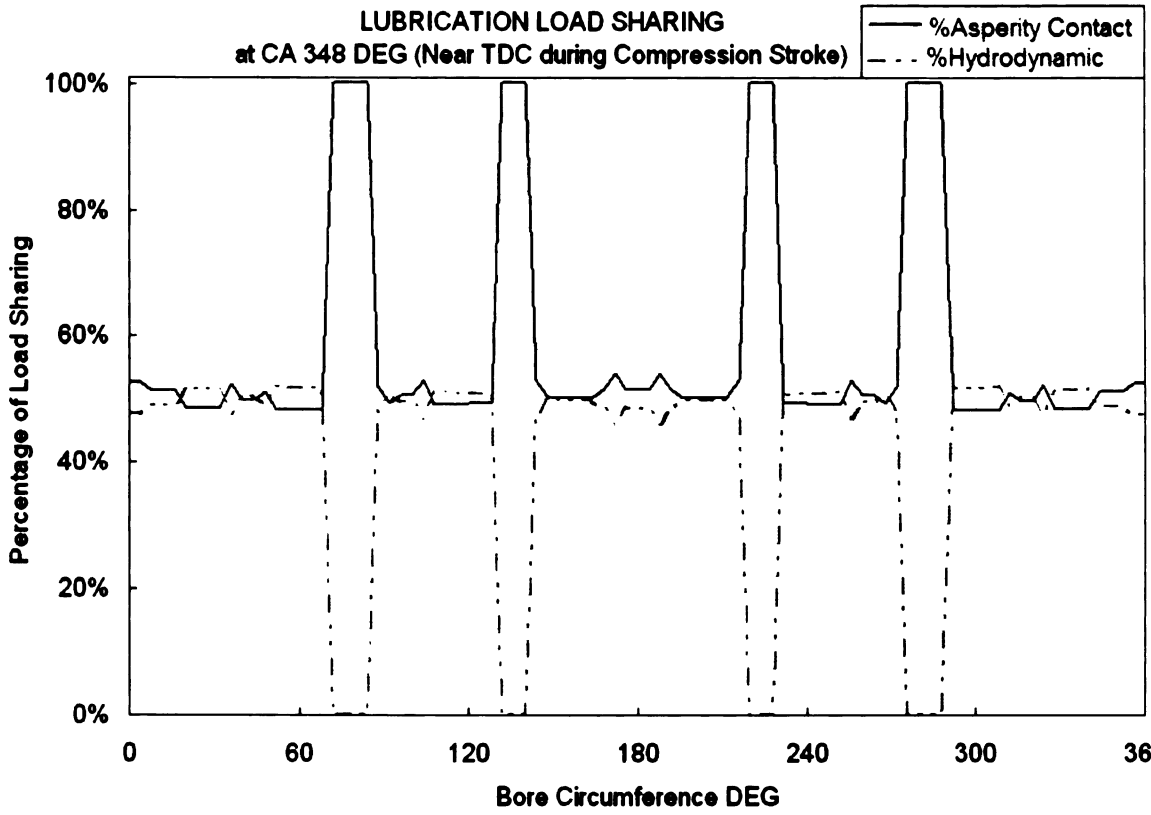

FIGURE 15. Asperity contact and hydrodynamic sharing lubrication load

Figures 16 and 17 show the hydrodynamic pressure distribution on the ring surface at 348 degree CA. At this crank angle, the hydrodynamic pressure gradient across the ring width is large due to high compression pressure in the combustion chamber. Breakdown of the hydrodynamic pressure is found at the full boundary lubrication region as mentioned in the previous section. Three hydrodynamic pressure profiles are selected from Fig. 16 and plotted in Fig. 17. They are typical Reynolds hydrodynamic pressure profiles. It is noted here that a half-Sommerfeld boundary condition is adopted, in which the front edge pressure is specified with the cylinder pressure and the trailing edge is with the sump pressure. Figure 17 illustrates more clearly the film separation effect on the development of hydrodynamic pressure. At the circumferential location of 0 and

24 degrees, the normalized film separation points (x_1/b) at the ring front edge are 0.05889 and 0.03043 (partially flooded). The separation point reaches the ring front edge at 52 degree (fully flooded). In numerical computation, the separation points mark the first integration point for the calculation of the lubrication load due to hydrodynamic pressure. Thus, only the ring/bore region that is fully filled with oil film (not film separation) will be accounted for in sharing the lubrication load. However, the film separation condition will not affect the asperity contact load calculation because asperity contact pressure is a function of the effective ring/ bore clearance instead of the hydrodynamic oil film, according to Eq. (11). Figure 18 shows the asperity contact pressure distribution across the ring surface. The asperity contact pressure peaks at the full boundary lubrication region and concentrates around the axially central area across the ring face. This is because the barrel profile of the ring face provides gradually increased clearance away from the middle of the ring surface in the axial direction. In spite of a tiny change of the ring face profile across ring width, (on the order of 0.05 micron per nodal point; see Fig. 11), the change of the clearance-induced asperity contact pressure is quite large near the central area across the ring width. This large change is caused by the non-linear characteristic of the function used in the calculation of the asperity contact pressure as given by Eq. (11).

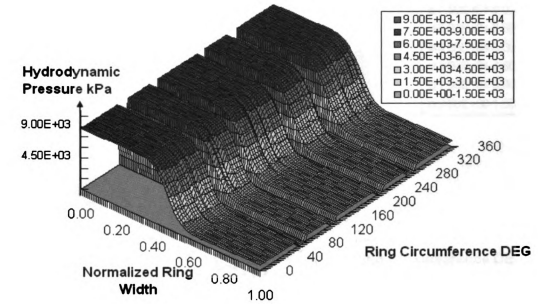

FIGURE 16. Hydrodynamic pressure distribution across top ring surface near TDC

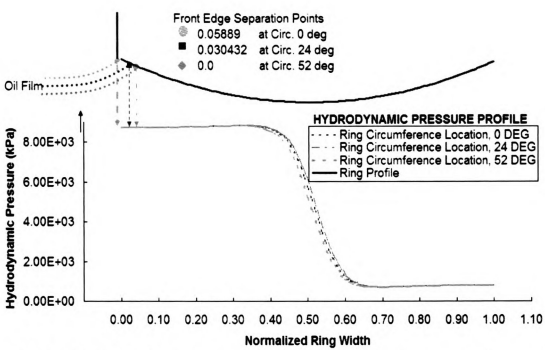

FIGURE 17. Hydrodynamic pressure and front edge film separation point at three distinct bore locations

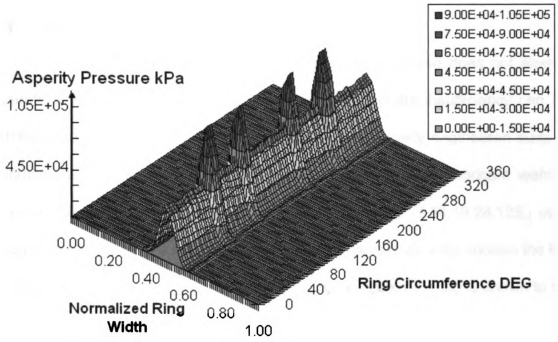

FIGURE 18. Asperity contact pressure distribution across top ring surface near TDC

CHAPTER 4 OIL EVAPORATION AND STARVED LUBRICATION

4.1 Introduction

The piston ring pack in an internal combustion engine does not always operate with sufficient lubrication. The causes of lubricant insufficiency can be attributed to the hostile combustion environment, improperly engineered surface microstructure, poorly designed ring face profile, insufficient lubricant wetting system, excessive temperature-induced oil consumption [3,18,19,28,125,] etc.; and the consequences such as wear and scuffing can significantly shorten the life of engines. For a multi-ring pack system, the top compression ring is known to be the most impacted ring due to its excessive thermal and mechanical stress and poorly lubricated state [113,114].

Many efforts that include partially flooded analysis to account for better physical representation of the piston ring/bore lubrication have approached it from the aspects of fluid mechanics [13,43,102,113]. A common approach in modeling the partially flooded lubrication is through imposing the inlet oil film thickness as the boundary condition at the ring/bore conjunction, and finding the location of the oil film attached/detached edge in order to satisfy both flow continuity and force equilibrium. In many studies, the inlet oil film thickness for the top compression ring during its upward stroke is either an input from measured data, or from the oil film layer left on the cylinder bore from its previous downward stroke, or from a constant value slightly higher than the surface roughness. These studies seldom accounted for the thermal effect from the temperature of the cylinder gas and bore wall on the oil film layer, which is exposed to the environment in the combustion

chamber. Bore temperature is accounted for mostly in the oil viscosity calculation while the cylinder gas temperature is not taken into account in the piston ring/bore lubrication. However, it is believed that the combustion gas and bore temperature do play greater roles in influencing the piston ring/bore lubrication through the evaporative effect on the piston ring pack oil transport system [4]. This model attempts to simulate a more realistic condition faced by the top compression ring by incorporating heat and mass transfer process in the computational analysis of partially flooded piston ring/bore lubrication.

4.2 Engine Oil Evaporation

In most applications, oil consumption due to lubricant evaporative process is inevitable due to high pressure and temperature gradient conditions in the combustion chamber [3,18,28,125]. Even though the top compression ring usually has very high sealing pressure that controls the combustion gas from escaping into the engine crank case, and helps in keeping the oil film thickness at a minimal level to minimize oil loss, the lubricant can still find paths into the combustion chamber. As a surface is never smooth, the peak-and-valley profile of a lubricated surface provides potential venue for the lubricating oil to retain. In the cylinder-kit assembly, a thin layer of oil is retained on the cylinder bore surface during the downward stroke of the top ring. This oil layer can become an important lubrication supply for the top compression ring during its return trip. However, this oil layer is also subjected to the hostile environment that encourages rapid heat and mass transfer. If the oil evaporative rate is high, the time interval between two successive strokes then provides significant exposure time for the oil layer to

evaporate, and results in a severe oil starvation condition for the top compression ring.

The oil evaporation model included in this present work is an extended effort from the authors' previous work [18,19], but with modification to incorporate a three-dimensional bore temperature distribution; thus accounting for local variation of the heat transfer process across the bore circumferential and axial directions. Single-specie oil is assumed in the model due to limitations of oil chemical properties data available (11-Methylnonacosane -C30H62 is used in the calculation of the oil vaporized pressure). The oil evaporation process is a function of mass flux, engine oil density, and the area of cylinder bore being exposed to the combustion chamber. The instantaneous evaporation rate at a local cylinder bore area can be calculated using the equation:

$$\Delta Q_{evap} = \frac{\dot{m}''_{evap} \Delta t \Delta A}{\rho_{oil}} \tag{23}$$

The cylinder bore temperature is a key determining factor in the process of oil evaporation [3,18,125]. Consider the thin oil film thickness left on the cylinder bore, which is on the order of microns; the film surface temperature is very close to the cylinder bore temperature. The film surface temperature is a key factor in the formation of oil vapor for the evaporation process to occur [126]. Hence, increasing bore temperature will speed up the evaporation process.

Not only does the oil evaporation process affect engine emissions, it also influences the lubrication of the piston ring pack, specifically of the top

compression ring. As illustrated in Figure 19, the oil layer at the front of the top ring during its upward movement serves as an oil supplier for its lubrication. This oil layer plays a role in assisting with the building up of hydrodynamic pressure that prevents metallic contact and scuffing. When being exposed to the environment of the combustion chamber, the oil film thickness begins to deplete, causing the top compression ring to be more susceptible to encounter mixed lubrication or even dry lubrication during its upward movement.

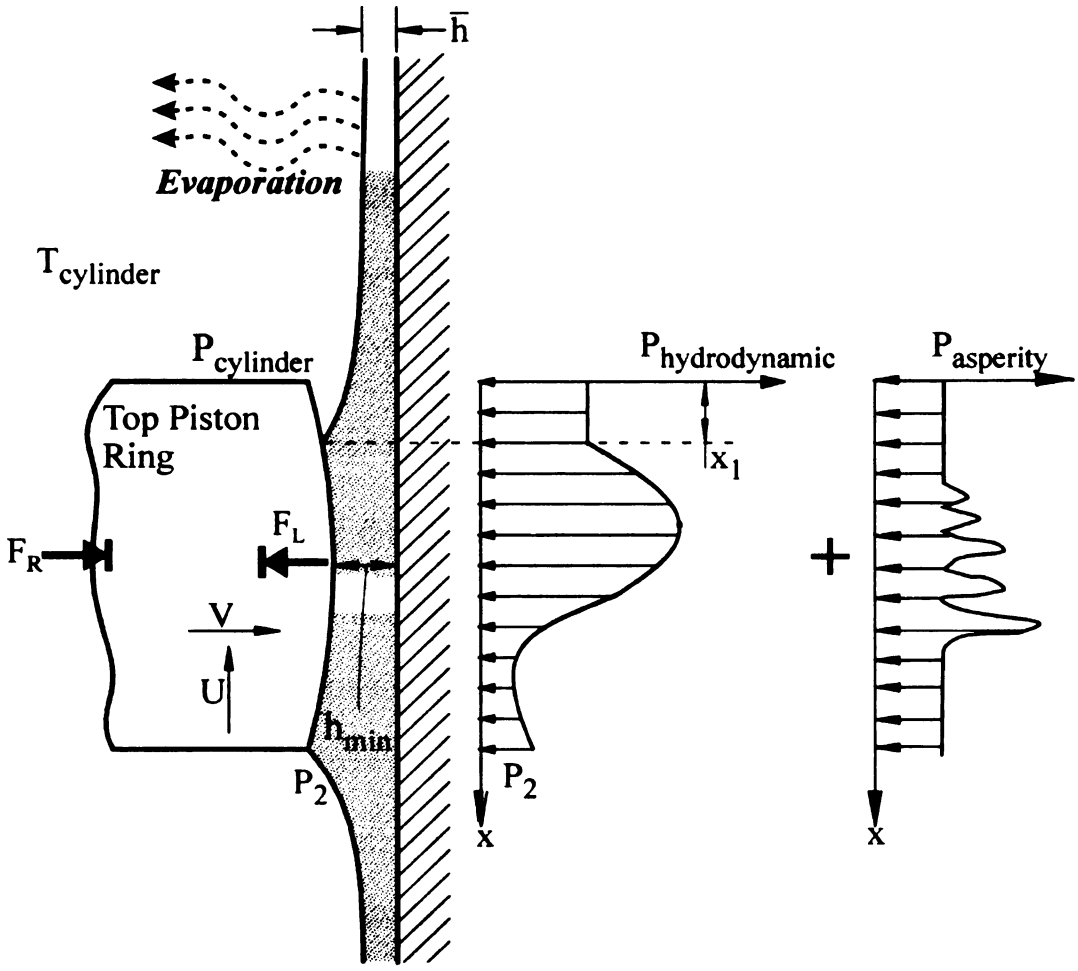

FIGURE 19. Top piston ring in upward stroke

The oil film thickness encountered by the top compression ring during its upward movement determines the boundary condition for the lubrication regime

the contact interaction will experience. The well recognized Stribeck Curve in Figure 20 illustrates this point. At sufficient oil supply, the oil film thickness h is an order of magnitude higher than the surface roughness R_a resulting in the surface interaction at hydrodynamic regime. When the amount of lubricant supplied to the contact decreases, h will decrease to an order of magnitude comparable with R_a, and as a consequence, interactions between the asperities of the surfaces occur, resulting in mixed or boundary lubrications. As a result, friction and wear increase.

In fact, the piston ring/bore contact always operates in mixed lubrication condition due to the fact that the oil film thickness between piston ring and bore is on the same order of magnitude as the surface roughness in most engine operating conditions, particularly near TDC and BDC. At the piston ring/bore interface, as shown in Figure 19, both the hydrodynamic pressure, P_h, and asperity contact pressure, P_a are sharing the lubricating reaction load in balancing the applied load due to the gas pressure behind ring groove, the ring tension and the ring stiffness due to ring/bore conformability. The integration of the hydrodynamic and asperity contact pressures over the ring face results in the lubrication reacting load. However, in the partially lubricated condition, there exists film separation near the front edge of the ring face, and this results in a smaller surface area available for the development of hydrodynamic pressure. This also implies that the asperity contact interaction may play a greater part in the lubricating load if the minimum oil film thickness is comparable with the surface roughness. The distance from the front edge of the ring to the separation point is

denoted as x_1, and it is dependent on the amount of lubricant supplied to the contact, $\bar{h}$. In the computational approach, x_1 can be determined numerically while solving for hydrodynamic and asperity contact pressures using the Reynolds and asperity contact equations. Convergence is achieved when, both locally and globally, F_L is equal to F_R and the flow continuity is also satisfied. The solution, which consists of hydrodynamic and boundary components, can serve as input for further calculation of friction and wear at the piston ring/bore interface. The piston ring/bore wear model is integrated in the lubrication model, and it is a direct application of Archard's equation [2] for mechanical adhesive wear between two surfaces.

4.3 Computational Methodology

The cylinder-kit analysis of an engine system consists of two basic components: cylinder gas dynamics and tribology. In the application of this model, CASE is used to provide essential data for the calculation of this model. Referring to the flow chart in Fig. 21, the input specifications are the geometrical dimensions and the operating conditions of an engine. Within CASE, the structure of its lubrication system is rearranged to accommodate the oil evaporation model. The lubrication computation is divided into two time domains, downward stroke and upward stroke. The oil evaporation model is employed as a function to compute oil supply for the piston ring/bore interface under the effect of oil evaporation during upward stroke. Using the gas dynamic model of CASE, the boundary and initial conditions such as the piston ring pack pressure, piston and piston ring

motion are calculated and adopted as the input for the computation of this modified lubrication system. The computational cycle of a four-stroke engine system begins with the intake stroke (0 - 180 degree crank angle (CA)) and ends with the exhaust stroke (540 - 720 degree CA).

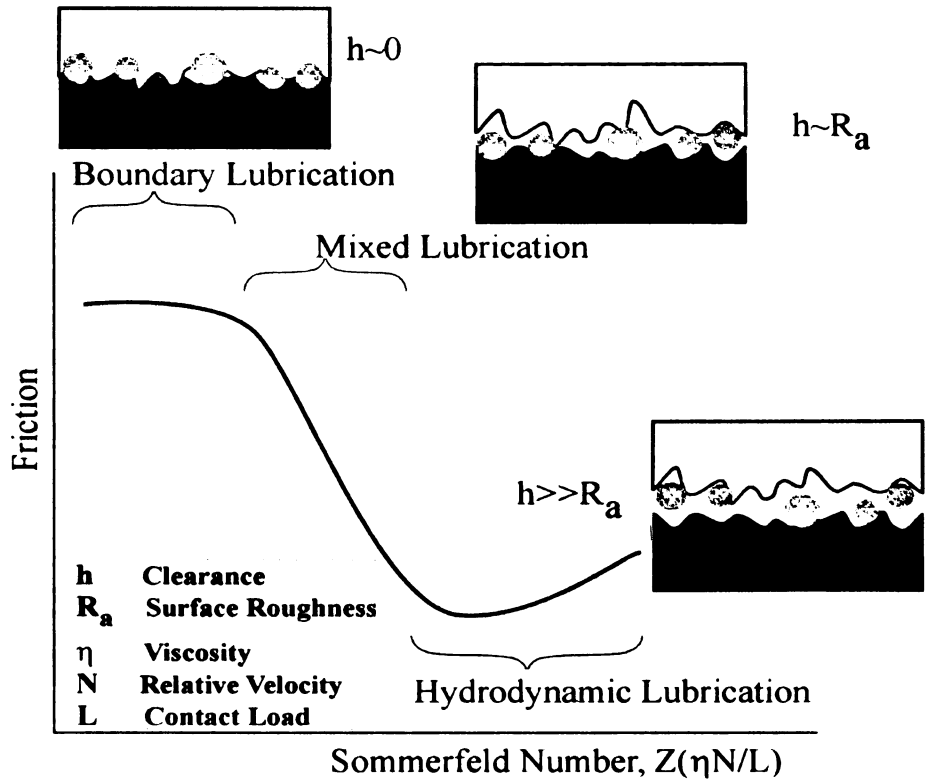

FIGURE 20. Stribeck curve

4.3.1 Downward Stroke

During the downward stroke (intake and power strokes), the piston ring pack is assumed to operate under the fully flooded condition. At each time interval, the minimum oil film thickness along the circumference of the top compression ring is recorded into the cylinder bore spatial domain, and treated as a layer of oil film retained on the bore wall. The spatial domain of the cylinder bore

is represented by a system of nodes, where each node contains lubrication information such as surface roughness, bore distortion and temperature, retained oil film thickness, heat transfer coefficients, etc. At successive time intervals after the passing of the top compression ring, nodal oil films that are exposed to the combustion chamber will begin their evaporative process. During this phase, the nodal oil film thickness will deplete as a result of oil loss calculated using Eq. (23). The evaporation process continues as long as the node is exposed to the combustion chamber.

4.3.2 Upward Stroke

After the piston reaches bottom dead center (BDC) and returns in upward motion (compression and exhaust strokes), the oil film thickness of the nodes that were exposed to the combustion chamber will become the oil supply to the ring/bore interface. The amount of oil encountered by the interface will be used in the determination of partially flooded mixed lubrication. Those nodes that have entered the piston ring/bore interaction will then be replenished with new oil film thickness data during the coming downward stroke.

Over an entire engine cycle, the spatial domain of the cylinder bore records the cumulative wear data, which is a resultant phenomenon due to partially flooded lubrication under the influence of oil evaporation.

4.4 Model Application

In general engine application, there exists a vital relation between the ring/bore lubrication and oil consumption [53]. This model is applied in a diesel engine

analysis to demonstrate the importance of oil evaporation effect in the analysis of partially flooded lubrication, and to study and understand a phenomenon that could potentially exist in an operating diesel engine. Modern diesel fuel injection systems are able to operate over a very broad range and this allows fuel injection events to be timed throughout the compression/expansion process. It is well demonstrated that there are potential adverse consequences in certain areas of fuel injection operation, some of which can cause increased cylinder bore wear. The phenomenon of "bore wall fuel wetting" is a well-known example. Given concerns around the potential for wear-inducing interactions between the fuel injection plumes and the cylinder bore wall, a particular interaction is being studied and analyzed in this work. The interaction shows what impact an imposed local heating of the bore wall can have on the cylinder bore wear.

The basic engine specifications and operating condition are given in Table 2.

TABLE 2. Engine specifications

Engine Model	**5.9L I6 Diesel Engine**
Bore Diameter	102.2 mm
Engine Operating Condition	2900RPM Rated
Ring Pack	Two Compression Rings and One Oil Control Ring
Surface Roughness: Top Ring Bore Wall	 0.08 micron 0.33 micron

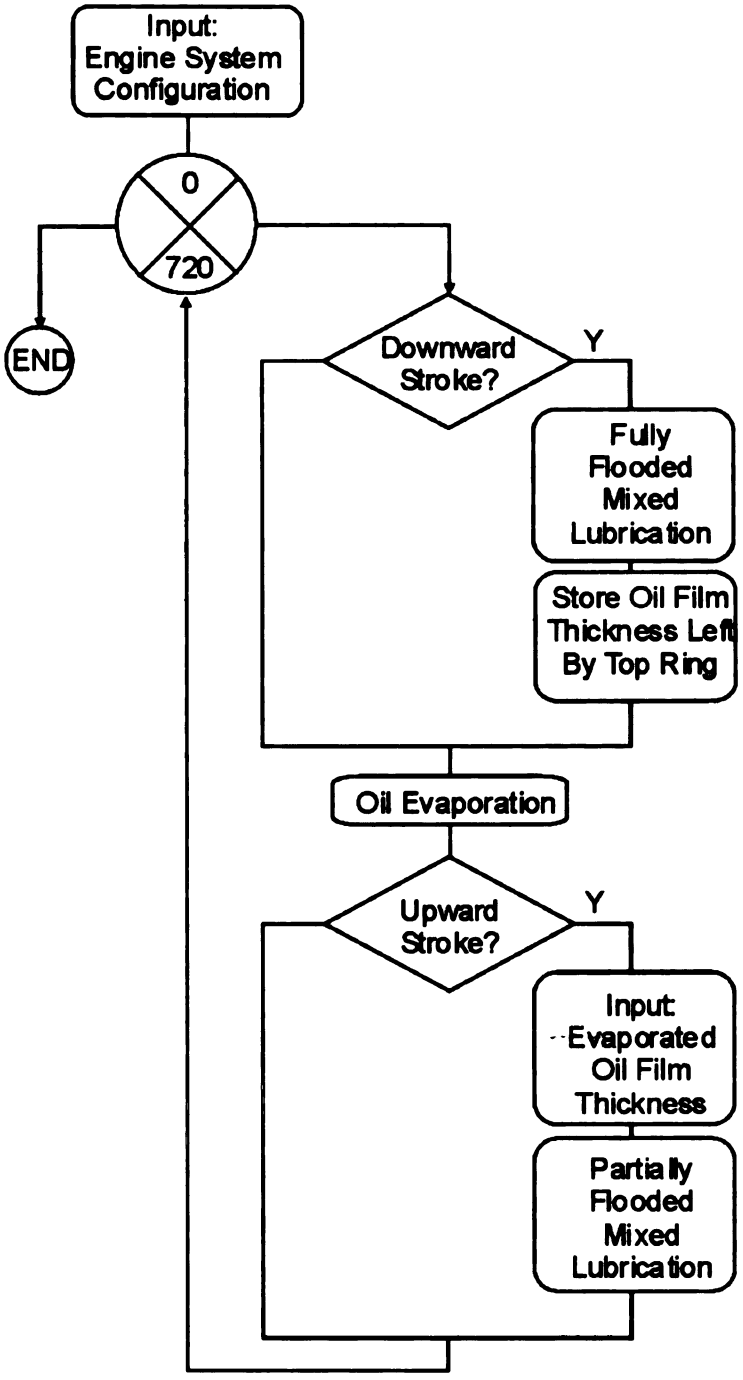

FIGURE 21. Program flow chart

In this application, the cylinder bore temperature is an external input to the model. The original bore temperature is obtained from experimental measurement of a diesel engine operation. Under the assumption that the fuel injection plumes in an operating diesel engine are additional heat sources that contribute to the

increase of local bore wall temperature, the original bore temperature profile is modified through the imposing of higher than surrounding temperature at five distinct locations near TRR on the cylinder bore wall as illustrated in Figure 22. In this example, the peak temperature of the five distinct locations (being referred as hot spots in later discussion) is increased from 180°C to 280°C.

Two discussions of the application will be presented. The first discussion is on the comparison between various lubrication models and how their assumptions affect the bore wear results. The second discussion is on the sensitivity of the bore wear result to the temperature of the hot spots, in which the peak temperature of the five hot spots will be increased by 10°C, 25°C, 30°C, 40°C, 50°C, 60°C, 75°C and 100°C.

4.4.1 Fully Flooded and Various Partially Flooded Lubrication Analyses

Under the same operating conditions and bore temperature, the bore wear results shown in Figures 23-25 and 27 demonstrate that results can vary under different lubrication assumptions. The bore temperature used in simulating these results is the same as the example shown in Figure 22. The hot spot peak temperatures are specified about 100°C higher than their surroundings. The engine thrust side is at 0° on the bore circumference and the hot spots are at 35°, 105°, 180°, 250° and 325° from the thrust side at the same axial location. The axial position of the hot spots is around the top ring reversal (TRR) location, which is about 9.28 mm in actual scale or 7.75 units in the nondimensional scale in Figure 22.

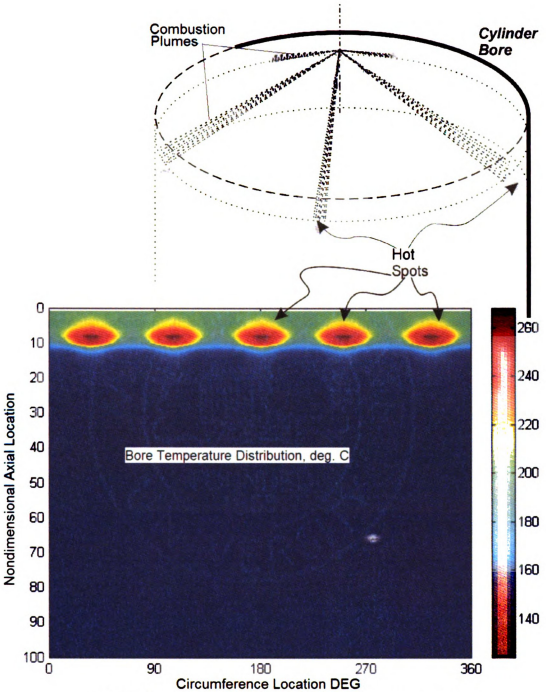

FIGURE 22. Cylinder bore temperature distribution

In all cases, as shown in Figures 23-25, and 27, higher local bore wear is predicted near the top, the second and the oil ring reversal at both TDC and BDC as is agreeable with findings from other works [53,67,119]. Among the results, the fully flooded lubrication analysis predicts the lowest bore wear magnitude near

TRR. The fully flooded analysis assumes that the top compression ring/bore conjunction is operating at fully flooded condition throughout the entire engine cycle.

Figure 24 provides the bore wear result from the partially flooded lubrication analysis without the consideration of oil evaporative effect. In this analysis, the oil film layer, which is left by the top ring during downward movement and exposed to the combustion chamber environment, remains the constant and is used on the successive upward stroke as the input for the partially flooded lubrication calculation at the piston ring/bore interface. It shows only a slight increase of bore wear over the result in Figure 23.

Figure 25 shows the bore wear result from the partially flooded analysis that assumes a constant oil film thickness (2 microns) encountered by the top ring during its upward stroke. The value of 2 microns, which is about 6 times the bore wall surface roughness, is chosen because the top ring/bore interface is operating within the range of about 2 micron of oil film thickness over the entire cycle as shown in Figure 26. This analysis predicts substantially higher bore wear near the TRR along the entire bore circumference.

Without considering the evaporative effect, the results in Figures 23 - 25 fail to capture the greater effect of hot spot temperature on the bore wear. Careful examination of these figures shows that there is a small degree of bore wear increase around the hot spots, which is caused by the oil viscosity reduction in high temperature. According to the common rule of oil viscosity, temperature

increase will result in the decrease of oil viscosity. The direct impact of the decrease of oil viscosity on the lubrication calculation is the decrease of hydrodynamic pressure around the hot spot area. As a result, the oil film around the hot spot area will be reduced when the ring conforms to the cylinder bore, which in turn raises the asperity contact pressure in the lubrication load sharing, resulting in the increase of wear around the hot spot areas. It is also known that lower viscosity will result in less squeezing force from the oil around ring reversal and thus greater asperity contact force is generated to support the applied load on the ring in the radial direction [113].

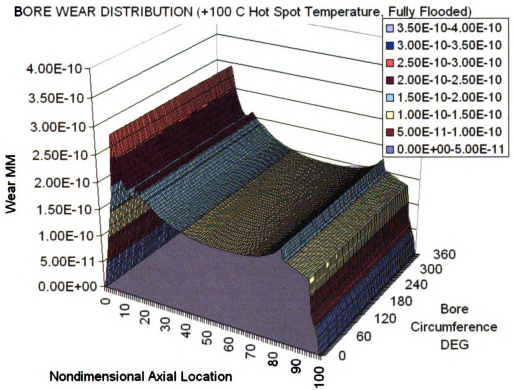

FIGURE 23. Bore wear (fully flooded lubrication)

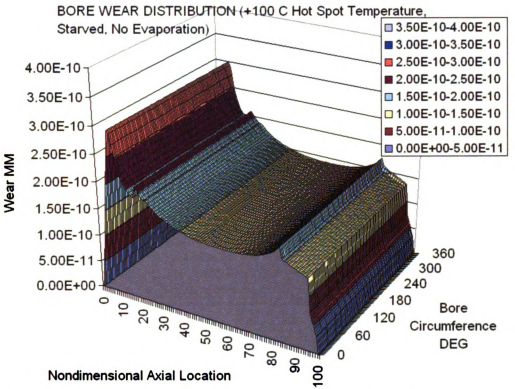

FIGURE 24. Bore wear (partially flooded, no evaporation)

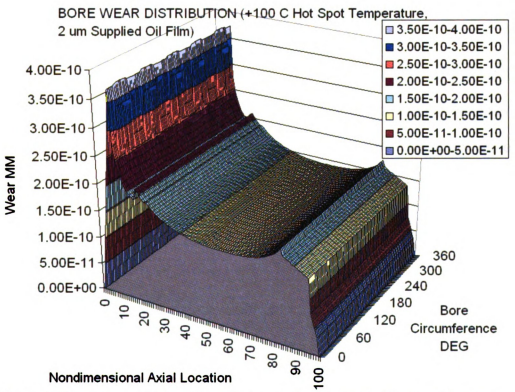

FIGURE 25. Bore wear (partially flooded, 2 microns supplied oil film)

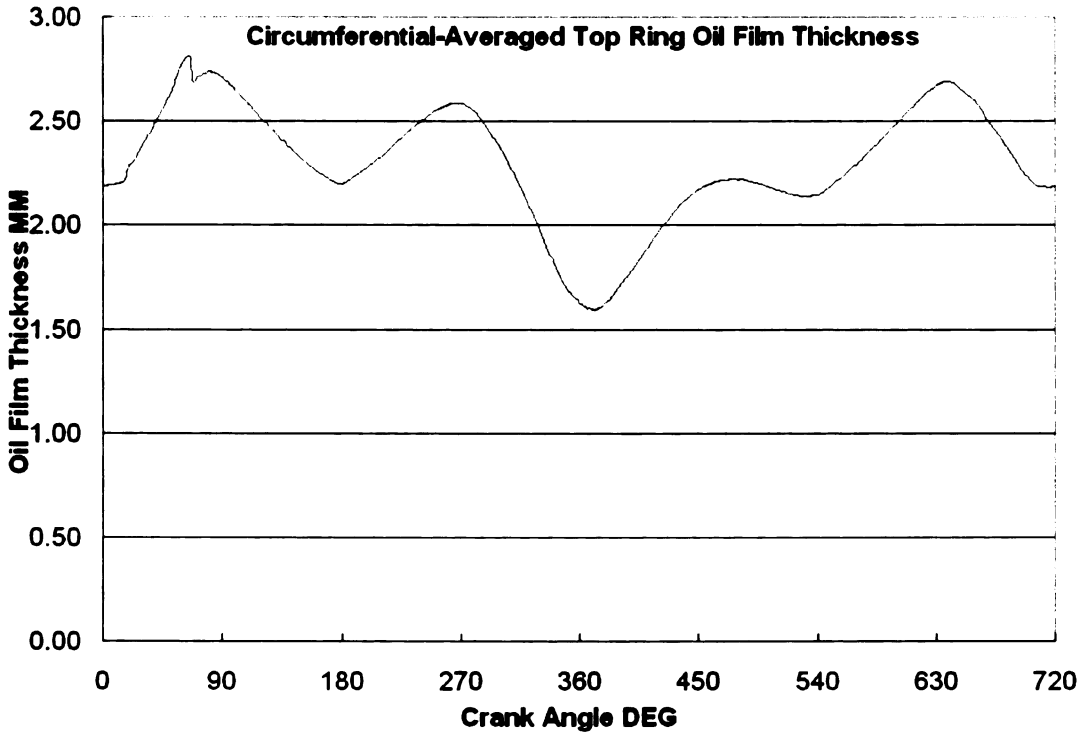

FIGURE 26. Cyclic top ring oil film thickness

By including the evaporative effect in the partially flooded lubrication calculation, the result in Figure 27 shows a significant difference from previous results. Distinctive pockets of high wear are observed at the hot spots while the surrounding areas along bore circumference at TRR have about 25% less wear. This implies that the local effect of bore temperature variation on the bore wear is captured in this analysis.

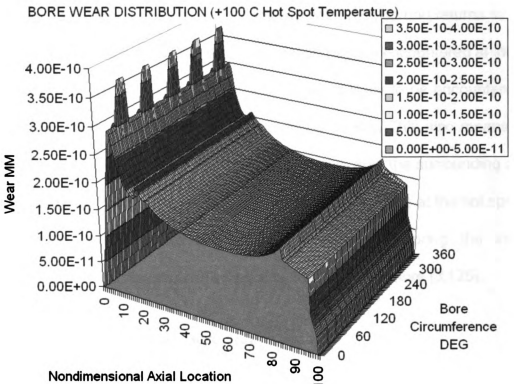

FIGURE 27. Bore wear (partially flooded, with evaporation)

The importance of including the evaporation analysis can be explained by studying the evaporation rate of oil film in the bore spatial domain. Figure 28 shows the change of oil film thickness along the bore circumference at TRR over an entire engine cycle. At 0 and 360 degree CA, the nodal oil film thicknesses at TRR are replenished with oil left from the top ring during its downward movement. As time advances, the nodal oil film thicknesses across bore circumference experience depletion in magnitude as a result of evaporation. The depletion rate is particularly notable at the hot spots. With the temperature 100^{o}C higher than their surroundings, hot spots cause rapid evaporation of oil film. During the intake/ compression process, there is no oil film left at hot spots after a few degrees of

crank angle while the non-hot spot locations experience a relatively slow evaporation rate. This implies that when the top compression ring returns to TRR at the end of the compression stroke, dry lubrication will be encountered at the hot spots while hydrodynamic or mixed lubrication is still likely to be encountered at the surrounding areas, which still have remaining oil film. This also means that bore wear is going to be much higher at the hot spots than the surrounding area. Another observation from Figure 28 is that the evaporation rate at the hot spots is slower during the power/exhaust stroke process than during the intake/ compression stroke. This observation agrees with other literature [3,125].

4.4.2 Temperature Effect on Bore Wear

In order to investigate the sensitivity of bore wear to the magnitude of the hot spot temperature, simulations have been conducted using eight sets of bore temperature distribution, in which each has different peak temperature at the hot spots. The peak temperatures of the hot spots are set 10°C, 25°C, 30°C, 40°C, 50°C, 60°C, 75°C and 100°C higher than their surroundings. The original temperature at the hot spots is about 180°C. The location of the hot spots is similar to those of Figure 22. The bore wear results under these conditions are shown in Figures 29 - 36 respectively.

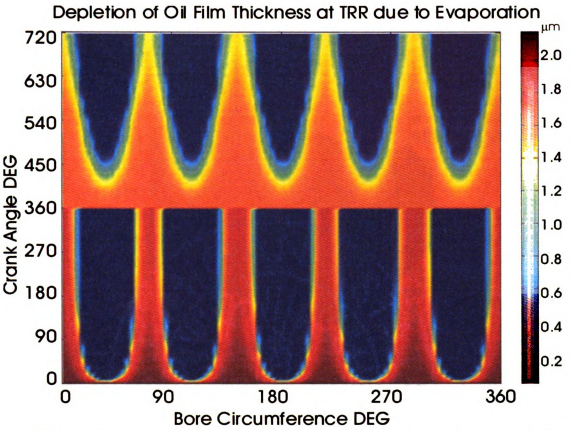

FIGURE 28. Depletion of oil film thickness at TRR under the evaporative effect

From the comparison of these results, one can observe that the increase of the hot spot temperature by 10°C does not produce any wear pockets (Figure 29). But the wear pockets at hot spots begin to emerge when the hot spot temperature is raised by 25°C (see Figure 30). From 25°C to 40°C increment (Figures 31 - 32), the wear increase at the hot spots remains relatively small (about 3% of total wear at TRR), but the area of wear pockets does increase.

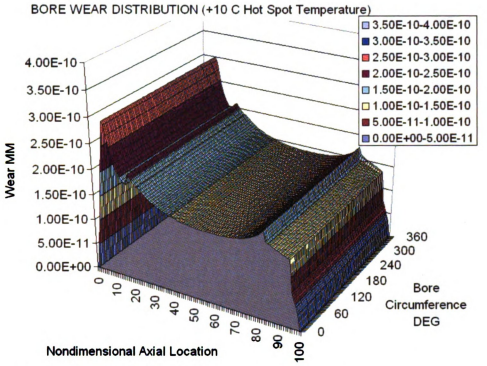

FIGURE 29. Cylinder bore wear with +10 degree C hot spot temperature

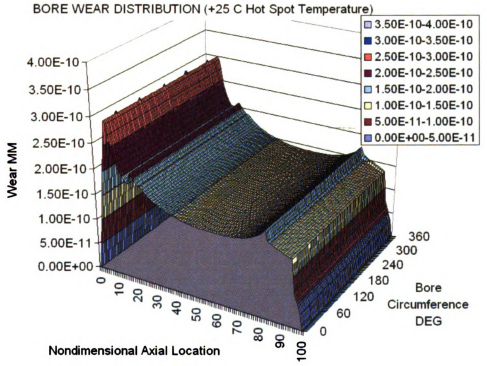

FIGURE 30. Cylinder bore wear with +25 degree C hot spot temperature

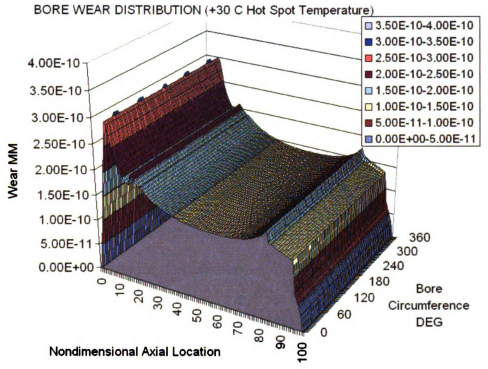

FIGURE 31. Cylinder bore wear with +30 degree C hot spot temperature

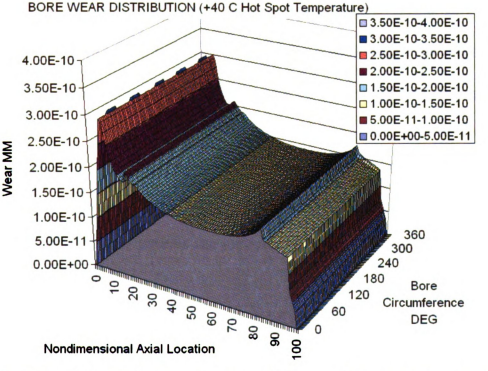

FIGURE 32. Cylinder bore wear with +40 degree C hot spot temperature

As the hot spots' temperature is increased to 230°C (50°C increase), spikes of wear are observed at hot spots (Figure 33). The magnitude of wear pockets jumps up by about 16%. From 50°C, 60°C, 75°C to 100°C increments (Figures 33, 34, 35 and 36), the magnitude of wear pockets increases gradually to about 25%. The increase of the wear pocket area is also more distinct after 50°C hot spot temperature increment. The observation of the change of hot spot wear with respect to temperature increase is summarized in Figure 37 where the non-hot spot wear is included for comparison.

This observation may indicate that there exists a range of temperature at the hot spots at which local bore wear pockets may emerge at a substantial rate. One possible reason may be due to the nonlinear relation between the evaporation rate and the bore temperature (oil vapor pressure is an exponential function of film surface temperature [126]). Hence, the temperature range for substantial increase of the bore wear pocket may fall between the increment of 50°C and 100°C margin. Another possible reason may be due to the exponential relation between film temperature and viscosity. The oil viscosity decreases exponentially as its temperature increases. The nonlinear temperature effect on oil viscosity will result in the reduction of hydrodynamic pressure in a nonlinear pattern, which ultimately causes the increase of asperity contact interaction and wear.

A useful conclusion from this observation is that the hot spot temperature at the cylinder bore wall needs to be controlled so that it does not go 50°C higher than the surrounding area in order to prevent undesirable wear pockets on the cylinder bore. In practice, this analysis may be useful in providing guidelines to the design of a modern diesel engine system that has the potential to encounter this phenomenon.

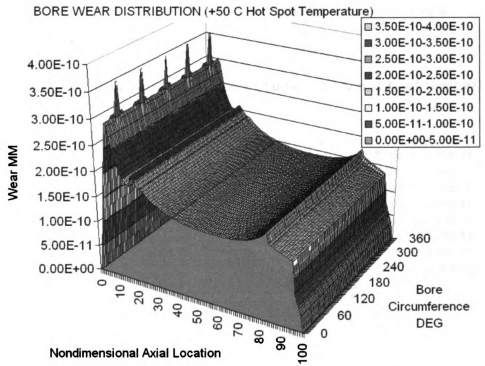

FIGURE 33. Cylinder bore wear with +50 degree C hot spot temperature

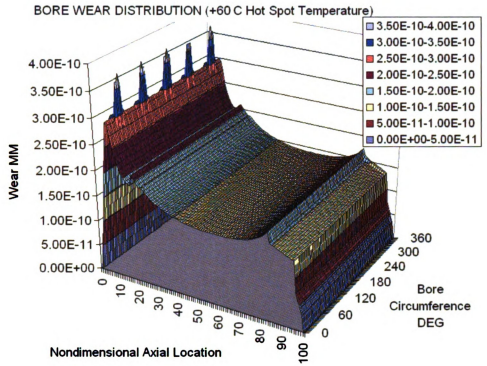

FIGURE 34. Cylinder bore wear with +60 degree C hot spot temperature

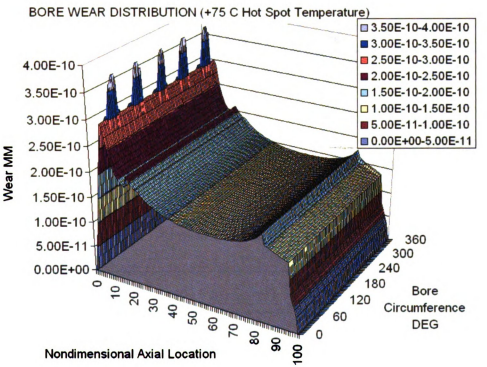

FIGURE 35. Cylinder bore wear with +75 degree C hot spot temperature

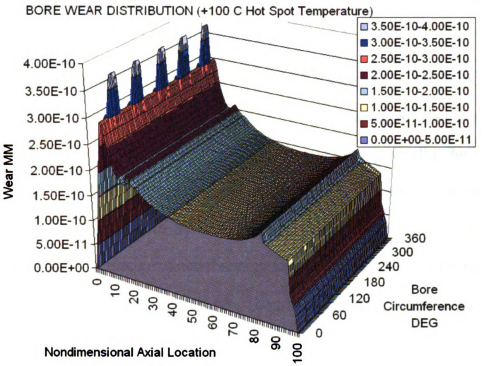

FIGURE 36. Cylinder bore wear with +100 degree C hot spot temperature

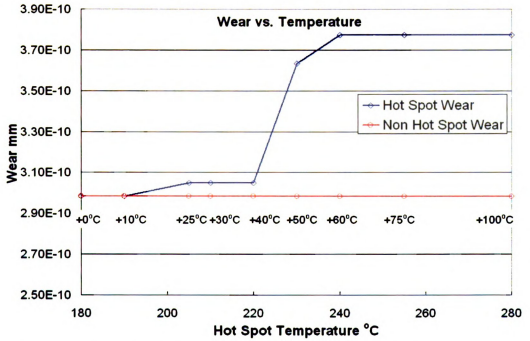

FIGURE 37. Temperature sensitivity of cylinder bore wear

CHAPTER 5 PISTON DYNAMICS AND EHL SOFTWARE

5.1 Introduction

In an internal combustion engine, the piston is the primary component that transfers combustion energy from the fuel to the translating work at the crank shaft that drives the whole engine to perform useful tasks. Hence, the design of a piston is very crucial in determining the efficiency of an engine's performance. Piston quality is often due to its optimal geometrical design, body mass and material selection that ensure minimal energy loss due to inertia, heat transfer and surface interaction with the cylinder bore. The piston also should not compromise its structure strength against fatigue failure. Nevertheless, to derive an optimal set of design parameters is often a very challenging and difficult job because there are many design parameters that affect the piston function. Hence, computational tools become very handy in piston design because of the time and cost effectiveness.

Taking advantage of today's high computer speed, this software, as part of the CASE [13] system, has integrated a piston finite element model into the coupled model of the piston dynamics and tribology so that the same finite nodal information computed from the 3-D FE model is used in the solving of the piston skirt elastohydrodynamics and the piston trajectory. The time-dependent local bore temperature seen by each node during the piston reciprocating motion is used in determining the local viscosity at the piston skirt; hence it accounts for more realistic lubrication calculation that can be influenced by the viscosity variation across the piston skirt surface due to non-uniform bore temperature.

5.2 Simplified Piston Model

Figure 38 shows the solid model of a production piston that contains detailed geometrical information. Constructing this solid model typically requires many hours of skillful computer-aided design (CAD) work. To conduct thermal and static analyses using the model also requires an enormous amount of computational time and effort. Hence, it is not feasible if one is to conduct a typical four-stroke engine cyclic analysis using the model for parametric design study. A simplified piston version (Fig. 39) is used to develop a piston software that can be time-efficient in performing a cyclic piston performance analysis, beginning with the construction of the solid model, the meshing of the model, to the ultimate calculation of the coupled analysis of elastohydrodynamic lubrication and dynamics. A major concern in the model simplification is to decide on the degree of geometrical simplification so that principal structural characteristics of the piston are not lost. On the other hand, the geometrical input for the simplified model should have reasonable flexibility that allows the software to be applied in most production pistons for the piston performance analysis. Hence, in the preliminary effort of this software development, the simplified piston solid model contains the following parameters (refer to Fig 40):

1. Piston diameter
2. Piston height
3. Piston pin axis locations
4. Average boss thickness
5. Average crown thickness

6. Piston skirt inside radius
7. Piston skirt radius center
8. Piston skirt height
9. Piston skirt width
10. Piston skirt tab dimensions

The above parameters can be considered as the principal parameters that define the piston of most internal combustion engines. An important parameter to be included later is the piston pin hole. Currently the piston pin is merged into the average piston pin boss section, and the pin axis locations are designated by four finite element nodes. These four nodes allow inertia loads to be assigned appropriately, and the non-symmetrical effect of piston movement due to the piston pin offset is preserved.

In order to investigate the structural and thermal behavior of the simplified piston model with respect to the actual production piston model, thermal and static analyses are conducted. The results are shown in Figures 41 and 42. It is observed that the magnitude of the calculated piston skirt surface temperatures are comparable between the two models, and the maximum temperature at the top of piston crown differs by about 4%. The calculated piston distortions are also in the same order of magnitude, but the distortion gradient toward the center of skirt surface on the actual model is higher than on the simplified model. This discrepancy is due to the absence in the simplified model of the pin hole and the pin boss, which extend to the bottom of the top piston crown. It is believed that the discrepancy will be reduced significantly once those features are implemented

into the simplified piston. At this preliminary stage, considering that the distortion characteristics on the piston skirt are similar from the qualitative point of view, this simplified piston model will be adopted for the computation of the coupled analysis of piston elastohydrodynamic lubrication and dynamics.

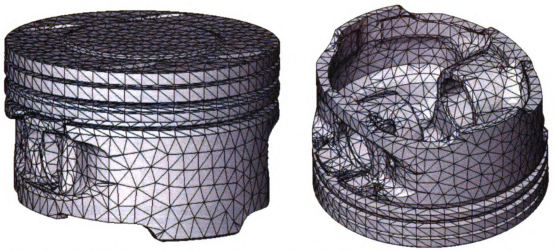

FIGURE 38. Piston solid model constructed with commercial CAD tool

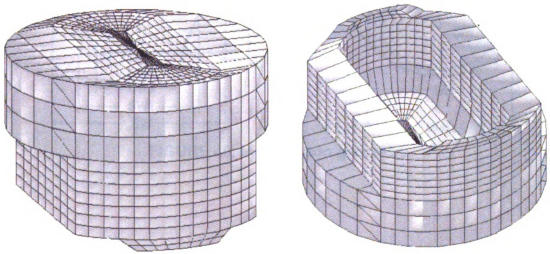

FIGURE 39. Piston solid model constructed with CASE

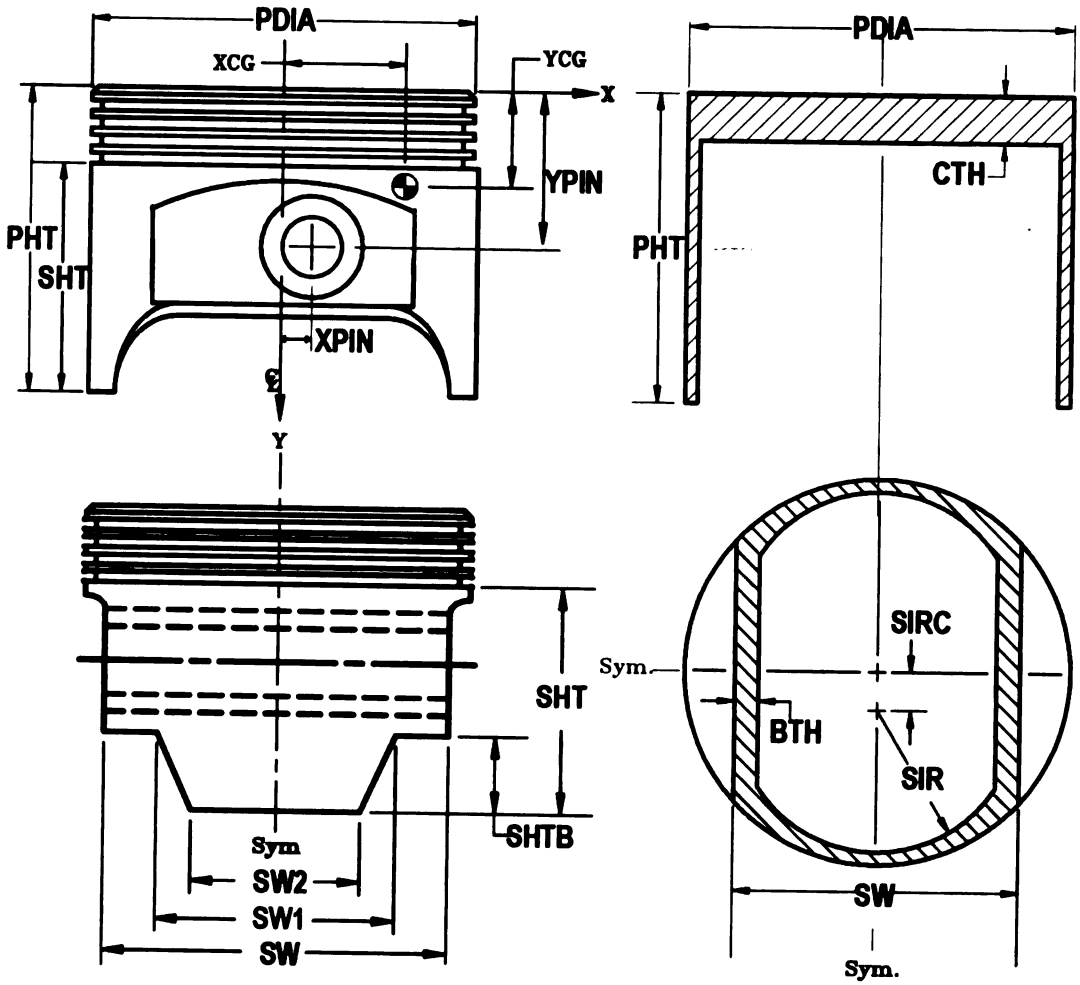

FIGURE 40. Input piston geometry

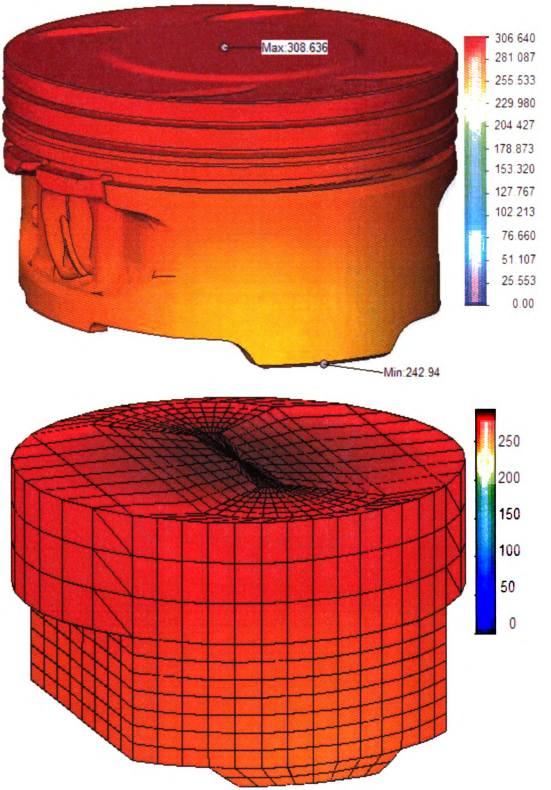

FIGURE 41. Computed temperature distribution between complicated and simplified Piston

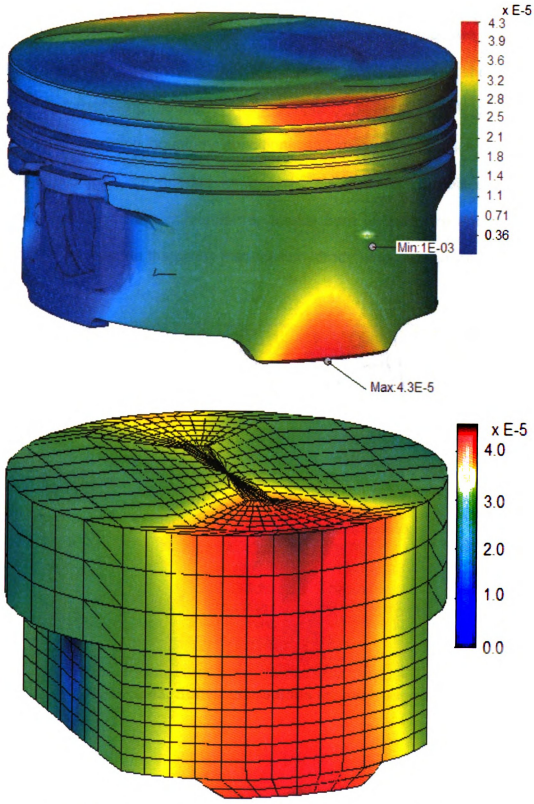

FIGURE 42. Computed distortion between complicated and simplified piston

5.3 Software Modules

This piston modeling software comprises several modules integrated together for a comprehensive simulation of piston performance as shown in Fig. 43. The preprocessing module allows the input of piston assembly geometrical parameters, operating boundary conditions and material properties, and other simulation control data needed for a cyclic piston analysis. This software is capable of taking in the non-uniformly spatial bore temperature and distortion information to compute the piston skirt elastohydrodynamic lubrication.

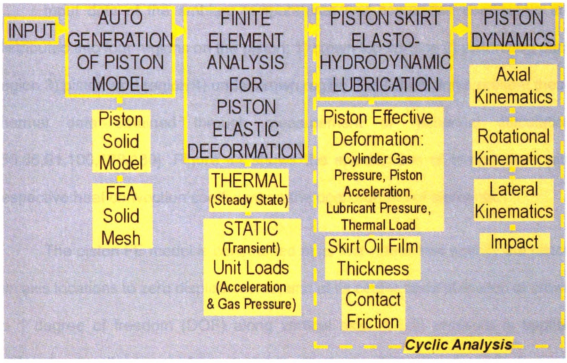

FIGURE 43. Software modules for piston modeling

5.4 Three-Dimensional Finite Element Modeling

5.4.1 Constructing and Meshing a Piston Solid Model

The first computation module is to automatically construct and mesh a piston finite element model similar to Fig. 39. The meshing of a piston solid model is made using two type of elements, hexahedral (8 nodes) and pentahedral (6 nodes). Specific loads and boundary conditions are imposed on the model in order to carry out the finite element analysis in the next module.

5.4.2 Load/Boundary Conditions

Input data of the ambient temperatures and convection coefficients are distributed into four regions on the piston: 1) crown top surface 2) piston ring pack region 3) piston skirt region 4) under crown region. Published works present these thermal data obtained through measurement or numerical calculation [55,86,91,100,128,130]. Figure 44 shows the specification of temperature with respective heat convection coefficient on the open surface of elements.

The piston FE model is constrained at its four nodes that specify the piston pin axis locations to zero displacements; and at its center node at the top of crown to 1 degree of freedom (DOF) along vertical axis. A unit pressure is applied uniformly over the top surface of piston crown, normal to the face of elements (refer to Fig. 45). A unit acceleration with respect to its global Cartesian coordinates is also specified uniformly over the whole model to account for inertia-induced distortion.

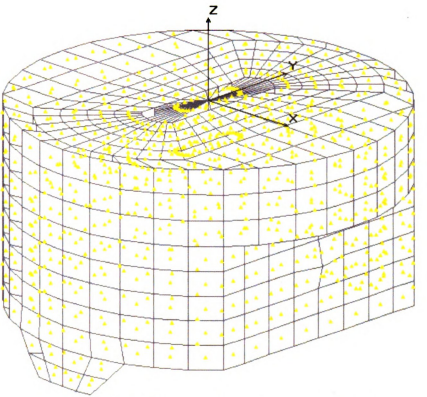

FIGURE 44. Thermal boundary conditions

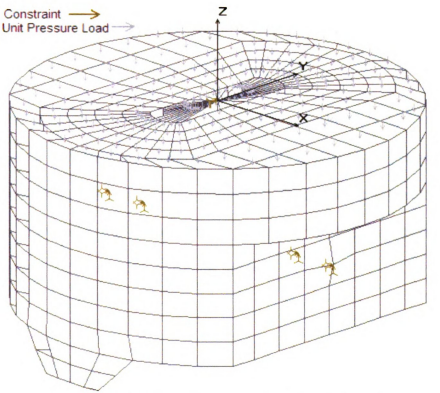

FIGURE 45. Constraints and unit pressure load

5.5 Thermal and Static Analyses

The next module consists of the finite element analysis solvers for the thermal and static analyses. It is used to solve for the temperature distribution and the distortion of the piston model. The piston distortion due to thermal load is computed in this module. Assuming steady state thermal conditions, the thermal distortion computed in this module will be repeatedly used throughout the entire cyclic analysis. However, the distortion due to the inertia and the cylinder gas pressure are transient. In order to save computational time, the approach suggested by Zhu [133,134] is used to calculate numerically the distortion due to inertia and cylinder gas pressure. The influence coefficient matrices, defining the piston skirt deformation caused by unit cylinder gas pressure and unit gravitational acceleration, is computed and stored for the next module. The module involves the calculation of piston dynamics coupled with the piston's elastohydrodynamic behavior inside the cylinder bore.

For the purpose of verifying the accuracy of calculation, a piston FE model is exported to a commercial software, COSMOS GeoSTAR, for similar thermal and static analyses. The computation from the built-in solvers are validated to be accurate as proven in the node-to-node comparison of the temperature and distortion results, as shown in Figures 46 and 47.

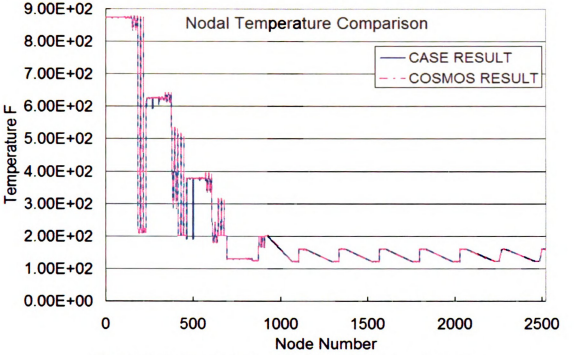

FIGURE 46. Node-to-node temperature comparison

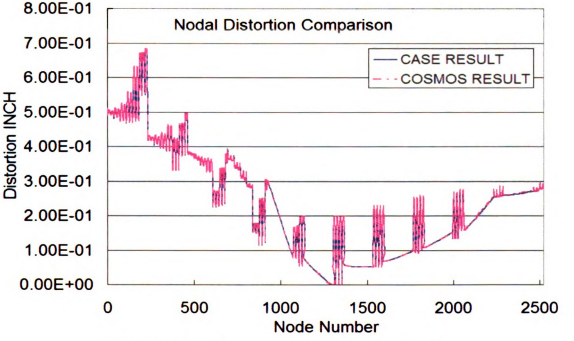

FIGURE 47. Node-to-node distortion comparison

5.6 Piston Skirt EHL Analysis

At every degree of crank angle, the input cylinder gas pressure and the calculated piston acceleration are multiplied with the influence coefficient matrices to obtain the resultant displacements at each finite element node along with the steady-state thermal distortion calculated from the previous module. On top of that, the distortion due to the hydrodynamic lubrication pressure load needs to be calculated. Because of the non-uniformity of the hydrodynamic lubrication pressure that impact the piston skirt surface on the thrust and anti-thrust sides, the 3-D static analysis for the piston distortion due to the hydrodynamic load needs to be conducted at every crank angle. Therefore, the effective piston distortion is due to loads from the cylinder gas pressure acting vertically on the piston crown, the inertial load acting vertically at the piston pin axis, the thermal load due to temperature variation over the piston body, and the lubricant hydrodynamic pressures acting radially over the area of skirt/bore conjunction.

By treating the skirt/bore interface as a slider bearing and assuming incompressible lubricant, the 2-D Reynolds equation, Eq. (24) can be applied to solve for the hydrodynamic lubrication over the piston skirt/bore surface both on thrust and antithrust sides using the finite element approach [133,87,88].

$$\frac{\partial}{\partial x}\left(\frac{h^3}{\mu}\frac{\partial p}{\partial x}\right)+\frac{\partial}{\partial z}\left(\frac{h^3}{\mu}\frac{\partial p}{\partial z}\right) = 6U\frac{\partial h}{\partial x}+12\frac{\partial h}{\partial t} \tag{24}$$

5.7 Equation of Motion

The static and dynamic loads that act on the piston as functions of crank angle are shown in Fig. 48. These loading factors are affecting, individually as well as collectively, the orientation and impact of the piston at every crank angle. The moment and forces of the piston induced from the loading factors are computed at every increment of computation over a complete cycle of engine analysis. The piston moves along the cylinder bore in one of several modes as shown in Fig. 49. The piston can come into contact with the bore at a top contact point or a bottom contact point on either the thrust side or antithrust side of the piston. If the piston is in contact with the bore at both contact points, this is denoted as Mode 1 (two-point contact). If neither contact point is in contact with the bore, this is denoted as Mode 4 (free contact). In Mode 2 (high-point contact), the piston is in contact with the bore at the top contact point, but not the bottom contact point. The piston is then free to pivot (rotate) about the top contact point. In Mode 3 (low-point contact), the piston is in contact with the bore at the bottom contact point, but not the top contact point. The piston is then free to pivot (rotate) about the bottom contact point. In order to determine the contact forces (F_1 and F_2), the piston lateral acceleration ($\ddot{x}_2$) and the piston rotational acceleration ($\ddot{\beta}$), moments are summed about the crank pin location (Pt. 1) and the piston pin location (Pt. 2). Rotational moments and acceleration ($\ddot{\beta}$) are considered positive clockwise. Forces and lateral piston acceleration ($\ddot{x}_2$) are considered positive to

the right. Summing moments about Pt. 1 for the piston and the connecting rod loads gives:

$$
\begin{aligned}
&-P_v(L_2+u)-P_H(L_1+f)+F_1(L_1+a)+F_2(L_1-b)+F_3(L_1+d) \\
&-F_4(L_1-h)+J_T\mu F_1(L_2+u+x_2+J_{ST}R)+J_B\mu F_2(L_2+u+x_2+J_{SB}R) \\
&-m_3g(L_2-e+u)+m_3\ddot{y}_3(L_2-e+u)-m_3\ddot{x}_3(L_1+c)+J_TF_7(L_2+u+R) \\
&+J_TF_8(L_2+u-R)-m_2\ddot{x}_2(L_1)+m_2\ddot{y}_2(L_2)+m_{rod}s^2\ddot{\phi}-I_3\ddot{\beta}+I_{rod}\ddot{\phi}=0
\end{aligned}
\tag{25}
$$

Summing moments about Pt. 2 for the piston and the connecting rod loads gives:

$$
\begin{aligned}
&-P_v(u)-P_H(f)+F_1(a)-F_2(b)+F_3(d)-F_4(h)+J_T\mu F_1(u+x_2+J_{ST}R) \\
&+J_B\mu F_2(u+x_2+J_{SB}R)+J_TF_7(R+u)-J_TF_8(R-u)+m_3g(e-u) \\
&-m_3\ddot{y}_3(e-u)-m_3\ddot{x}_3(c)-M_{pin}-I_3\ddot{\beta}=0
\end{aligned}
\tag{26}
$$

Velocity direction coefficients are denoted as J_T and J_B. Side contact coefficients are denoted as J_{ST} and J_{SB}. $J_{ST}=1$ if top contact is on the thrust side and $J_{ST}=-1$ if top contact is on the antithrust side. Coefficients are similar for bottom contact friction forces. Additional sign conventions are:

1. Crank angle (θ) - positive clockwise
2. Connecting rod angle (ϕ) - positive counterclockwise
3. Piston axial location from top of deck (y) - positive down
4. Piston axial velocity ($\dot{y}$) - positive down
5. Piston axial acceleration ($\ddot{y}$) - positive down

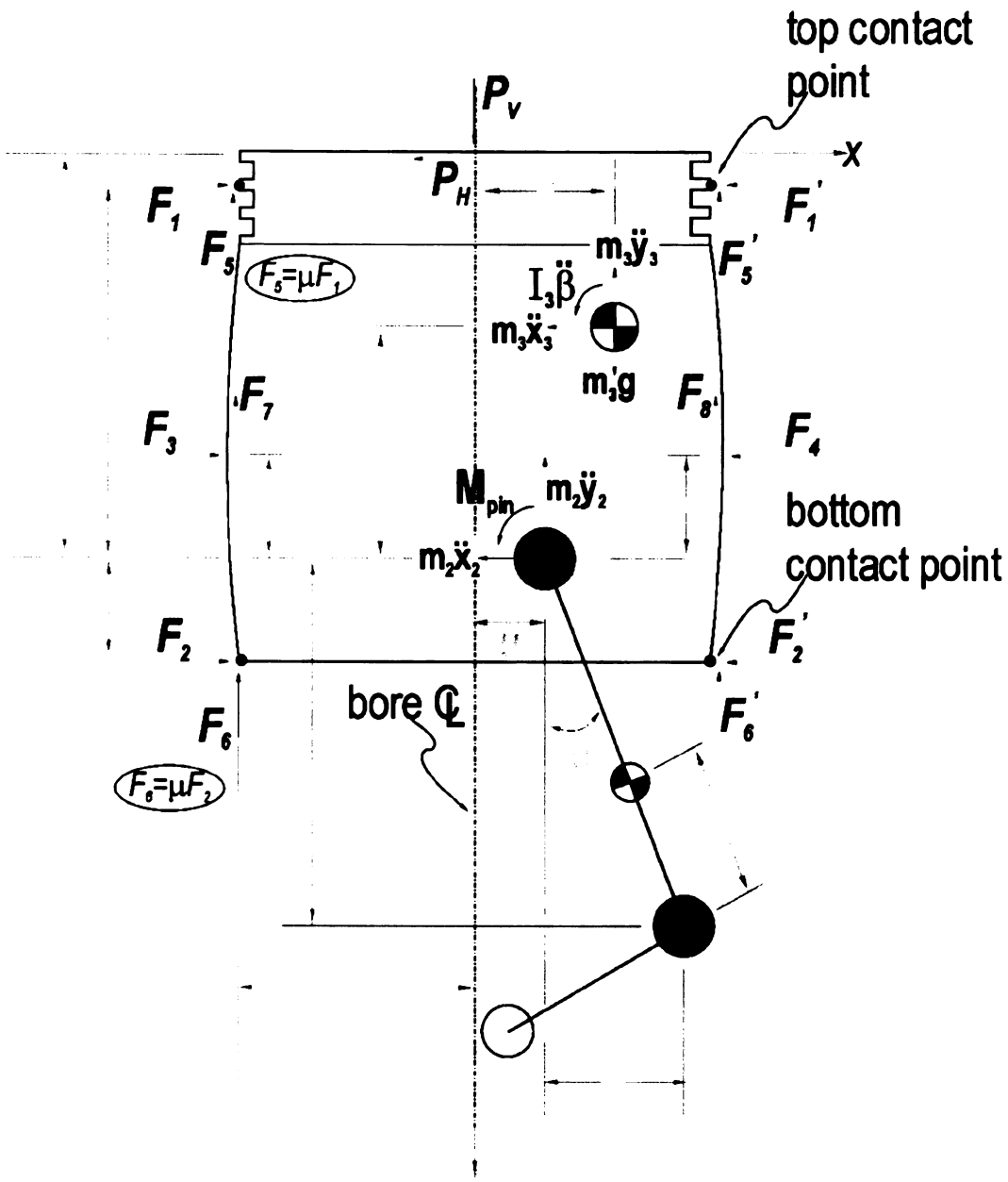

FIGURE 48. Imposed loads and dynamics of piston during operation

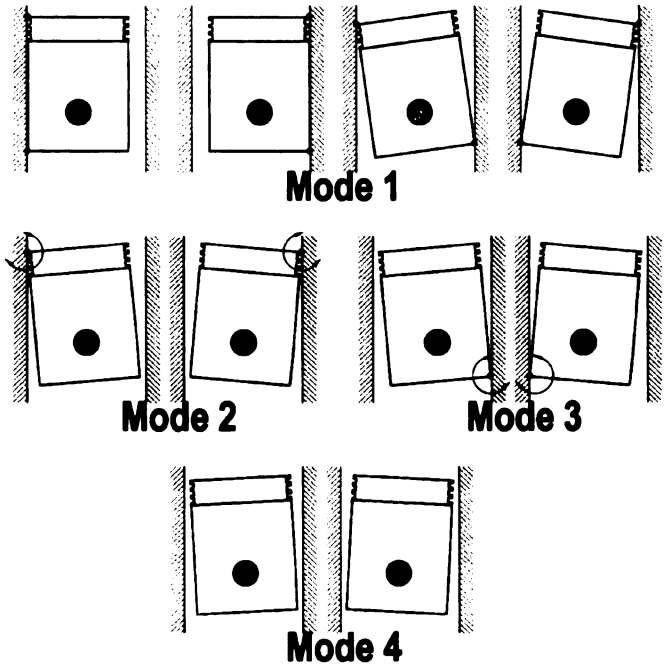

FIGURE 49. Motion modes

By introducing the following new terms:

$$J_V = J_T = J_B \tag{27}$$

$$\ddot{x}_3 = \ddot{x}_2 + \ddot{\beta}(c) \tag{28}$$

$$\ddot{y}_3 = \ddot{y} + \ddot{\beta}(e-c) \tag{29}$$

$$W_{pis} = m_3 g \tag{30}$$

Equation (25) can be rewritten as

$$\begin{aligned} &-P_v(L_2+u)-P_H(L_1+f)+F_1(L_1+a)+F_2(L_1-b)+F_3(L_1+d) \\ &-F_4(L_1-h)+J_V\mu F_1(L_2+u+x_2+J_{ST}R)+J_V\mu F_2(L_2+u+x_2+J_{SB}R) \\ &-(L_2-e+u)+m_3[\ddot{y}+\ddot{\beta}(e-u)](L_2-e+u)-m_3[\ddot{x}_3+\ddot{\beta}(c)](L_1+c) \\ &+J_V F_7(L_2+u+R)+J_V F_8(L_2+u-R)-m_2\ddot{x}_2(L_1)+m_2\ddot{y}_2(L_2) \\ &+m_{rod}(s^2)\ddot{\phi}-I_{pis}\ddot{\beta}+I_{rod}\ddot{\phi}=0 \end{aligned} \tag{31}$$

or

$$(H_1)F_1 + (H_2)F_2 + (H_3)\ddot{x}_2 + (H_4)\ddot{\beta} = (H_5) \tag{32}$$

and Equation (26) can be rewritten as

$$\begin{aligned} &-P_v(u) - P_H(f) + F_1(a) - F_2(b) + F_3(d) - F_4(h) + J_V\mu F_1(u + x_2 + J_{ST}R) \\ &+ J_V\mu F_2(u + x_2 + J_{SB}R) + J_T F_7(R + u) - J_T F_8(R - u) + W_{pis}(e - u) \\ &- m_3[\ddot{y} + \ddot{\beta}(e - u)](e - u) - m_3(\ddot{x}_2 + \ddot{\beta}(c))(c) - M_{pin} - I_{pis}\ddot{\beta} = 0 \end{aligned} \tag{33}$$

or

$$(H_6)F_1 + (H_7)F_2 + (H_8)\ddot{x}_2 + (H_9)\ddot{\beta} = (H_{10}) \tag{34}$$

where

$$H_1 = L_1 + a + J_V\mu(L_2 + u + x_2 + J_{ST}R) \tag{35}$$

$$H_2 = L_1 - b + J_V\mu(L_2 + u + x_2 + J_{SB}R) \tag{36}$$

$$H_3 = -m_3(L_1 + c) - m_2(L_1) \tag{37}$$

$$H_4 = -m_3(L_2 - e + u)(e - u) - m_3(L_1 + c)(c) - I_{pis} \tag{38}$$

$$\begin{aligned} H_5 = {} & P_V(L_2 + u) + P_H(L_1 + f) - [I_{rod} + m_{rod}(s^2)]\ddot{\phi} - F_3(L_1 + d) \\ & + F_4(L_1 + h) - J_V F_7(L_2 + u + R) - J_V F_8(L_2 + u - R) \\ & + W_{pis}(L_2 - e + u) - m_3\ddot{y}(L_2 - e + u) - m_2\ddot{y}(L_2) \end{aligned} \tag{39}$$

$$H_6 = a + J_V\mu(u + x_2 + J_{ST}R) \tag{40}$$

$$H_7 = -b + J_V\mu(u + x_2 + J_{SB}R) \tag{41}$$

$$H_8 = -m_3(c) \tag{42}$$

$$H_9 = -m_3(e - u)^2 - m_3(c)^2 - I_{pis} \tag{43}$$

$$\begin{aligned} H_{10} = {} & P_V(u) + P_H(f) - F_3(d) + F_4(h) - J_V F_7(u + R) + J_V F_8(R - u) \\ & - W_{pis}(e - u) + m_3\ddot{y}(e - u) + M_{pin} \end{aligned} \tag{44}$$

Referring to Fig. 49, the boundary conditions for each motion mode can be expressed as following:

Mode 1:

$$\ddot{x}_2 = 0 \text{ and } \ddot{\beta} = 0 \tag{45}$$

Mode 2:

$$F_2 = 0 \text{ and } \ddot{x}_2 = -a\ddot{\beta} \tag{46}$$

Mode 3:

$$F_1 = 0 \text{ and } \ddot{x}_2 = b\ddot{\beta} \tag{47}$$

Mode 4:

$$F_1 = 0 \text{ and } F_2 = 0 \tag{48}$$

For Mode 1, solving Equations (32) and (34) with the boundary conditions of Equations (45) yields,

$$F_1 = \frac{H_5H_7 - H_2H_{10}}{H_1H_7 - H_2H_6} \tag{49}$$

$$F_2 = \frac{H_5H_6 - H_1H_{10}}{-H_1H_7 + H_2H_6} \tag{50}$$

For Mode 2, solving Equations (32) and (34) with the boundary conditions of Equations (46) yields,

$$F_1 = \frac{H_5(-H_8a + H_9) - H_{10}(-H_3a + H_4)}{H_1(-H_8a + H_9) - H_6(-H_3a + H_4)} \tag{51}$$

$$\ddot{\beta} = \frac{-H_1 H_{10} + H_5 H_6}{-H_1(-H_8 a + H_9) + H_6(-H_3 a + H_4)} \tag{52}$$

For Mode 3, solving Equations (32) and (34) with the boundary conditions of Equations (47) yields,

$$F_2 = \frac{H_5(H_8 b + H_9) - H_{10}(H_3 b + H_4)}{H_2(H_8 b + H_9) - H_7(H_3 b + H_4)} \tag{53}$$

$$\ddot{\beta} = \frac{-H_2 H_{10} + H_5 H_7}{-H_2(H_8 b + H_9) + H_7(H_3 b + H_4)} \tag{54}$$

For Mode 4, solving Equations (32) and (34) with the boundary conditions of Eq. (48) yields,

$$\ddot{x}_2 = \frac{H_5 H_9 - H_4 H_{10}}{H_3 H_9 - H_4 H_8} \tag{55}$$

$$\ddot{\beta} = \frac{H_5 H_8 - H_3 H_{10}}{-H_3 H_9 + H_4 H_8} \tag{56}$$

The piston motion is ready to be solved with all the known values of the input piston geometry and the calculated external loads except with the unknown moment, M_{pin}, developed due to the friction between the piston and the piston pin. Referring to Fig. 50, M_{pin} can be determined through the finding of the pin force, A, first. The direction of M_{pin} depends on the relative angular velocity of the piston, $\dot{\beta}$, and the connecting rod $\dot{\phi}$. An iterative approach is adopted to determine the lateral and the axial components of the pin force, denoted as A_1

and A_2 respectively. Summing piston forces in the lateral (x) and axial (y) directions yields

$$\begin{aligned}\sum F_x &= A_1 + J_p\mu_p A_2 - F_1 - F_2 + m_3\ddot{x}_3 \\ &\quad + P_H - F_3 + F_4 = 0\end{aligned} \tag{57}$$

$$\begin{aligned}\sum F_y &= A_2 - J_p\mu_p A_1 + J_V\mu(F_1 + F_2) \\ &\quad + m_3\ddot{y}_3 + -P_V - m_3 g + F_7 + F_8 = 0\end{aligned} \tag{58}$$

Rearranging Eq (57) yields

$$\begin{aligned}&A_1 + J_p\mu_p A_2 \\ &= F_1 + F_2 - m_3\ddot{x}_3 - P_H + F_3 - F_4\end{aligned} \tag{59}$$

or can be in the form of

$$A_1 + C_1 A_2 = C_2 \tag{60}$$

Rearranging Eq (58) yields

$$\begin{aligned}-J_p\mu_p A_1 + A_2 &= -J_V\mu(F_1 + F_2) - m\ddot{y}_3 \\ &\quad + P_V + m_3 g - F_7 - F_8\end{aligned} \tag{61}$$

or can be in the form of

$$C_3 A_1 + A_2 = C_4 \tag{62}$$

where

$$C_1 = J_p\mu_p \tag{63}$$

$$C_2 = F_1 + F_2 - m_3\ddot{x}_3 - P_H + F_3 - F_4 \tag{64}$$

$$C_3 = -J_p\mu_p \tag{65}$$

$$C_4 = -J_V\mu(F_1 + F_2) - m\ddot{y}_3 + P_V + m_3 g - F_7 - F_8 \tag{66}$$

Solving for A_1 and A_2 results in

$$A_1 = \frac{C_1C_4 - C_2}{C_1C_3 - 1} \tag{67}$$

$$A_2 = \frac{C_2C_3 - C_4}{C_1C_3 - 1} \tag{68}$$

Then, the friction moment M_{pin} can be determined as follows:

$$M_{pin} = J_p\frac{\mu_p d_p}{2}\sqrt{A_1^2 + A_2^2} \tag{69}$$

With all equations needed for the piston dynamics derived at every crank angle, the piston contact forces (F_1 and F_2) and the piston accelerations ($\ddot{x}_2$ and $\ddot{\beta}$) are determined from the moment relationships derived previously in Equations (49) to (56) by initializing M_{pin} equal to zero. The moment M_{pin} can now be calculated using Eq. (69) and used in determining the new contact forces and the piston accelerations as well as new values for A_1 and A_2 using Equations (67) and (68). The process is repeated until convergence is achieved.

The piston accelerations ($\ddot{x}_2$ and $\ddot{\beta}$) and the contact forces (F_1 and F_2) are determined at every crank angle throughout a four stroke cycle. The lateral velocity and position of the piston are calculated by integrating $\ddot{x}_2$ and $\ddot{\beta}$ over the appropriate time step. The location of the top and bottom of the piston skirt is continually monitored so that the mode of the piston motion can be determined at every crank angle.

5.8 Piston Impact

When the piston impacts the cylinder bore, the kinetic energy of the piston at impact is determined under the assumptions that the velocity of the point on the piston at which impact occurs is reduced to zero (rebound does not occur); and if the piston is free in the bore prior to impact, then the angular velocity of the piston after impact is determined according to the principle of conservation of angular momentum.

Piston angular velocity after impact may be determined as follows. Consider the system just prior to impact, with the piston having a horizontal velocity ($\dot{x}_3$) and angular velocity ($\dot{\beta}$). The mass at point 2 (piston pin location) is m_{eq} and is equal to the piston pin mass (m_2) plus the equivalent connecting rod mass located at point 2. The mass (m_{eq}) has velocity $\dot{x}_2$. The angular momentum just before impact with respect to the point (*P*) of impact (see Fig. 51) is given by

$$H_a = m_3\dot{x}_3(b+c) + I_3\dot{\beta} + m_{eq}\dot{x}_2 b \tag{70}$$

After impact the velocity of the piston at *P* is zero, and the piston rotates about the point of contact at the new angular velocity ($\dot{\beta}'$). Thus the angular momentum after impact is given by

$$H_a' = m_3\dot{x}_3'(b+c) + I_3\dot{\beta}' + m_{eq}\dot{x}_2' b \tag{71}$$

but from Fig. 51, one has

$$\dot{x}_2' = b\dot{\beta}' \quad \text{and} \quad \dot{x}'_3 = (b+c)\dot{\beta}' \tag{72}$$

Then

$$H_a' = I_3\dot{\beta}' + m_{eq}b^2\dot{\beta}' + m_3(b+c)^2\dot{\beta}' \tag{73}$$

Applying the principle of conservation of angular momentum,

$$H_a = H_a' \tag{74}$$

gives

$$\dot{\beta}' = \frac{m_3\dot{x}(b+c) + I_3\dot{\beta} + m_{eq}\dot{x}_2 b}{I_3 + m_3(b+c)^2 + m_{eq}b^2} \tag{75}$$

Eq. (75) defines the angular velocity of the piston after impact.

As a measure of the intensity of each impact, the change in kinetic energy of the piston is calculated from

$$\text{Kinetic Energy Lost at Impact} = KE_1 - KE_2 \tag{76}$$

where

$$KE_1 = 0.5(m_3\dot{x}_3^2 + m_3\dot{y}_3^2 + m_{eq}\dot{x}_2^2 + I_3\dot{\beta}^2)$$
$$= \textit{Kinetic energy of piston before impact} \tag{77}$$

$$KE_2 = 0.5(m_3\dot{x}_{3a}^2 + m_3\dot{y}_{3a}^2 + m_{eq}\dot{x}_{2a}^2 + I_3\dot{\beta}_a^2)$$
$$= \textit{Kinetic energy of piston after impact} \tag{78}$$

where the subscript ***a*** refers to the velocities after impact.

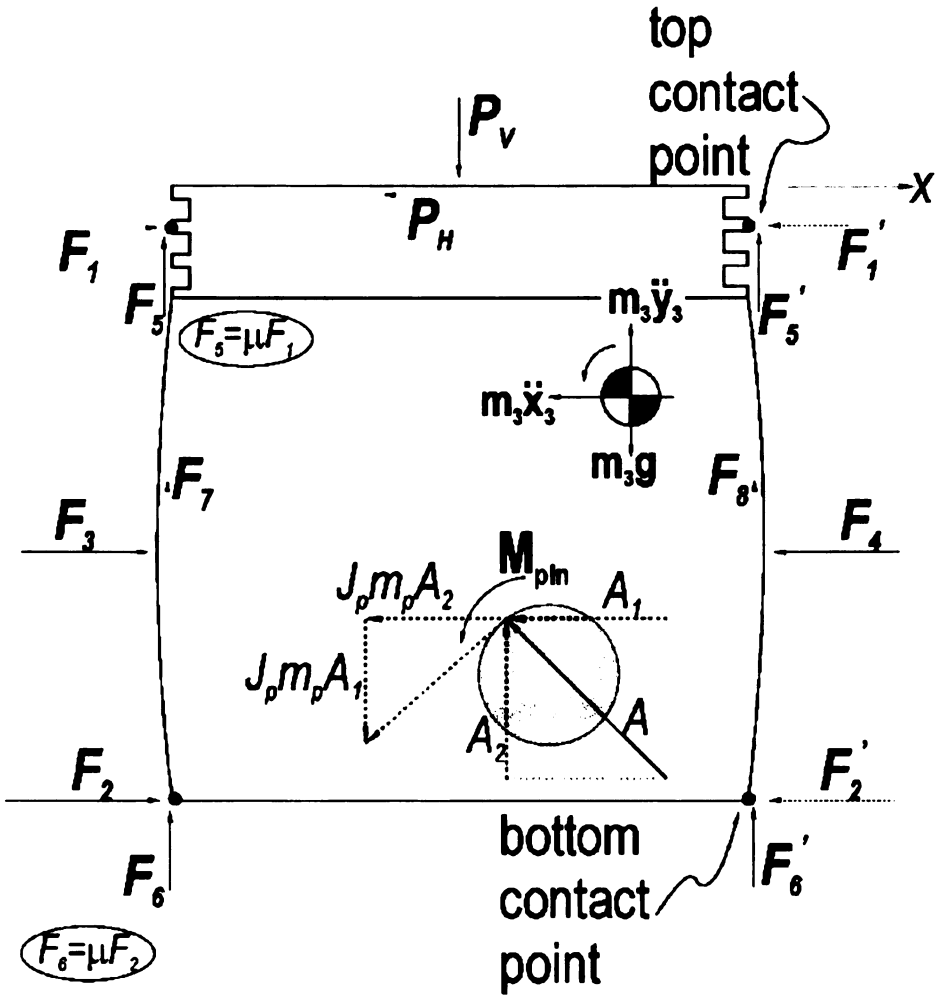

FIGURE 50. Pin forces acting on piston

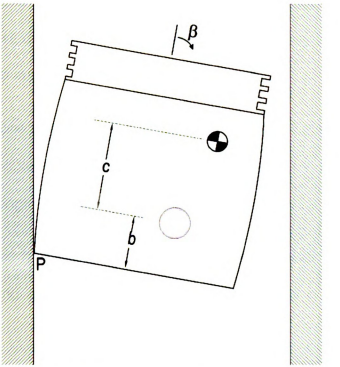

FIGURE 51. Piston impact with cylinder bore

5.9 Numerical Algorithm for Piston Skirt EHL and Dynamic Analyses

The lubricant film thicknesses and pressures (on the thrust and antithrust sides of the piston at the end of the crank angle increment) are calculated according to the following procedure:

1. Skirt distortions due to lubricant pressures are determined using nodal lubricant pressures that exist at the beginning of the crank angle increment. Additional skirt distortions are added to the lubricant pressure distortions. These include skirt profile (including ovality) and skirt thermal distortions which remain constant over the four-stroke cycle.

2. Skirt distortions due to combustion pressures are determined by multiplying the gas pressure distortion vector (influence coefficient) by the actual pressure occurring at the current crank angle.

3. Skirt distortions due to piston inertia loads are determined by multiplying the inertia distortion vector (influence coefficient) by the piston acceleration at the current crank angle.

4. Gas pressure and inertia distortions are combined with all other distortion vectors resulting in a skirt contour at the end of the current crank angle increment.

5. The skirt contour and lateral piston location in the bore and piston tilt are then used to determine lubricant film thickness on the thrust and antithrust sides of the piston. With the axial velocity of the piston at the end of the current crank angle increment known, the lubricant pressures at the end of the current crank angle increment are determined.

6. The resultant loads and shear forces as well as gas pressure loads and inertia loads are computed at the current crank angle.

7. The procedure is repeated for all crank angles.

5.10 Preliminary Results and Discussions

Simulations using this piston software are conducted for a boosted-motored four-stroke engine at two operating conditions: 1500 RPM 2 PSI Boost

and 3000 RPM 2 PSI Boost. The intake throttle is regulated with boosted pressures in order to imitate the firing pressure trace. Some basic input data are listed as follows:

Nominal piston diameter	**88.95 mm**
Nominal cylinder bore diameter	**91.00 mm**
Stroke	**90.00 mm**
Length of connecting rod	**169.20 mm**
Piston height	**50.10 mm**
Piston skirt height	**27.00 mm**
Average pin boss thickness	**13.50 mm**
Average crown thickness	**12.10 mm**
Piston skirt tab height	**3.50 mm**
Piston skirt width	**65.00 mm**
Piston skirt tab width (top)	**40.00 mm**
Piston skirt tab width (bottom)	**29.00 mm**

Bore distortion and other non-symmetric boundary conditions are not considered in the present analysis so that the piston performance under the effect of skirt elastohydrodynamic lubrication can be studied more clearly. The cylinder gas pressure traces for the two operating conditions are plotted in Fig. 52 as functions of crank angle. The intake stroke start at 0 degree crank angle and the exhaust stroke ends at 720 degree crank angle.

5.10.1 Piston Dynamics

Figure 53 shows the solution of the cyclic piston trajectory at 1500 RPM 2 PSI Boost and at 3000 RPM 2 PSI Boost condition. The antithrust side is at the positive upper bound and the thrust side is at the negative lower bound in the

plots. The upper and lower bounds are the calculated effective clearance allowable for the piston to move laterally taking into consideration the piston and bore distortion, piston skirt profile and piston ovality. More vigorous piston motion is observed at the 3000 RPM 2 PSI Boost condition than at the 1500 RPM 2 PSI condition. The drastic direction change of the pin movement in particular near 360 degree crank angle (CA) signifies the event of high piston impact. The change of piston velocity at TDC and BDC (0, 180, 360, 540, 720 degree CA) and the change of piston acceleration at midstroke (90, 270, 450, 630 degree CA) seem to initiate changes in the piston pin lateral position. This is understandable, as it is known that the shift in velocity direction affects the balance of piston momentum, and the change in acceleration direction affects the piston load equilibrium.

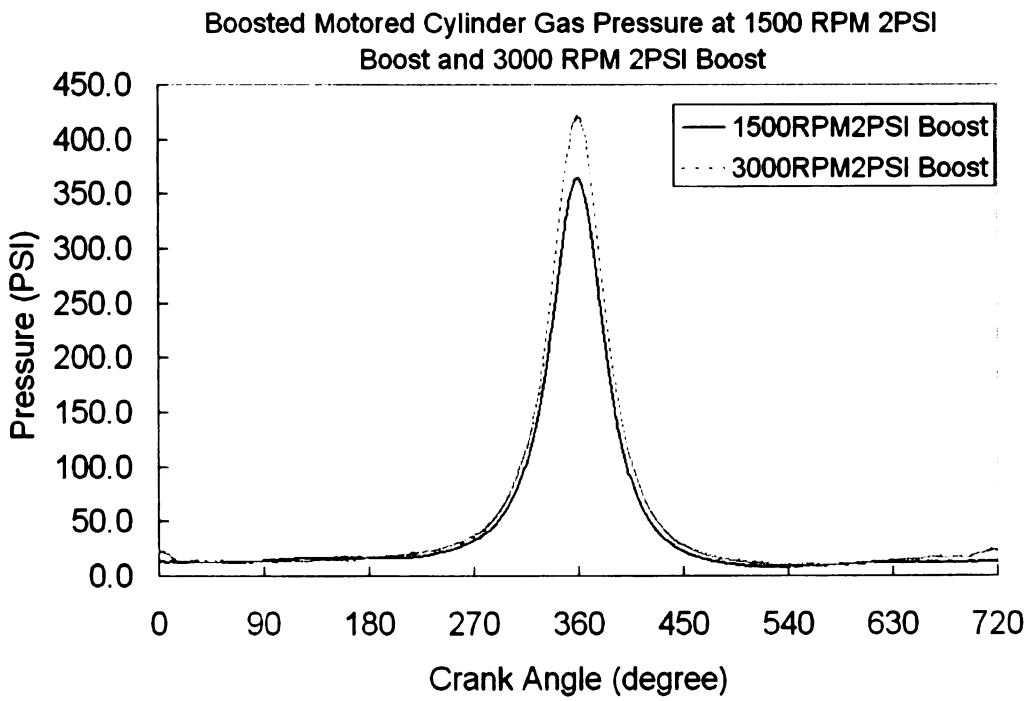

FIGURE 52. Cylinder gas pressure traces

Figure 54 illustrates the cyclic piston tilting motion. Higher engine speed is seen to cause more piston rotational motion. It is also observed that the piston rotates at the highest magnitude of allowable angle (constrained by the piston/ bore clearance) during 3000 RPM throughout the whole engine cycle, but a small degree of piston rotation is seen at some crank angles during the 1500 RPM operation. This implies that during high engine speed, piston momentum is sufficiently high to permit a complete change of piston orientation, from one motion mode to another opposite mode.

With higher kinematics at higher engine speeds, one can expect to see greater contact forces impacting the piston as shown in Fig. 55, which shows the contact forces that take place at the top and bottom contact points. Positive magnitude designates the contact point at the thrust side, and negative at the antithrust side, for both top and bottom contact points. The results again show that the engine speed contributes to the increase of contact forces due to more dynamic piston motion at higher speed. The contact force experienced by the piston at 3000 RPM is about four times higher than at 1500 RPM.

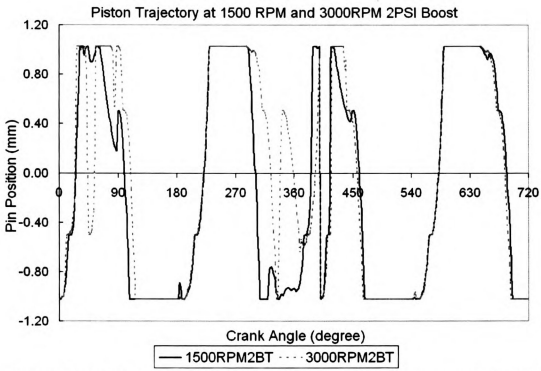

FIGURE 53. Cyclic piston lateral movement at 1500 RPM and 3000 RPM 2 PSI Boost

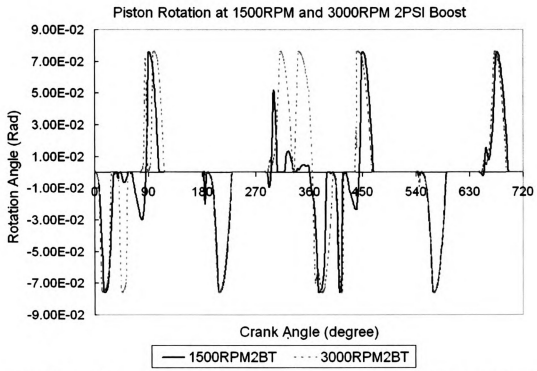

FIGURE 54. Cyclic piston rotation at 1500 RPM and 3000 RPM 2 PSI Boost

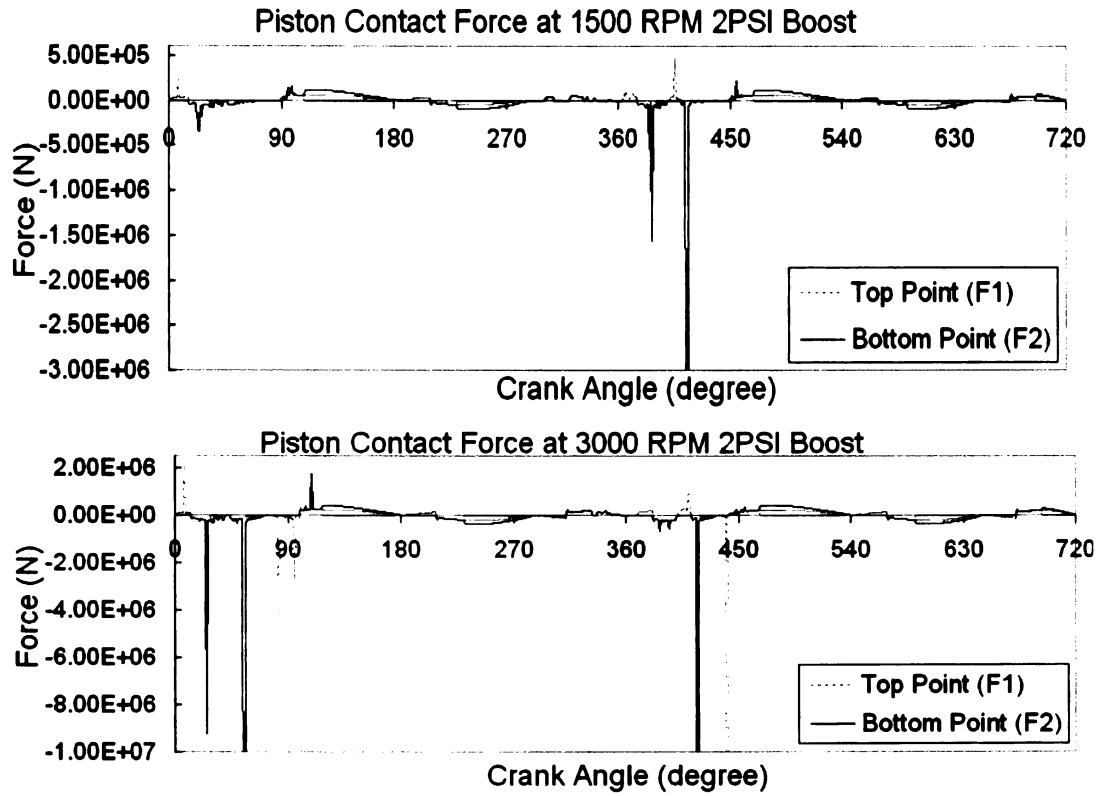

FIGURE 55. Piston contact forces on thrust and anti-thrust sides

5.10.2 Piston Skirt Elastohydrodynamic Lubrication

Figure 56 gives the lubrication forces on the thrust and anti-thrust sides. The lubrication forces are computed from the integration of hydrodynamic lubrication pressure over the bearing area of thrust and anti-thrust sides. Higher lubrication force is observed at 3000 RPM than at 1500 RPM due to the fact that Reynolds hydrodynamic pressure is proportional to the sliding speed at two contact surfaces. In addition, with the lubrication analysis coupled with the piston elasticity and dynamics, one can also expect higher hydrodynamic pressure due to the squeeze film effect, which is a function of the rate of radial surface

movement either due to the piston lateral motion or the skirt radial elastic deformation.

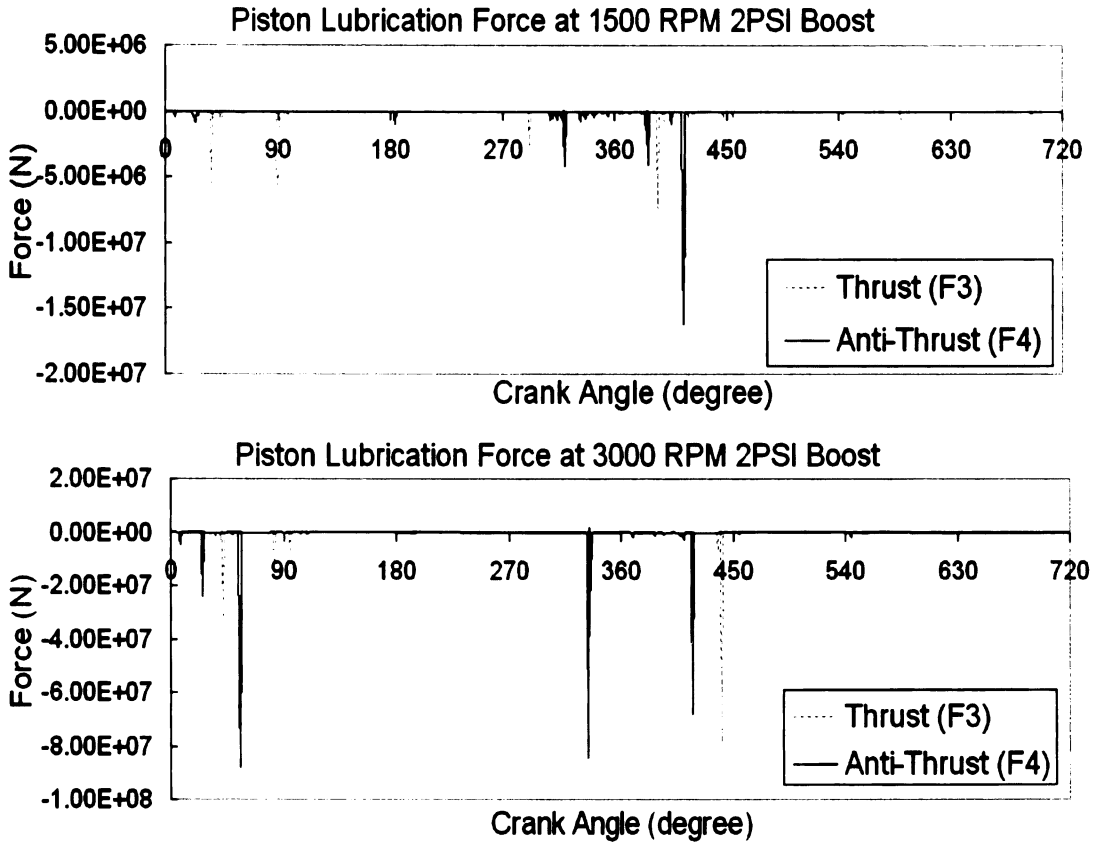

FIGURE 56. Piston lubrication forces on thrust and anti-thrust sides

Figure 57 gives the magnitude of contours of hydrodynamic lubrication pressures computed at 5 degree crank angle during the 1500 RPM 2 PSI Boost analysis. Imposing these pressures on the 3-D piston FE model results in the distortion of the piston skirts as shown in Figure 58. Positive distortion represents the expansion of the body structure and negative distortion means contraction. This also means that positive distortion will result in smaller skirt/bore clearances and vice versa. The different pressure profiles on the thrust and anti-thrust sides

are due to the difference in skirt/bore clearance as a result of distortion from pressure, inertia and thermal loads. Without considering the non-symmetric influence from bore distortion or temperature, symmetric results about the axis plane normal to the piston pin are expected.

Figures 59 and 60 give the magnitude of contours of hydrodynamic lubrication pressures and resultant distortions computed at 5 degree crank angle during the 3000 RPM 2 PSI Boost analysis. Similar distribution profiles of hydrodynamic pressure and distortion are observed at the two cases. Comparing the magnitude of hydrodynamic distribution, one can observe that the 3000 RPM engine speed contributes to better hydrodynamic lubrication than the 1500 RPM condition.

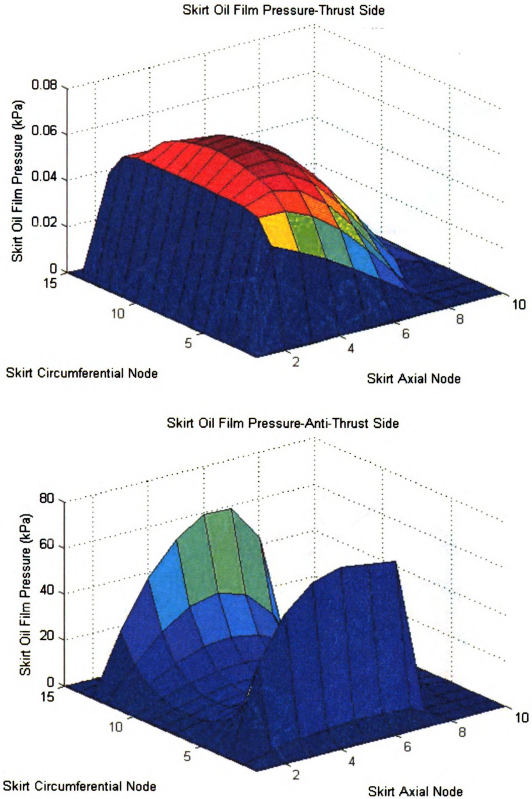

FIGURE 57. Piston skirt thrust and anti-thrust oil film pressure at 5 degree CA, 1500 RPM 2 PSI Boost

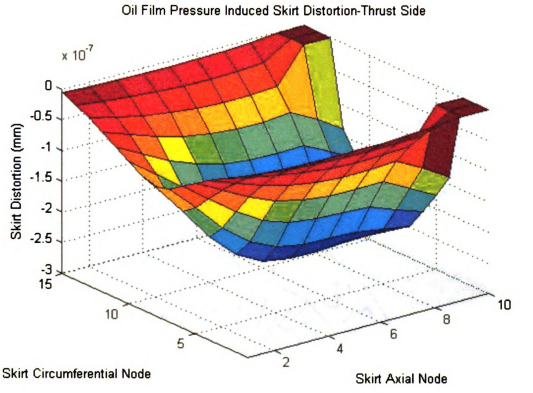

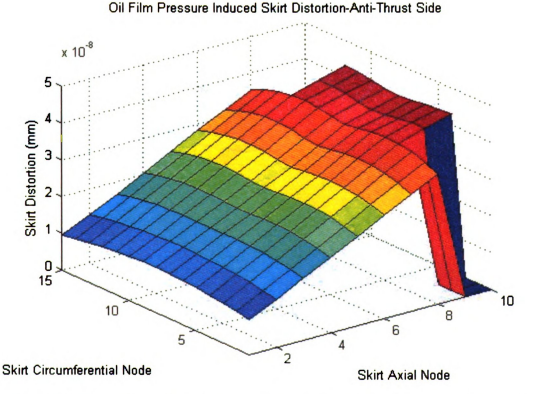

FIGURE 58. Piston skirt thrust and anti-thrust side distortion due to oil film pressure at 5 degree CA, 1500 RPM 2 PSI Boost

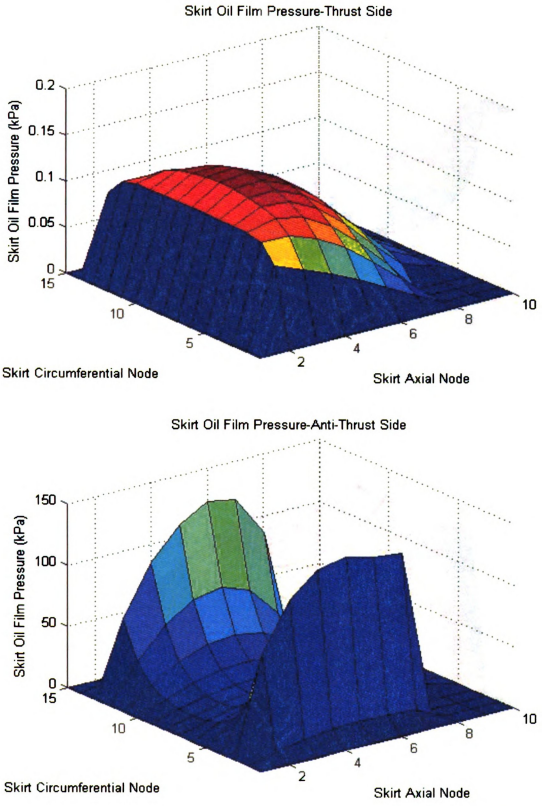

FIGURE 59. Piston skirt thrust and anti-thrust oil film pressure at 5 degree CA, 3000 RPM 2 PSI Boost

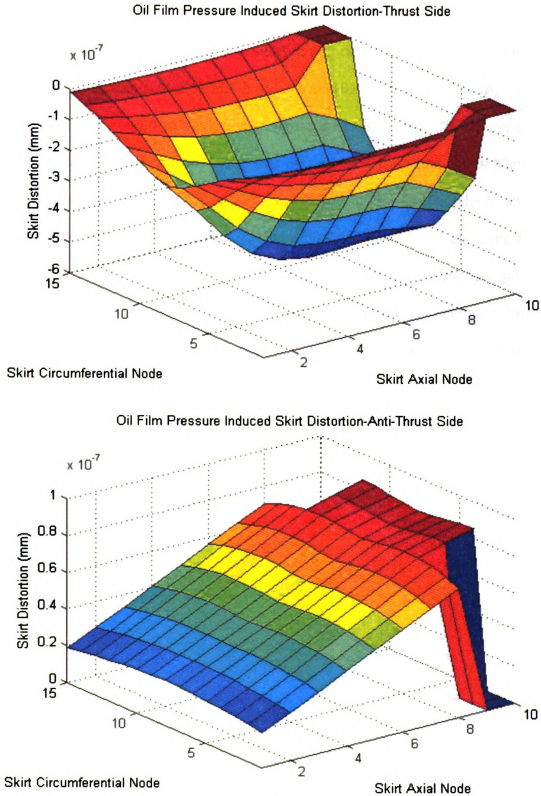

FIGURE 60. Piston skirt thrust and anti-thrust side distortion due to oil film pressure at 5 degree CA, 3000 RPM 2 PSI Boost

An interesting observation is seen at 365 degree CA during the 3000 RPM 2PSI simulation, as illustrated in Figures 61 and 62. At 365 degree CA, the piston movement is observed to be at a very vigorous stage because of the impact from the peak pressure, as shown in Figures 53 and 54. The piston top is tilting away from the anti-thrust side, resulting in a divergent surface profile which acts like a scrapper piston ring. As a result, no hydrodynamic pressure is generated on the anti-thrust side of the piston skirt. However, the hydrodynamic pressures generated at the thrust side, applied in the piston 3-D model, produce distortion on the whole piston structure. Hence, distortion is seen at both thrust and anti-thrust sides of the piston skirt.

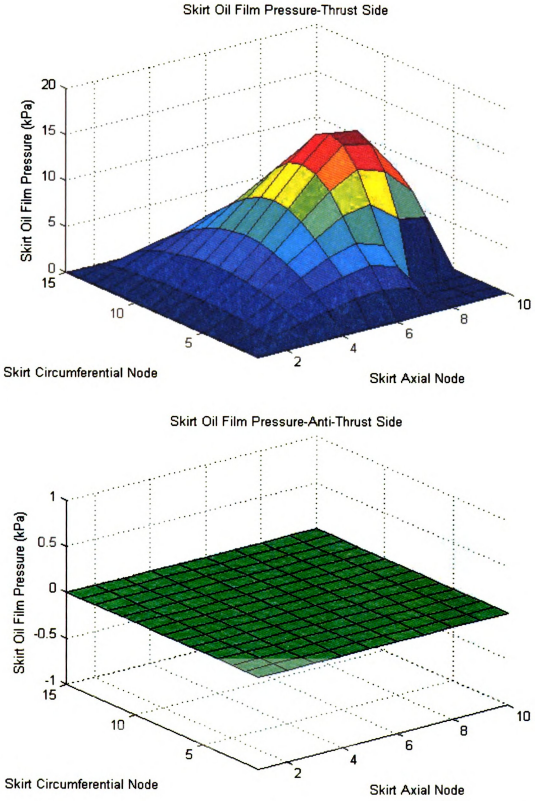

FIGURE 61. Piston skirt thrust and anti-thrust oil film pressure at 365 degree CA, 3000 RPM 2 PSI Boost

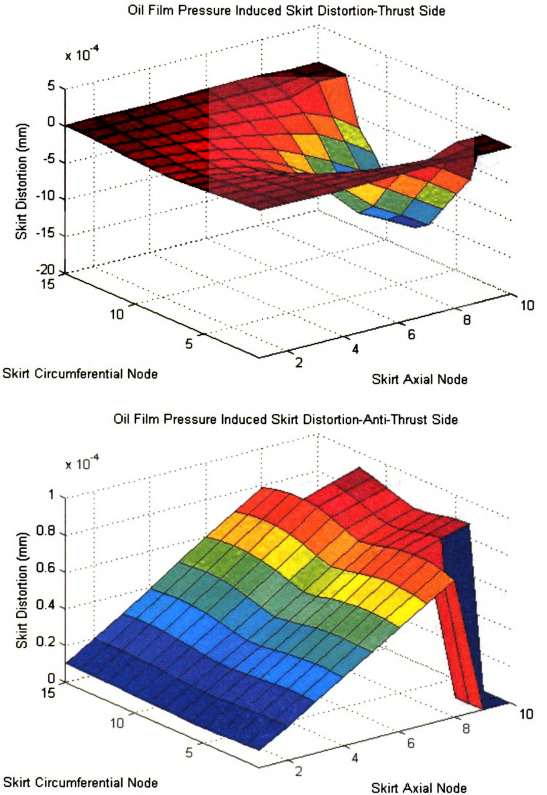

FIGURE 62. Piston skirt thrust and anti-thrust side distortion due to oil film pressure at 365 degree CA, 3000 RPM 2 PSI Boost

CHAPTER 6 COMPUTATIONAL VALIDATION - OPTICAL ENGINE SYSTEM

6.1 Introduction

The engine performance predictions using the computational models presented in previous chapters are compared with experimental measurements obtained from experiments conducted under the collaborative effort between the Engine Research Laboratory of Michigan State University and Mid Michigan Research, an Okemos engineering consulting company. The U.S.A. Army sponsors this effort [36]. Basic principles of the experiments are presented in this chapter.

This experimental rig is an optical system consisting of an engine equipped with an optically accessible full-length cylinder made of sapphire. The optical engine is positioned in a test rig equipped with laser optical devices so that high precision oil film thickness measurement using the laser-induced fluorescence technique (LIF) can be made during engine operation. For the piston temperature and the piston ring pack gas pressure measurements, telemetric technology is adopted. Here a piston is installed with wireless micropressure transducers and thermocouples for measuring the gas pressure and piston temperature at piston ring grooves and lands.

6.2 Laser-Induced Fluorescence Method

Laser-induced fluorescence (LIF) has been widely adopted in the measurement of piston assembly oil film thickness. The laser induced fluorescence is the wave emission from atoms or molecules because of their

excitation to higher energy levels due to the absorption of laser radiation. This method is selected because the fluorescence detection has the advantage of higher sensitivity and is non-intrusive. It is a spectroscopic method for sampling neutral or charged atomic or molecular species at their fundamental or excited states. When applied in the optical engine equipped with the full-length sapphire cylinder bore, the LIF method can be used to measure the oil film thickness directly at any crank angle and location; thus it provides a complete visual observation on the piston assembly oil film thickness.

6.3 Optical Engine System

Figure 63 shows the optical engine. The optical properties of the sapphire cylinder allow oil film measurement to be made at all possible directions along circumferential and axial directions (Fig. 64). It is mounted on a non-firing production engine structure, which is driven by a motor. Figure 65 shows the photo and the schematic of the optical system. The optical system consists of a CCD camera, an Excimer laser, laser optics and the optical engine. These are aligned precisely in a test rig such that the laser beam is directed to the sapphire cylinder for the measurement of the oil film thickness at desired locations. Table 3 gives a summary of the functions of components in the optical engine system.

TABLE 3. Optical system components and functions

Component	Function
Excimer Laser	Provides laser beam source at wavelength of about 308 nm
Laser optics	Guide and direct beam projection
CCD(charge-coupled device) Camera	Captures illuminated images of oil film thickness

Component	Function
Filter	Provides narrow bandwidth for light waves of about 505nm to pass through
OpticTable	Provides guided positions for optical components
Data Acquisition Device	Processes image data

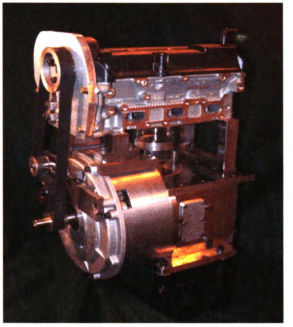

FIGURE 63. Optical engine equipped with sapphire cylinder

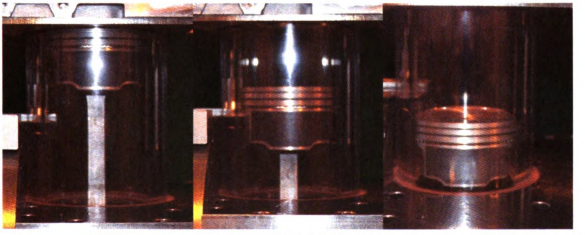

TDC **Mid Stroke** **BDC**

FIGURE 64. Sapphire cylinder provides optical access over entire range of piston stroke

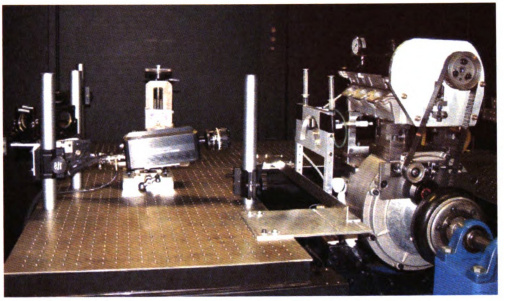

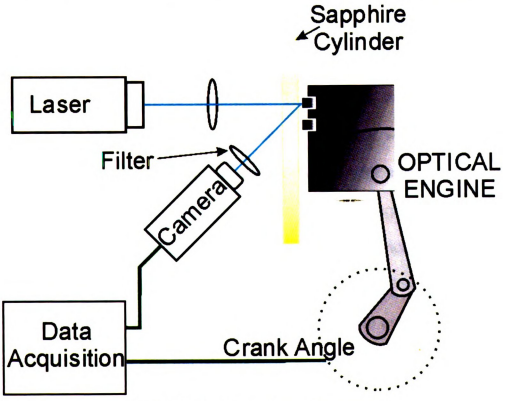

FIGURE 65. Optical engine system

6.4 Correlation between Oil Film Thickness and Film Illumination Intensity

Prior to oil film thickness measurement for an operating optical engine, the relationship between the thickness and the brightness of the illuminated oil film must be known. For this reason, a LIF calibration technique is developed. Making use of the sensitivity of LIF, the numerical relationship between fluorescence intensity and oil film thickness is determined. The calibration is conducted using the static calibration method on a calibration stand, shown in Figure 66(a). The accuracy of this method is accomplished by using a micrometer with a resolution of 1 micron as shown in Figure 66(b). The micrometer is used to hold a known thickness of oil against the sapphire window in the test stand, thus allowing fluorescence intensity to be measured at various oil film thicknesses. To measure the oil film thickness, the area between the micrometer head and the sapphire is first flooded with SAE 5W30 engine oil. The area is then illuminated with ultraviolet light (308 nm wavelength) from an Excimer laser, which results in the oil fluorescing at a wavelength of approximately 505 nm. A 505 nm narrow band filter is fitted onto a CCD camera in order to capture the images that only contain information from the fluorescing oil film with no interference from the original 308nm light wave reflection. An example of a LIF image of the calibrated oil film thickness is seen in Figure 66(c) where the bright, round area is the oil trapped between the micrometer and the sapphire.

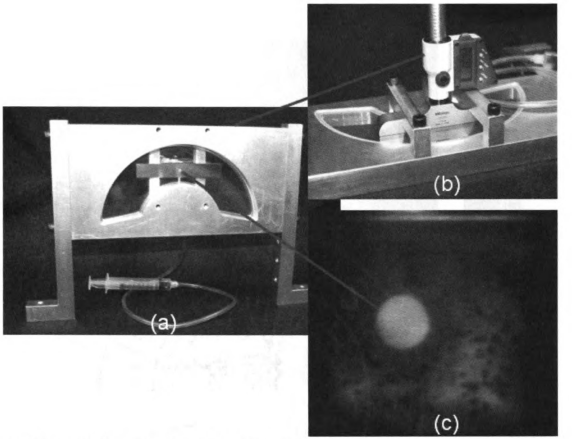

FIGURE 66. LIF calibration apparatus (a) calibration stand, (b) micrometer, and (c) LIF image of oil film thickness

With the known oil film thickness from the micrometer and the recorded fluorescence intensity, the correlation between these two data can be determined. To do so, the image captured needs to be transformed into digital form - pixel format, in order for the correlation to be completed. Figure 67 shows two examples of post-processed pixel intensity images for 32 microns and 106 microns respectively. As illustrated here, the LIF method is extremely capable in capturing the film thickness variation at the micron level. In an operating engine, the oil film thickness at the ring/bore interface is also at an order of microns. Thus, the LIF method has proven to be effective in the oil film thickness measurement for the optical engine.

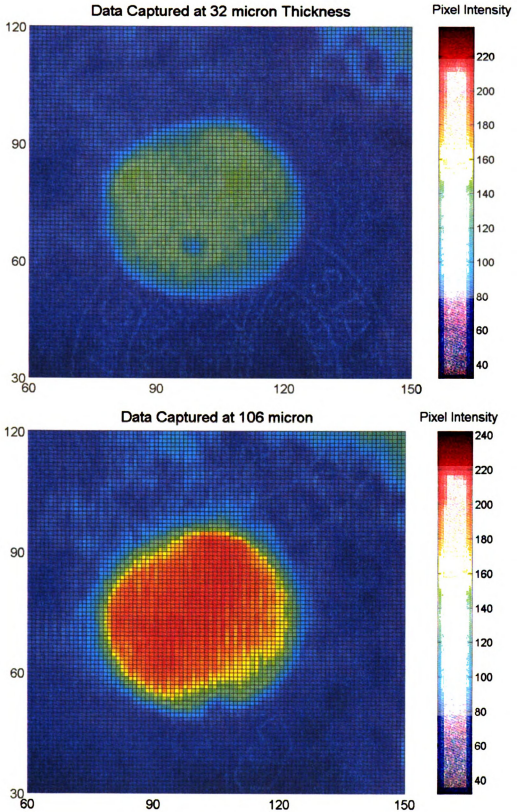

FIGURE 67. Processed digital LIF image

Images in this dissertation are presented in color.

Figure 68 shows a result of LIF calibration, where a measurement of oil film thickness on the calibration stand was taken at seven different oil film thicknesses regulated using the micrometer. The oil film thickness is observed to have an exponential relationship with its image pixel intensity. However, under normal operating conditions, the ring/bore oil film thickness usually does not go beyond 50 micron. Hence, the linear approximation from the correlation curve can be used as the reference for oil film thickness measurement of the optical engine.

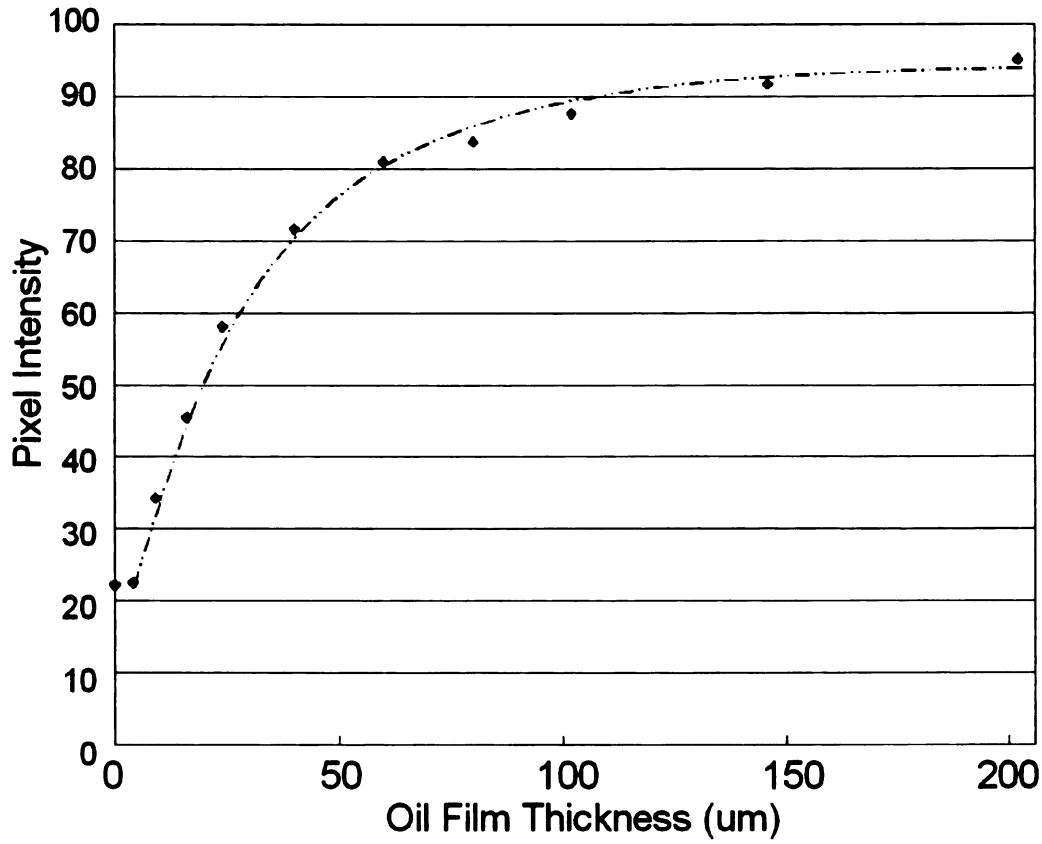

FIGURE 68. LIF calibration curve

6.5 Procedure for Oil Film Thickness Measurement

The oil film thickness measurement for the optical engine under running conditions is performed using the following two-step procedure. First, the engine is rolled away and the calibration stand is stationed in its place. The LIF calibration is carried out in the way described in previous section. After the calibration is completed, the engine is rolled back to the exact same location, where the stand was, for oil film thickness measurement. High precision translation of optical engine position is achieved using a test stand which is equipped with devices for small horizontal displacement. Figure 69 shows the optical engine that is installed on a test stand in a test cell.

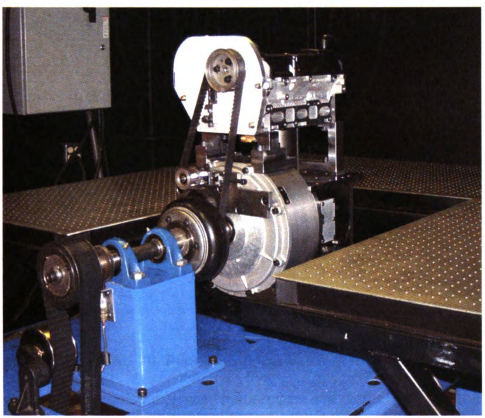

FIGURE 69. Optical engine in test cell

6.6 Piston Ring Pack Pressure and Temperature Measurement

The piston of the optical engine is equipped with state-of-the-art technology, IR telemetrics, to measure gas pressures at each of its grooves and lands, and its body temperature, as shown in Figure 70.

FIGURE 70. Piston equipped with IR telemetrics

Six pressure transducers are mounted on the piston with one transducer each at the second and third lands, top ring groove and oil ring groove, and with

two transducers at the second ring groove with one at the thrust side and another at the antithrust. Five thermocouples are mounted on the piston with one thermocouple each at the second and third lands, and all the three piston ring grooves. The measuring devices are wireless; magnetic induced electricity is generated from the interaction between the coil on the piston and a stationary base on the engine body. Digital signals are acquired from the transducers and thermocouples during engine run time.

6.7 Engine Test Runs

Engine tests are conducted to measure the performance of the motored optical engine over a range of operating conditions. Even though the optical engine does not operate with fuel combustion, the cylinder gas pressure is regulated or boosted at the intake throttle to imitate the firing engine gas pressure trend.

6.7.1 Inter-Ring Gas Pressure Results

During the inter-ring gas pressure measurement, the sapphire cylinder bore is replaced with a cast-iron cylinder bore so that the measurement can be taken over a greater range of operating conditions. Cast-iron is used because it can withstand higher impact from the piston dynamics during high speed, and the influence of the material of the cylinder bore on the gas dynamic is almost negligible. Selected operating conditions for the inter-ring gas pressure measurement are given in Table 4.

TABLE 4. Operating conditions for inter-ring gas pressure measurement

Speed	Intake Pressure Condition
1000 RPM	2 PSI Boost, 4 PSI Boost, 6 PSI Boost, 8 PSI Boost
1500 RPM	2 PSI Boost, 4 PSI Boost, 6 PSI Boost, 8 PSI Boost, 15 mm Hg Manifold Vacuum
2000 RPM	2 PSI Boost, 4 PSI Boost, 6 PSI Boost, 8 PSI Boost, 15 mm Hg Manifold Vacuum
2500 RPM	2 PSI Boost, 4 PSI Boost, 6 PSI Boost, 8 PSI Boost, 15 mm Hg Manifold Vacuum
3000 RPM	2 PSI Boost, 4 PSI Boost, 6 PSI Boost, 8 PSI Boost, 15 mm Hg Manifold Vacuum

Figures 72 to 95 show the measured inter-ring pressures in comparison to the CASE simulated results. Gas pressures at the top ring groove, the piston second land, the second ring groove, and the third piston land, as illustrated by Figure 71, are compared between the prediction and measurement.

The overall result comparison shows that the prediction of the ring pack pressures from the computational models is in relatively good agreement with the measurement except at the third piston land pressures and the third ring groove pressures (not presented).

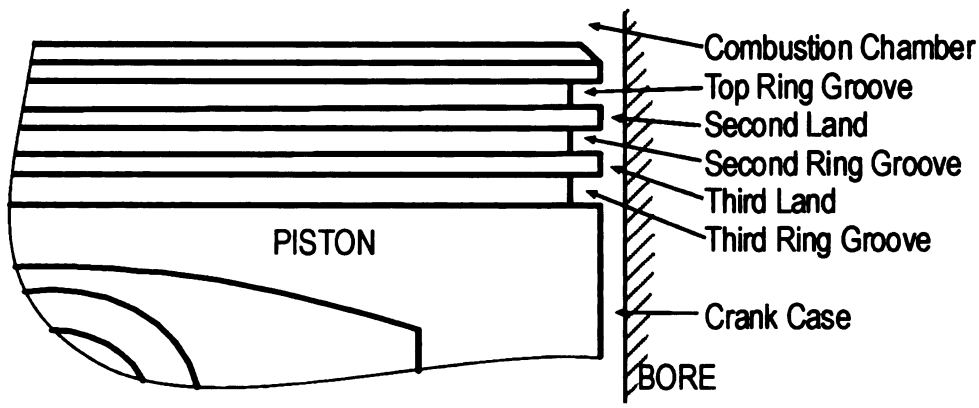

FIGURE 71. Detailed piston ring pack region

The comparison of the top ring groove pressures for all operating conditions, except 1000 RPM 8 PSI Boost, shows that the error is within about 5%. Good correlation is observed in both quantitative and qualitative comparisons. This observation should be expected due to the direct application of the measured cylinder gas pressure as a boundary condition for the gas flow calculation at regions surrounding the top piston ring - first groove and second land. For the second land pressures, 15 of the 24 cases show that the comparison is within about 5% error and good correlation is also observed in both quantitative and qualitative comparisons for these cases. The lesser agreement at the second land pressures compared to the top ring groove pressures are due to the fact that the calculation is now not relying on the measured cylinder gas pressures, but rather on the calculated top groove pressure and the calculated second land pressures as boundary conditions. For the second ring groove pressures, 11 of the 24 cases show good correlation in both quantitative and qualitative comparisons. However, for the third land pressures, only 3 of the 24 cases show good correlation.

The discrepancy can be attributed to some degree of shortcoming in both the experiment and the computational model. The telemetric technology used in the experiment has a major problem of noise disturbance on the measured pressures and temperatures. Filtering technique is currently being used to filter out the high frequency data, which are assumed to be from the external noise. However, the filtering process has a very high potential to eliminate useful information at the same time. For instance, the pressure spikes due to the ring

fluttering are predicted at some cases, but the measurement does not display the spikes even though a similar trend of pressure traces between the prediction and measurement is observed during the occurrence of the spikes (refer to Figures 85,86,87,92,93,94).

On the other hand, the model of the inter-ring pack pressures in CASE is based on the orifice-volume method, which solves for the flow pressures across all piston grooves and lands simultaneously using the iterative method. The calculated pressure of a control volume is very dependent on the pressures at the upper and lower boundaries. While the pressure at the top boundary (top ring) is the measured cylinder gas pressure, the pressure at the bottom boundary (oil control) is the crank case pressure, which is assumed to be at constant atmospheric pressure (measurement is not available). The constant pressure assumption is not so appropriate in this application as the measure pressure at the oil control ring region does show a sinusoidal pressure trace pattern as a function of crank angle. The current gas dynamics model needs to be improved in order to account for the cyclic variation of crank case pressure. As a result, good correlation is observed at the region closer to the combustion chamber, but the discrepancy is seen to increase across the piston ring pack region towards the engine crank case.

Several useful observations regarding piston ring dynamics are given here. Spikes on the pressure traces are observed at some cases, implying the ring fluttering phenomenon, or instability of the ring dynamics within the ring groove. It

is known that there is a mutual dependent relationship between the piston ring dynamics and the inter-ring gas flow dynamics. The piston ring relative positions in ring grooves affect the pressure variation across the piston ring pack as the axial and radial movement of piston rings within piston grooves creates variable paths for the cylinder gas to flow from one piston land or piston groove to another. On the other hand, pressure variation also has countereffect on piston ring dynamics. The pressure gradient between the top and the bottom of a piston ring, coupled with its inertia, will dictate its position equilibrium within the groove. The fluttering observed in some cases is believed to be from the second and third ring since no pressure fluctuation is observed on the top ring groove. The instability of the piston ring dynamics is observed to increase as the engine speed increases. This implies that the gas pressures on the top and the bottom of a ring and its inertia have mutually comparable effects on the ring dynamics during high speed conditions. In contrast, for the top ring, the pressure on the top of the ring (cylinder gas pressure) is much higher than on the bottom of the ring, resulting in much stable and predictable piston ring axial motion. A more severe degree of pressure fluctuation is observed at the third piston land, which implies that the oil control ring probably experiences the least stability condition.

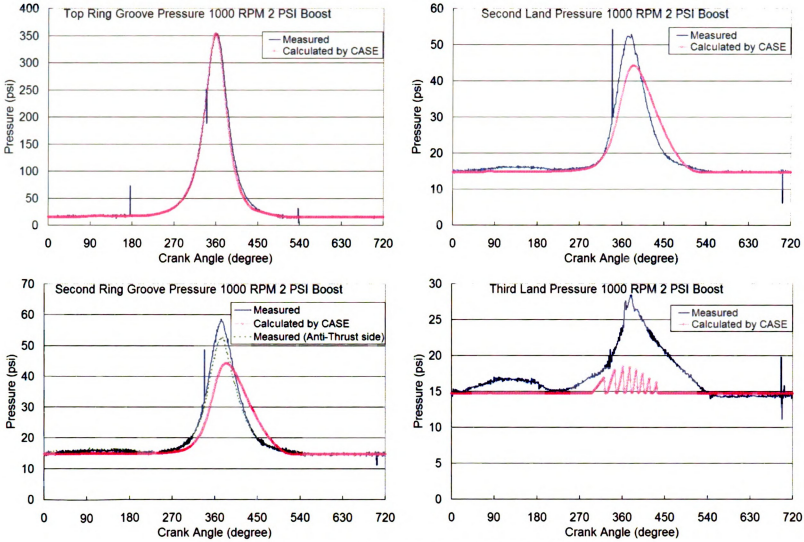

FIGURE 72. Inter-ring gas pressure at 1000 RPM 2 PSI Boost

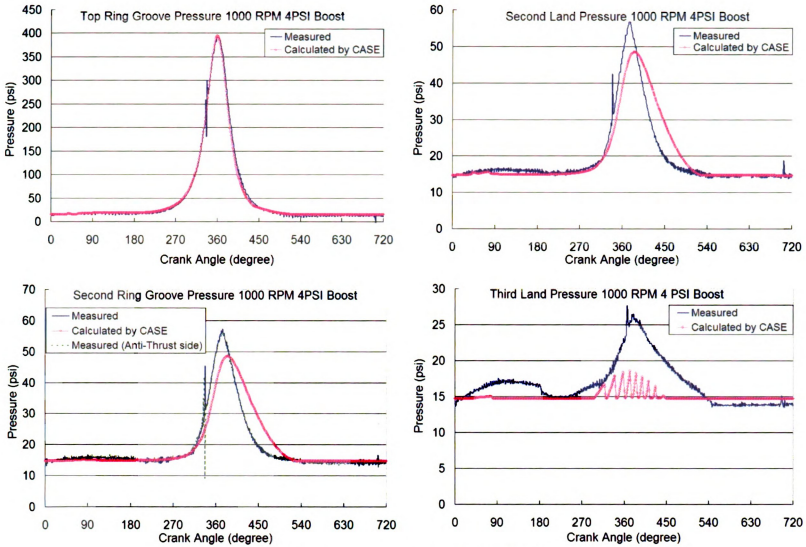

FIGURE 73. Inter-ring gas pressure at 1000 RPM 4 PSI Boost

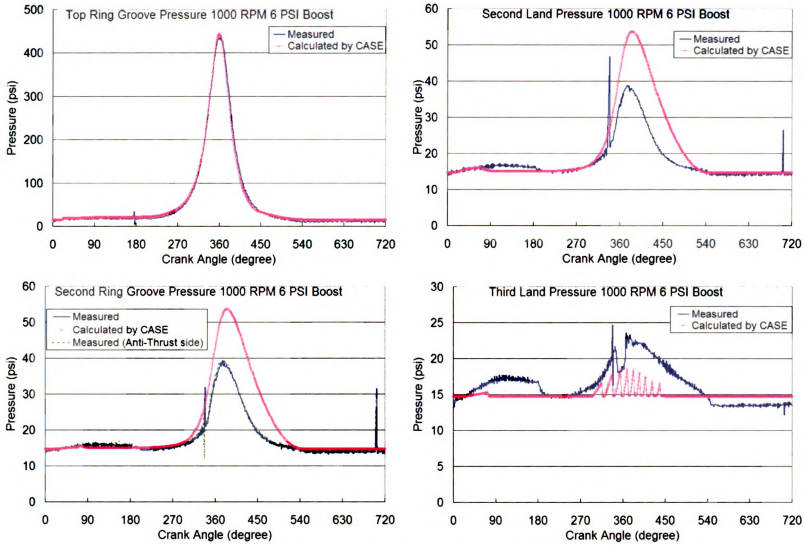

FIGURE 74. Inter-ring gas pressure at 1000 RPM 6 PSI Boost

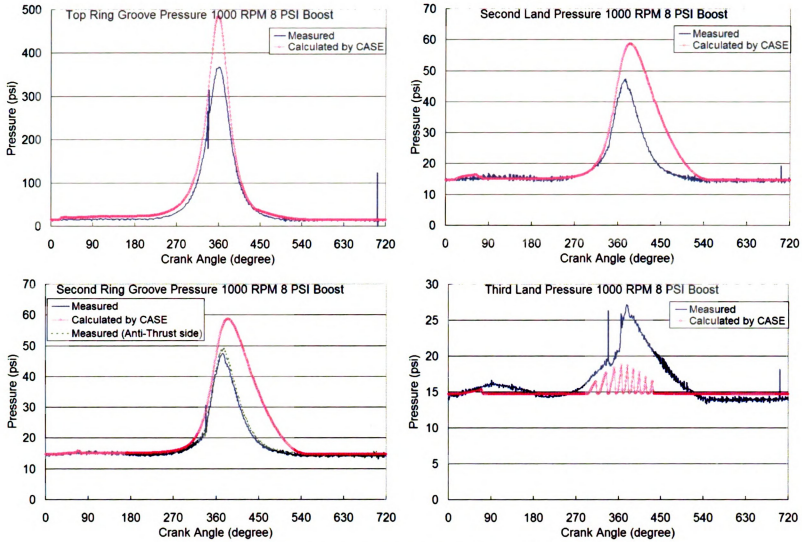

FIGURE 75. Inter-ring gas pressure at 1000 RPM 8 PSI Boost

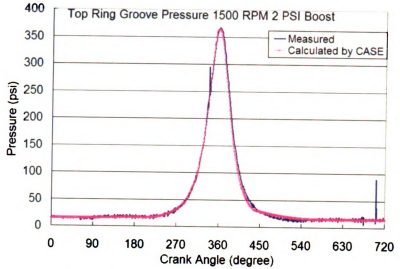

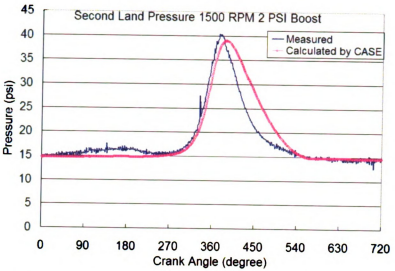

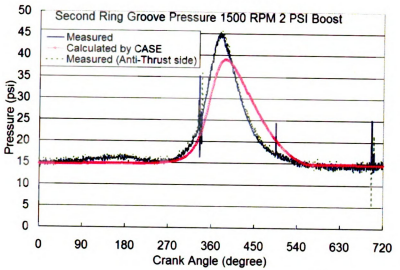

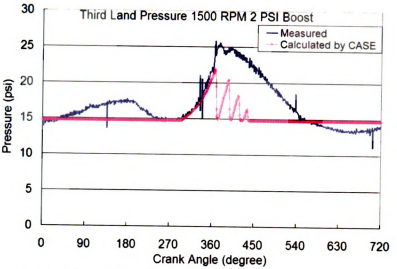

FIGURE 76. Inter-ring gas pressure at 1500 RPM 2 PSI Boost

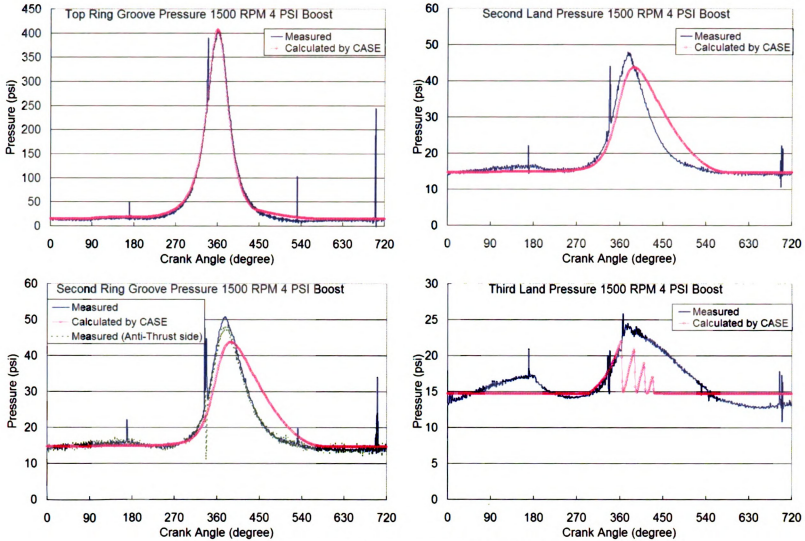

FIGURE 77. Inter-ring gas pressure at 1500 RPM 4 PSI Boost

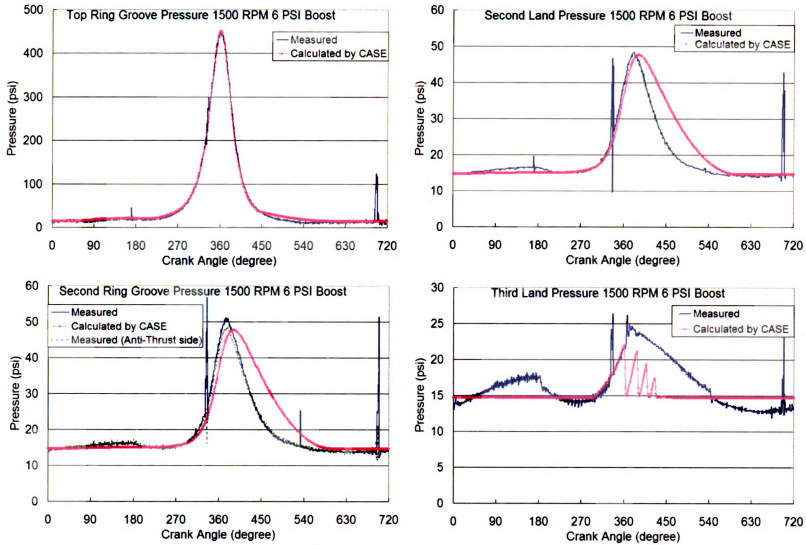

FIGURE 78. Inter-ring gas pressure at 1500 RPM 6 PSI Boost

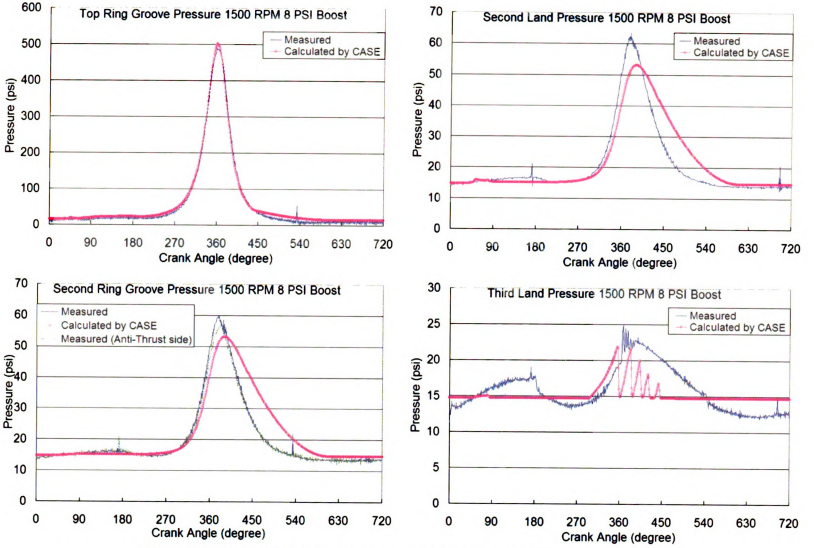

FIGURE 79. Inter-ring gas pressure at 1500 RPM 8 PSI Boost

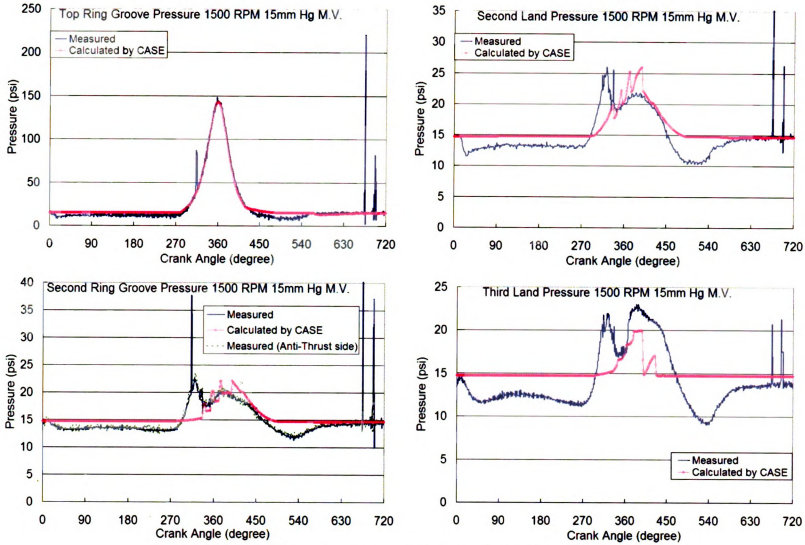

FIGURE 80. Inter-ring gas pressure at 1500 RPM 15 mm Hg M.V.

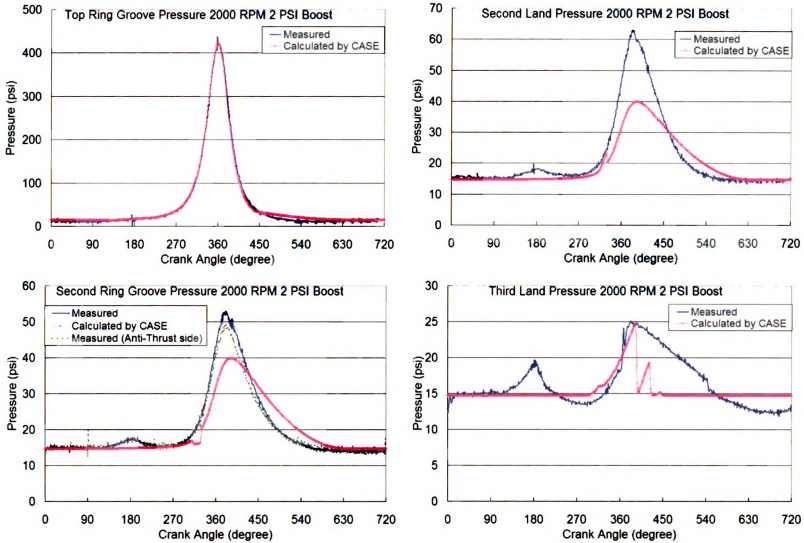

FIGURE 81. Inter-ring gas pressure at 2000 RPM 2 PSI Boost

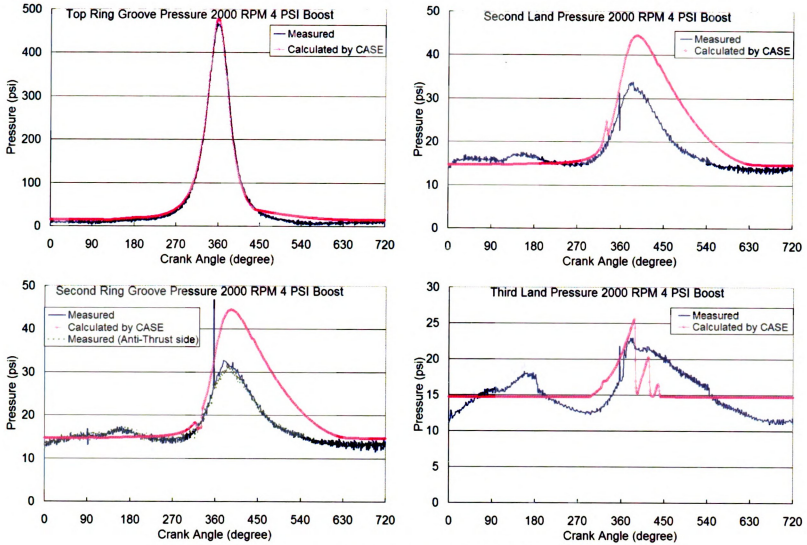

FIGURE 82. Inter-ring gas pressure at 2000 RPM 4 PSI Boost

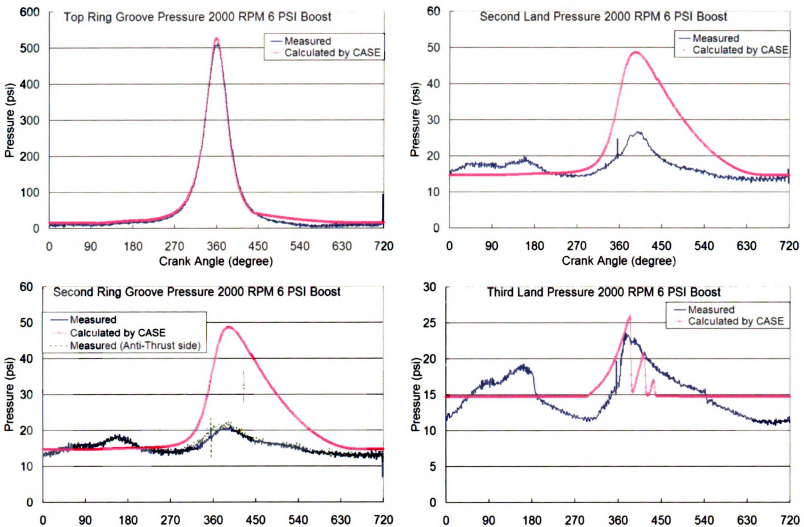

FIGURE 83. Inter-ring gas pressure at 2000 RPM 6 PSI Boost

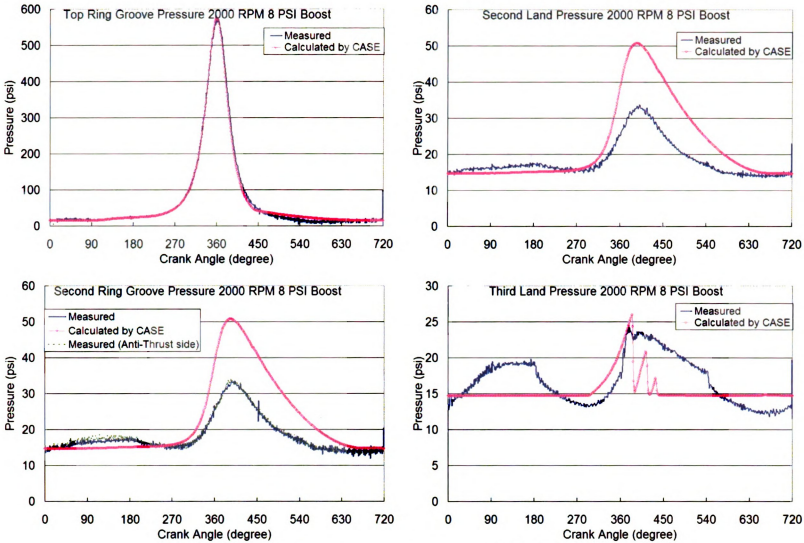

FIGURE 84. Inter-ring gas pressure at 2000 RPM 8 PSI Boost

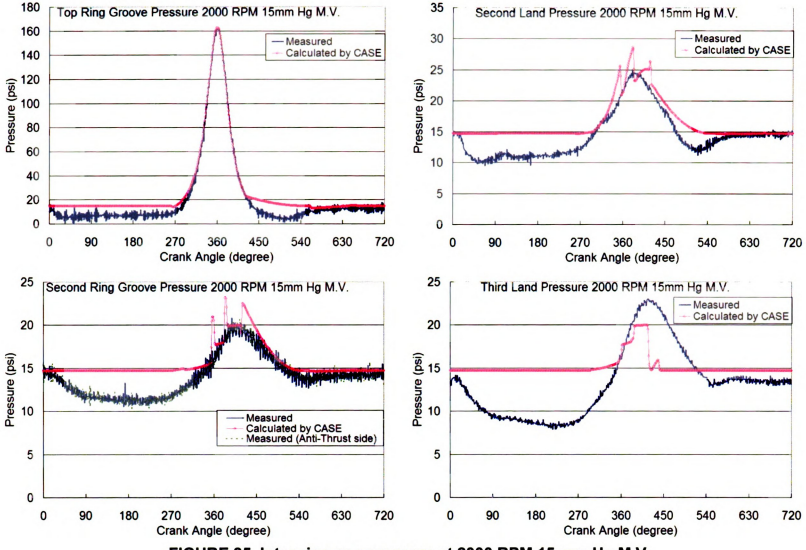

FIGURE 85. Inter-ring gas pressure at 2000 RPM 15 mm Hg M.V.

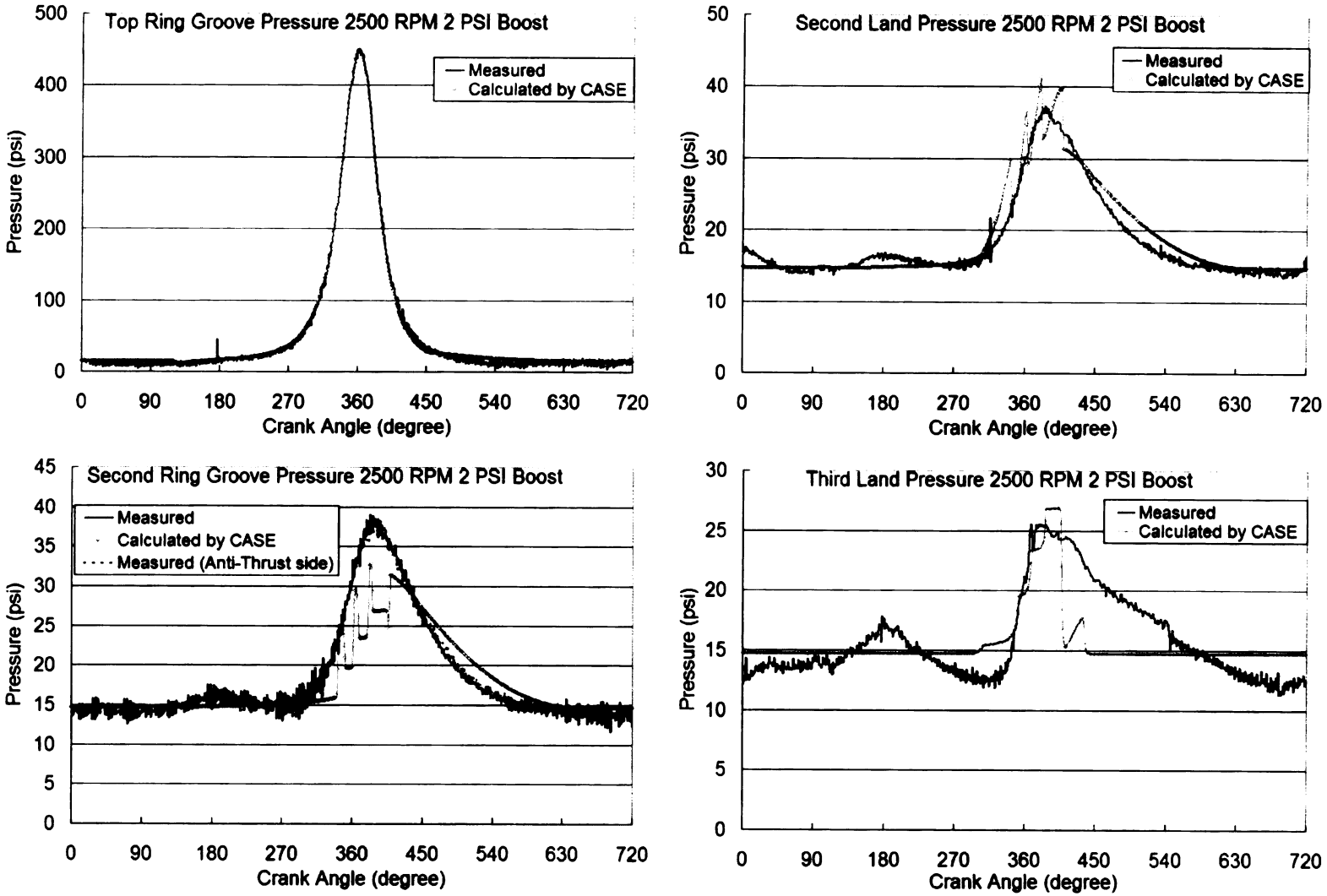

FIGURE 86. Inter-ring gas pressure at 2500 RPM 2 PSI Boost

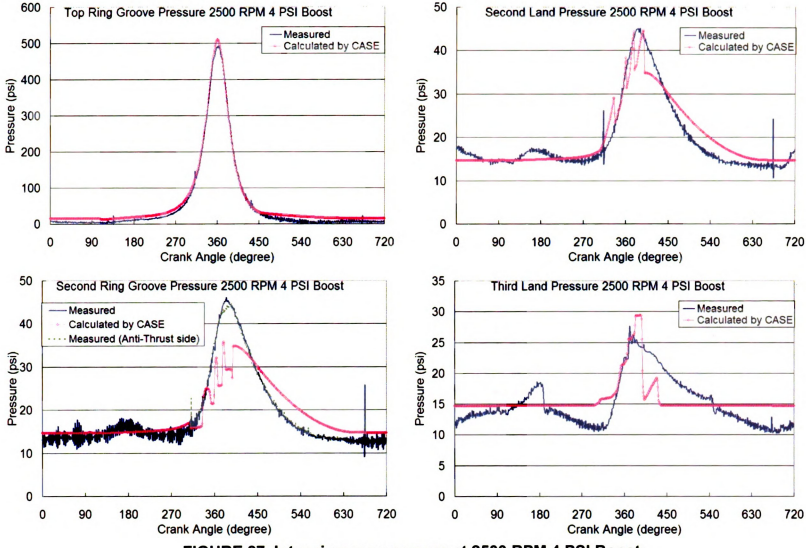

FIGURE 87. Inter-ring gas pressure at 2500 RPM 4 PSI Boost

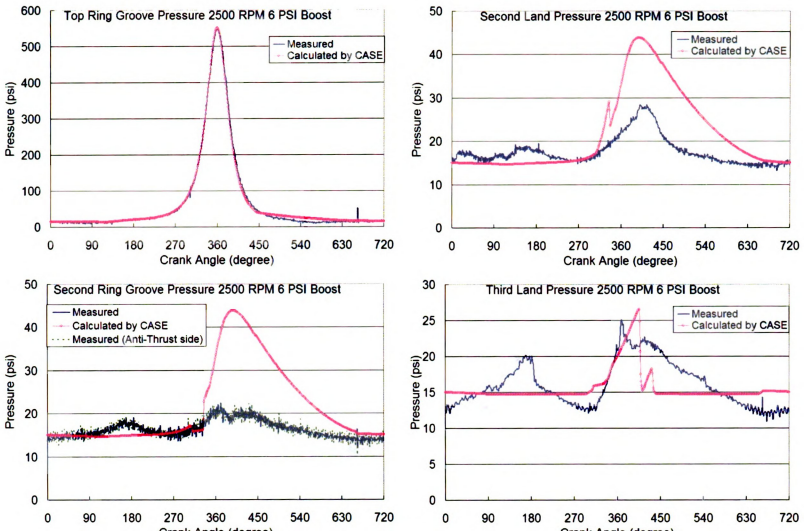

FIGURE 88. Inter-ring gas pressure at 2500 RPM 6 PSI Boost

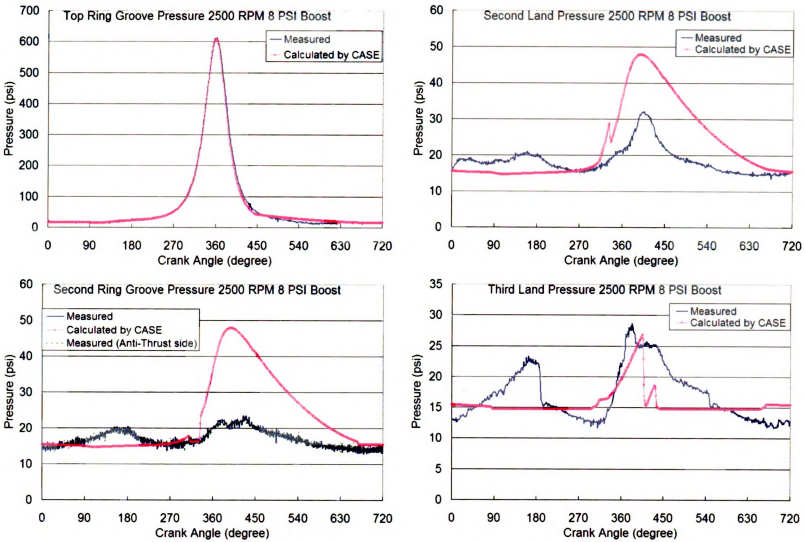

FIGURE 89. Inter-ring gas pressure at 2500 RPM 8 PSI Boost

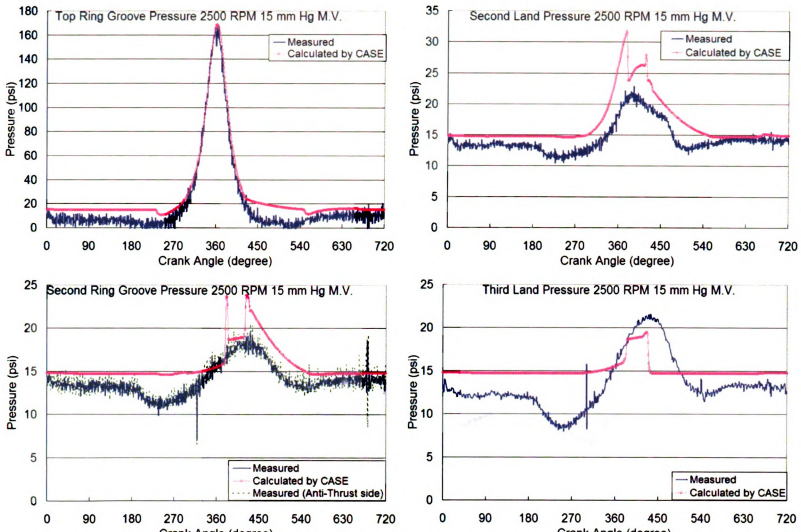

FIGURE 90. Inter-ring gas pressure at 2500 RPM 15 mm Hg M.V.

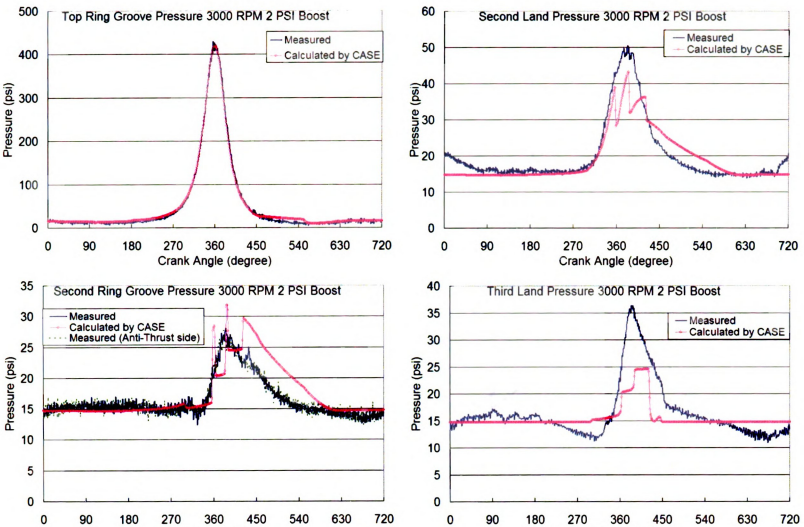

FIGURE 91. Inter-ring gas pressure at 3000 RPM 2 PSI Boost

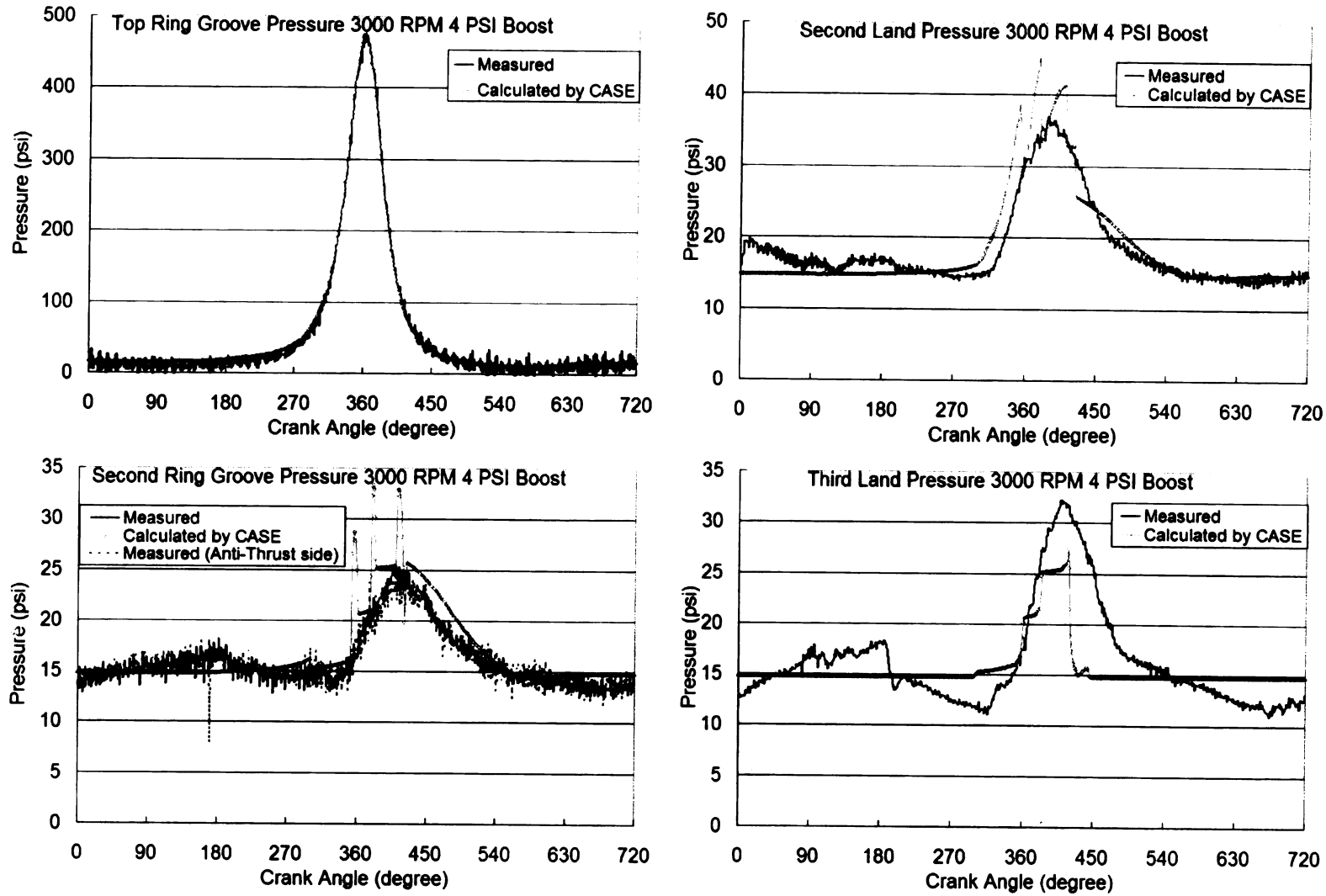

FIGURE 92. Inter-ring gas pressure at 3000 RPM 4 PSI Boost

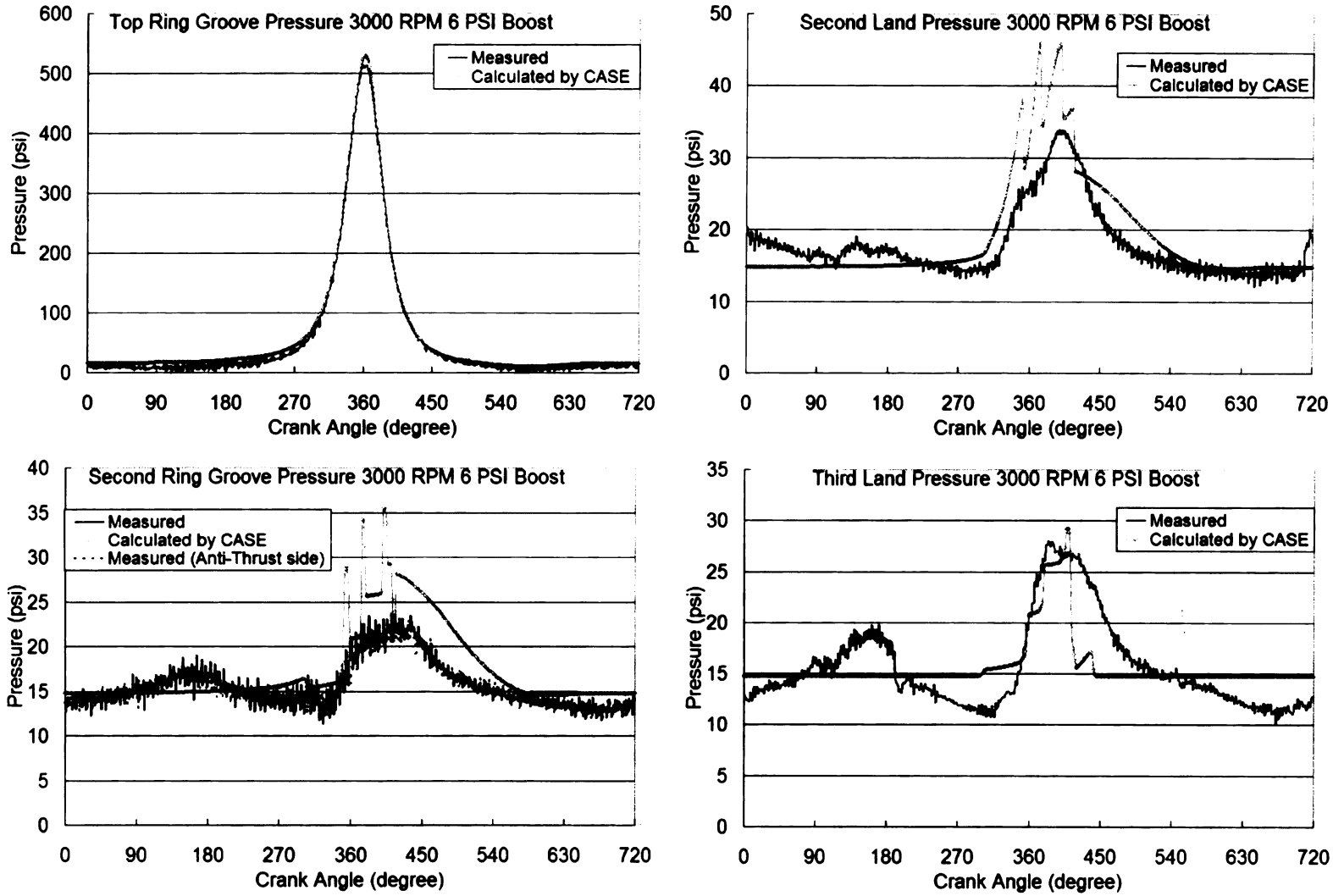

FIGURE 93. Inter-ring gas pressure at 3000 RPM 6 PSI Boost

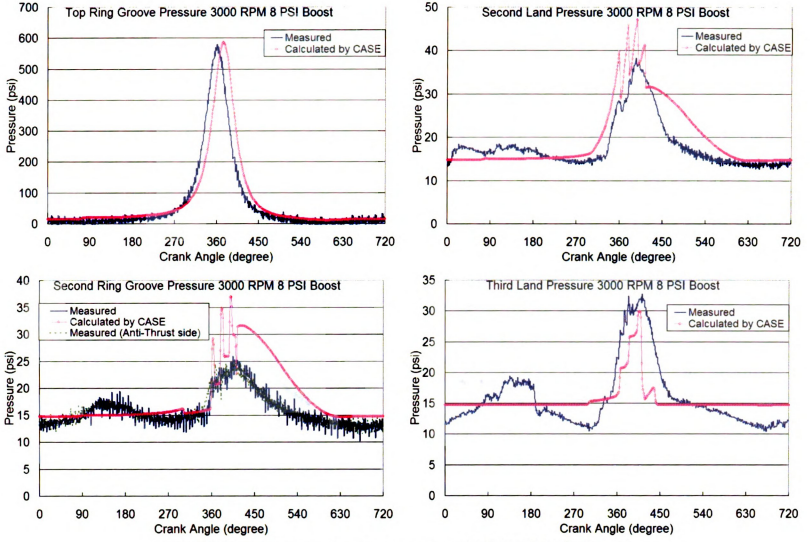

FIGURE 94. Inter-ring gas pressure at 3000 RPM 8 PSI Boost

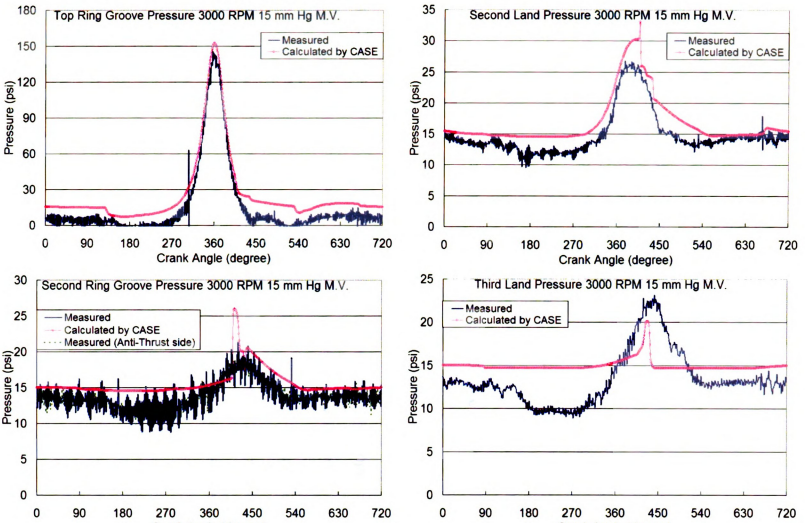

FIGURE 95. Inter-ring gas pressure at 3000 RPM 15 mm Hg M.V.

6.7.2 Oil Film Thickness Measurement Results

During the oil film thickness measurement using the LIF method, the sapphire cylinder bore is used. Currently, the highest engine speed is only limited to 1500 RPM because of the concern over the ductility of the sapphire in response to thermal load induced from the piston ring/bore interaction. An infrared camera is being used to monitor the temperature distribution of the sapphire cylinder to ensure that it is not overheated during engine operation. Figures 96 and 97 show the oil film thickness measured at the top compression ring and the second compression ring respectively over three engine speeds - 500, 750 and 1000 RPM. The measurement is taken at 320 degree crank angle (CA) (40 degree CA before top dead center, compression stroke). The measurements are consistent with the general observation that higher speed leads to thicker hydrodynamic oil film. The ring profile is used for reference. Comparison with the prediction is made at 500 RPM 40 degree CA and 1000 RPM 320 degree CA for the top compression ring oil film thickness, as shown in Figures 98 and 99. Without taking into consideration the roughness edge of the ring face on the predicted result, the difference of the mean oil film thickness between the prediction and the measurement are 32.3% and 28.5% for the 500 RPM 40 degree CA and 1000 RPM 320 degree CA respectively. Considering the degree of complication involved in the calculation as well as the measurement of oil film thickness, the error is considered relatively small.

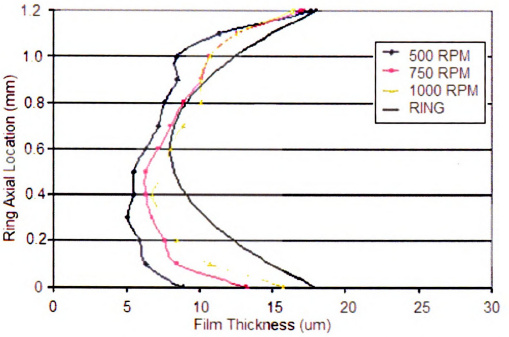

FIGURE 96. Top ring oil film thickness profiles measured over various engine speeds at 320 degree CA

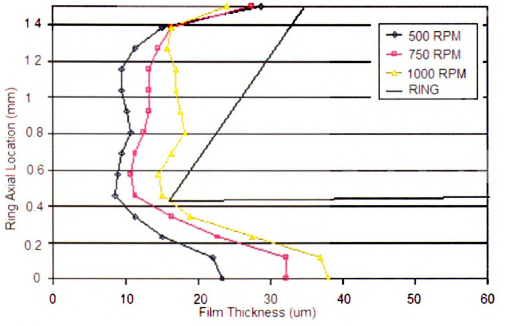

FIGURE 97. Second ring oil film thickness profiles measured over various engine speeds at 320 degree CA

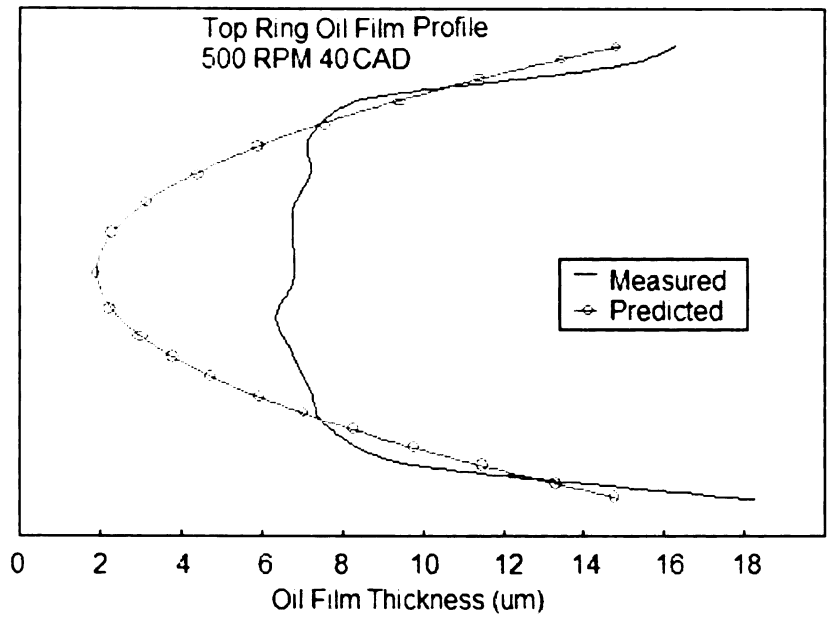

FIGURE 98. Oil film thickness profile at 500 RPM, 40 degree CA

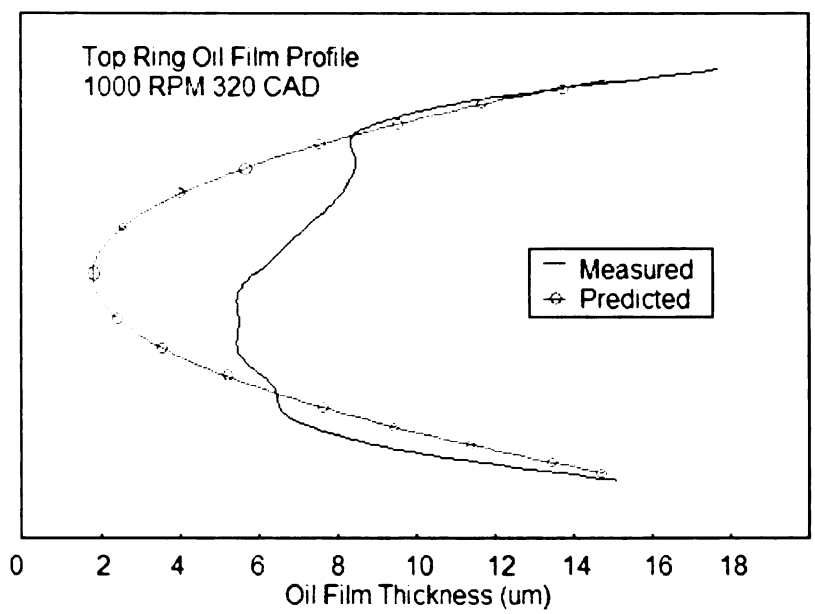

FIGURE 99. Oil film thickness profile at 1000 RPM, 320 degree CA

A systematic series of test runs is conducted for cyclic oil film thickness measurement. The selected operating conditions for the oil film thickness measurement are given in Table 5.

TABLE 5. Operating conditions for oil film thickness measurement

Speed	Intake Pressure Condition
500 RPM	2 PSI Boost, 8 PSI Boost, 15 mm Hg M.V.
1500 RPM	2 PSI Boost, 8 PSI Boost, 15 mm Hg M.V.

The measured oil film thickness results are presented in Figures 101 - 115. The oil film thickness is measured over the region that covers the top and second rings at 500 RPM and 1500 RPM under three intake pressure conditions (15 mm Hg M.V. (or equivalent of 7 PSI Vacuum), 2 PSI Boost and 8 PSI Boost).

The detailed lubrication profile obtained from measurement does shed some light regarding the partially flooded assumption made for the piston ring pack lubrication modeling. The measured profiles given in Figures 101 - 115 show that the oil transport at one ring is not relying solely on another ring. There is oil trapped between two rings that contributes to the inter-ring oil flow. At 270 and 630 degree CA, when the piston ring pack is moving upwards, the oil film left from the top ring is going to be a source of supplied oil for the trailing second ring. At 90 and 450 degree CA, the top ring becomes the trailing ring. A commonly used assumption in the theoretical modeling of partially flooded analysis is that the oil left from the leading ring is solely the supplied oil for the trailing ring, and the trapped oil between them is ignored, in order to established a inter-ring oil transport model. This assumption is not appropriate at least in the application of

this motored and boosted optical engine system, as shown from the measurement where the trailing ring is observed to have thick oil film cumulation in its front edge for all the cases. Therefore, the assumption used in the partially flooded model of this dissertation, which considers fully flooded conditions for the rings below the top ring, is shown to be valid in this application.

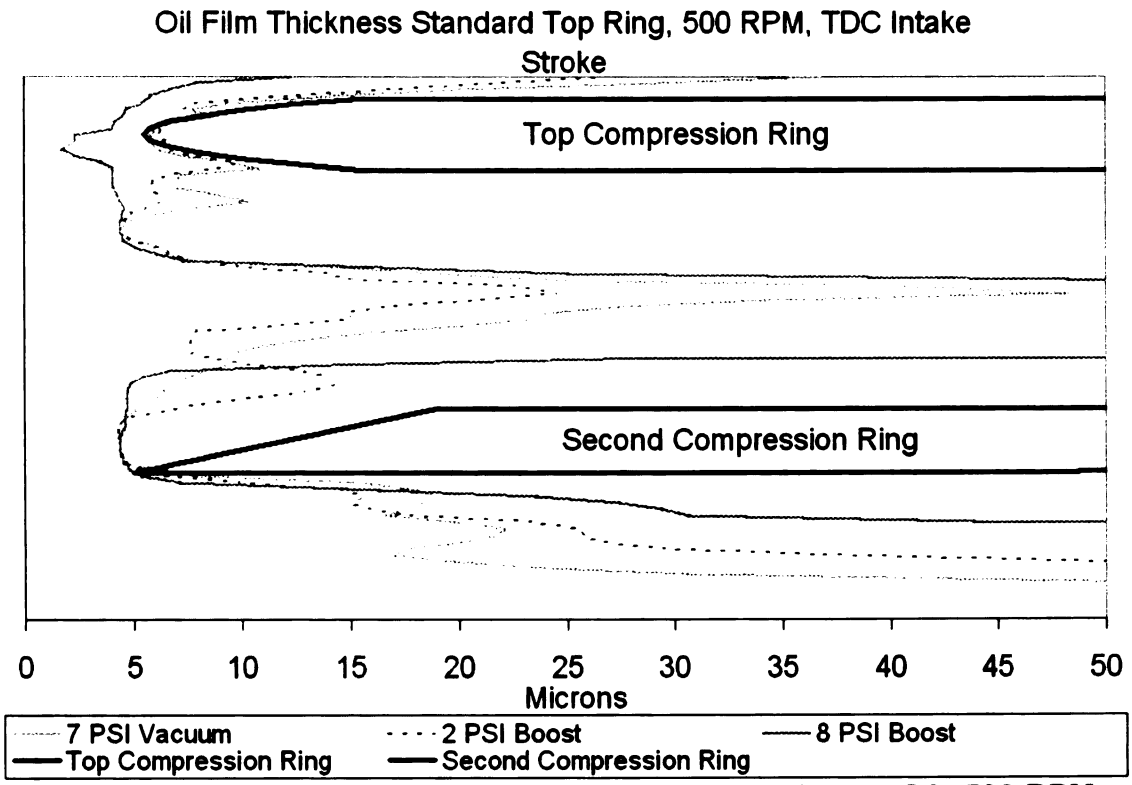

FIGURE 100. Oil film thickness measured at 0 degree CA, 500 RPM

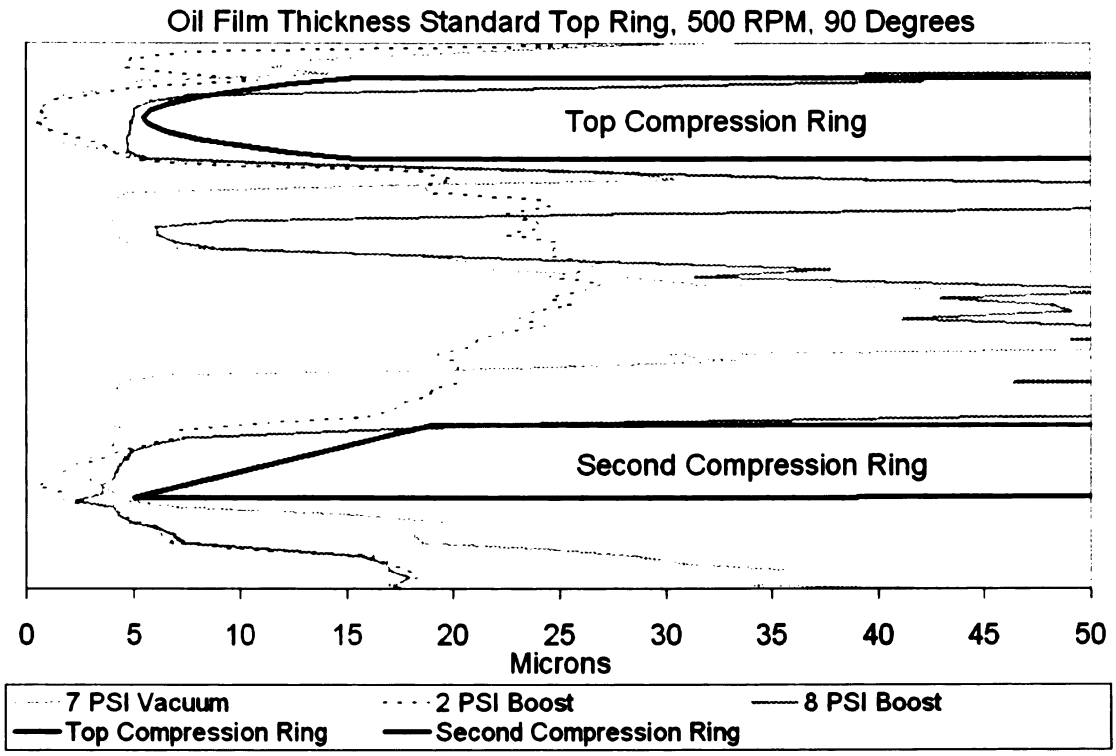

FIGURE 101. Oil film thickness measured at 90 degree CA, 500 RPM

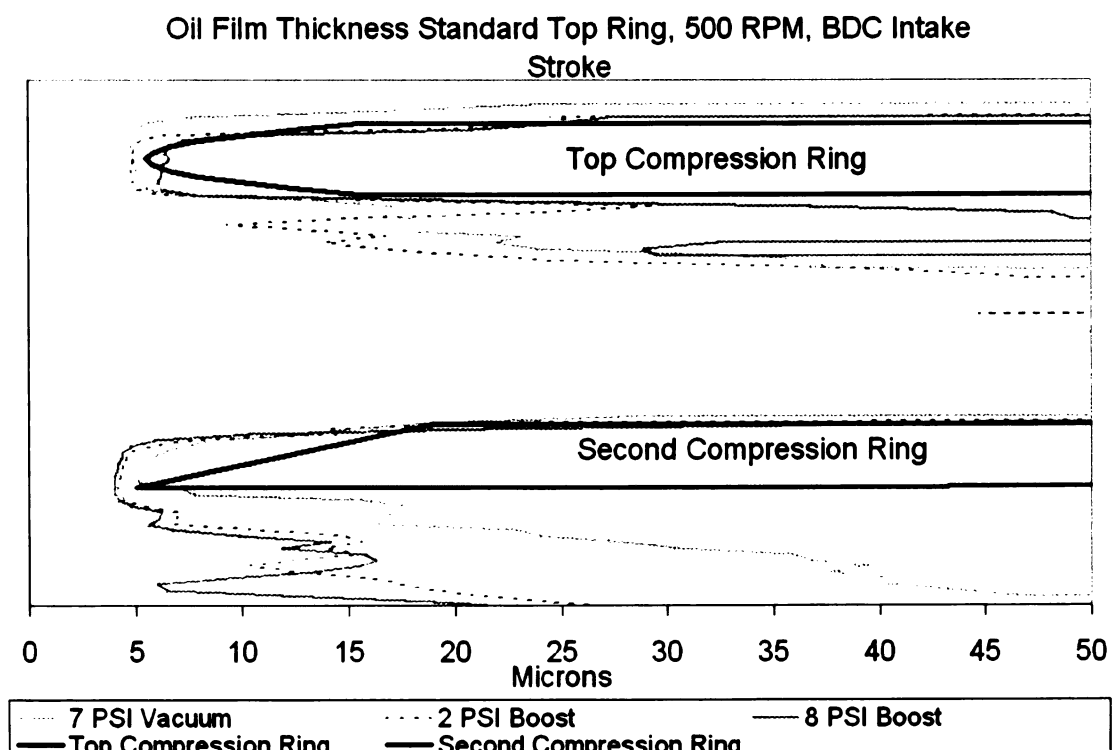

FIGURE 102. Oil film thickness measured at 180 degree CA, 500 RPM

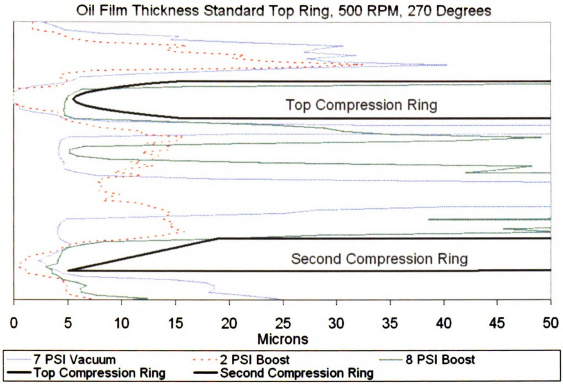

FIGURE 103. Oil film thickness measured at 270 degree CA, 500 RPM

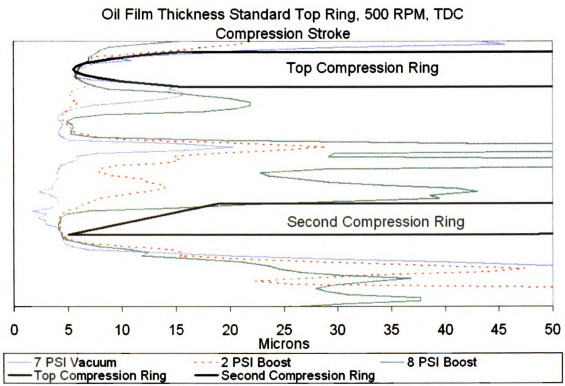

FIGURE 104. Oil film thickness measured at 360 degree CA, 500 RPM

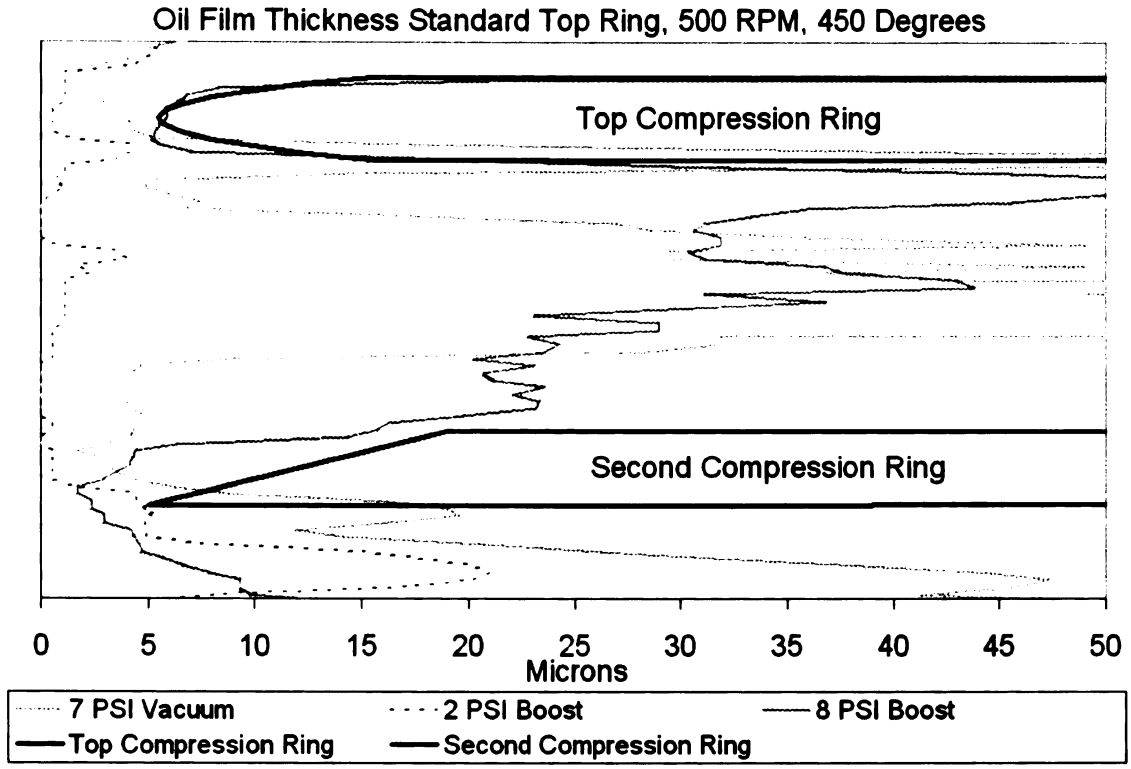

FIGURE 105. Oil film thickness measured at 450 degree CA, 500 RPM

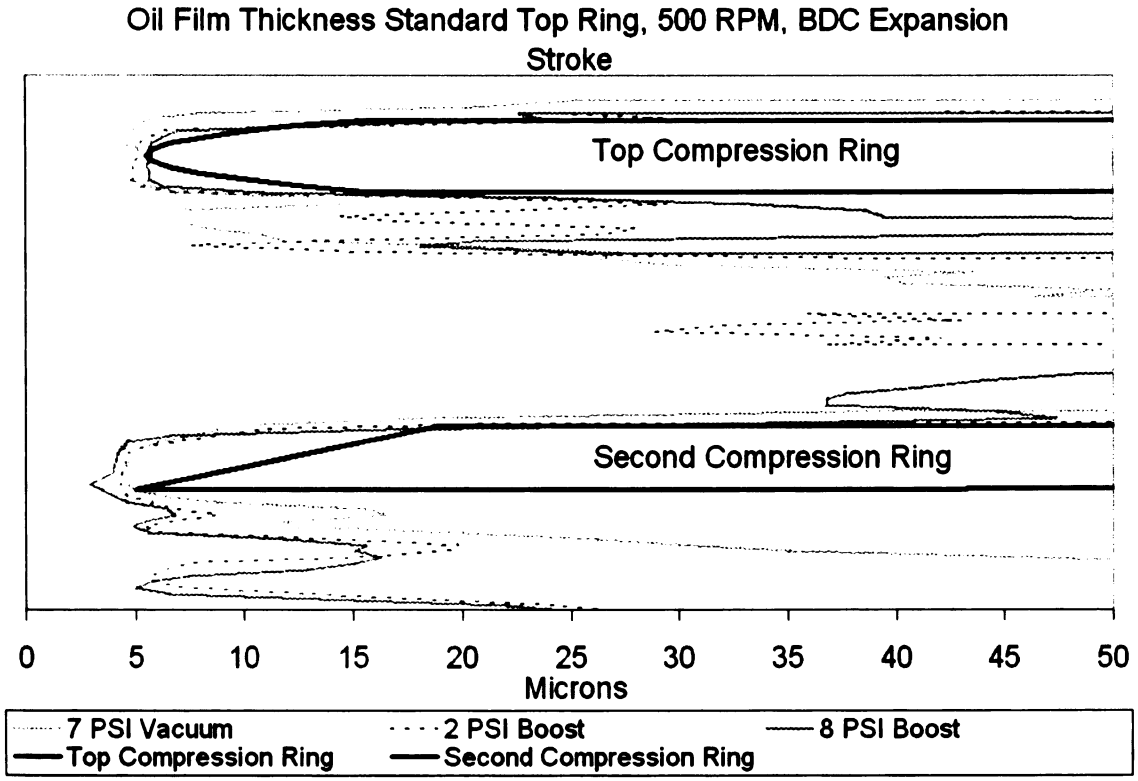

FIGURE 106. Oil film thickness measured at 540 degree CA, 500 RPM

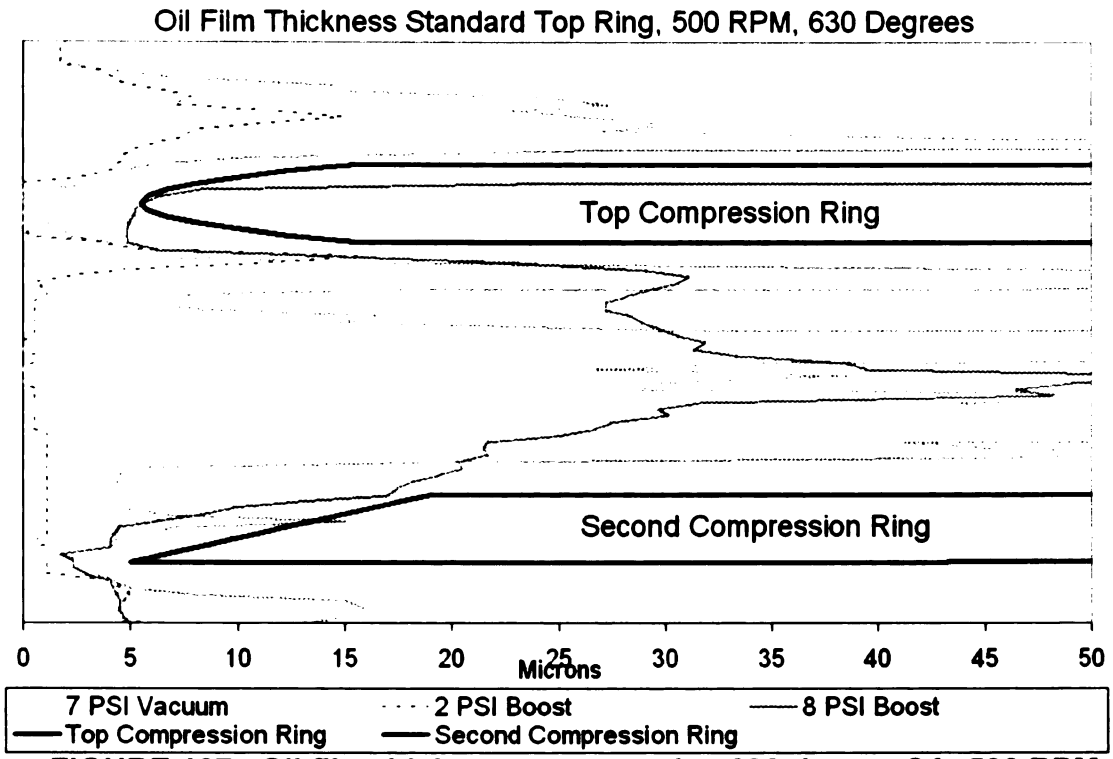

FIGURE 107. Oil film thickness measured at 630 degree CA, 500 RPM

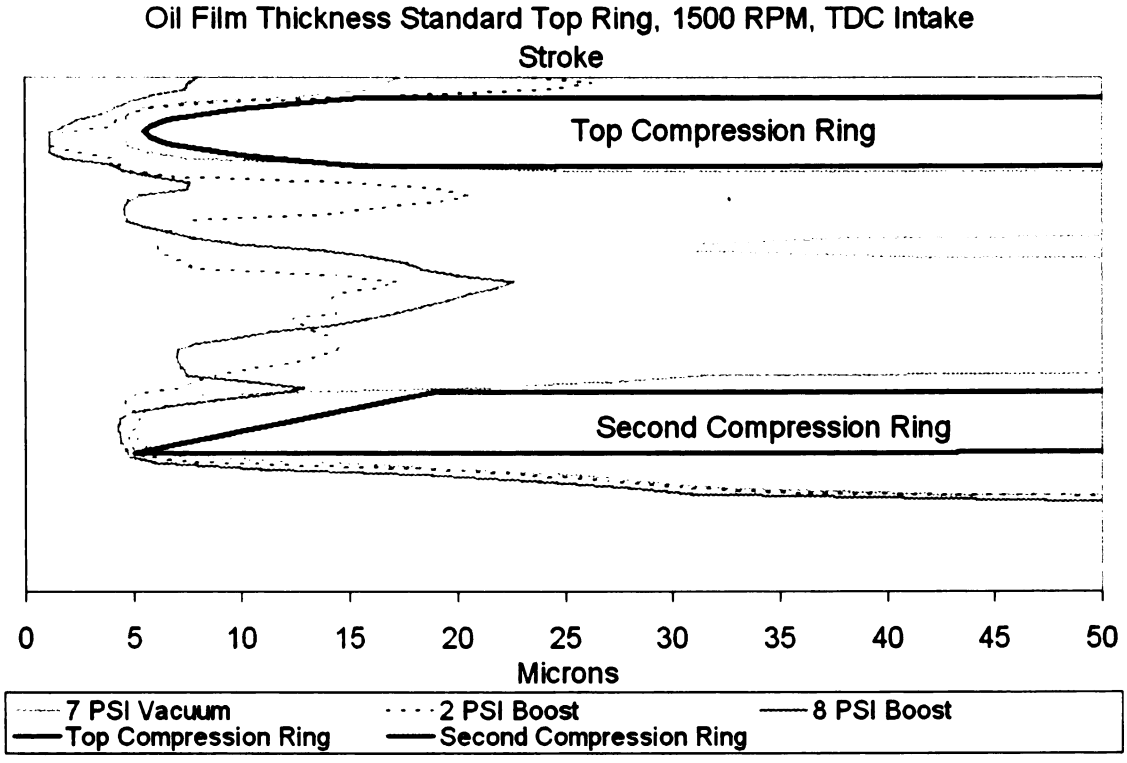

FIGURE 108. Oil film thickness measured at 0 degree CA, 1500 RPM

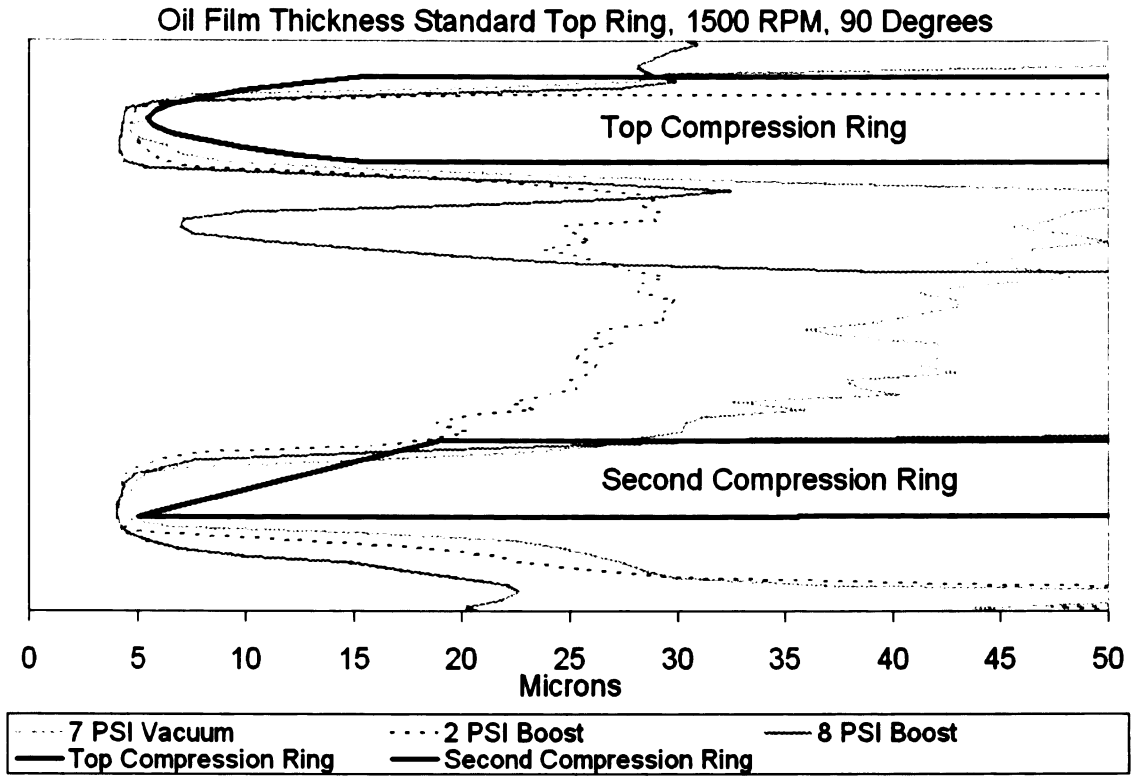

FIGURE 109. Oil film thickness measured at 90 degree CA, 1500 RPM

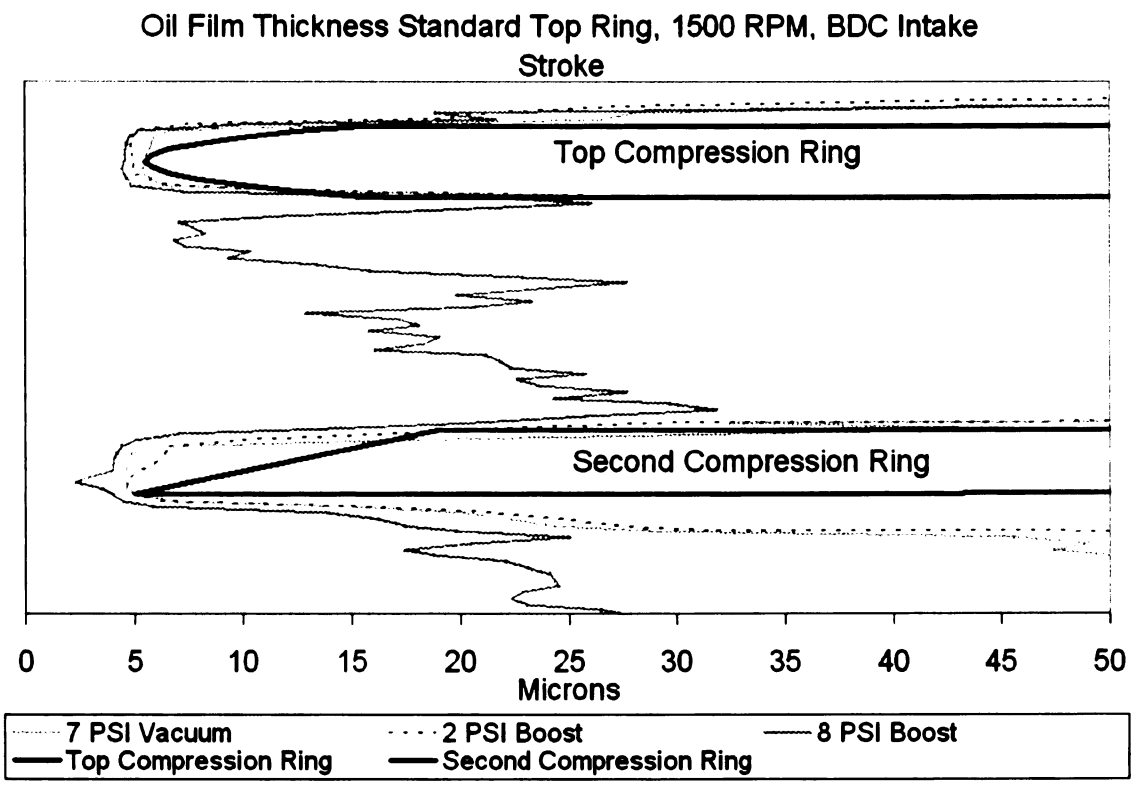

FIGURE 110. Oil film thickness measured at 180 degree CA, 1500 RPM

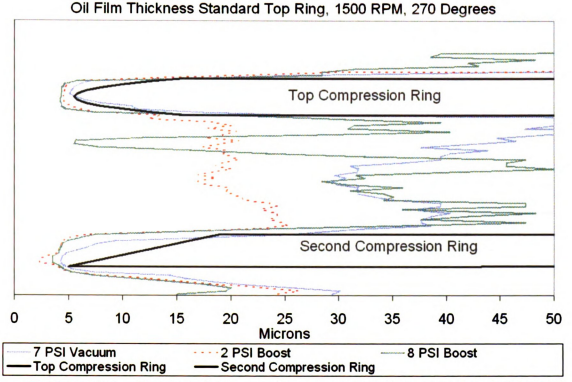

FIGURE 111. Oil film thickness measured at 270 degree CA, 1500 RPM

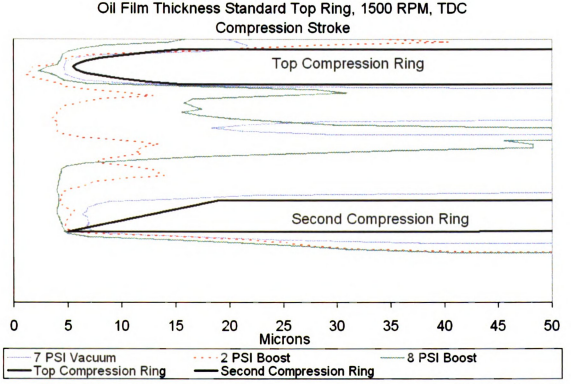

FIGURE 112. Oil film thickness measured at 360 degree CA, 1500 RPM

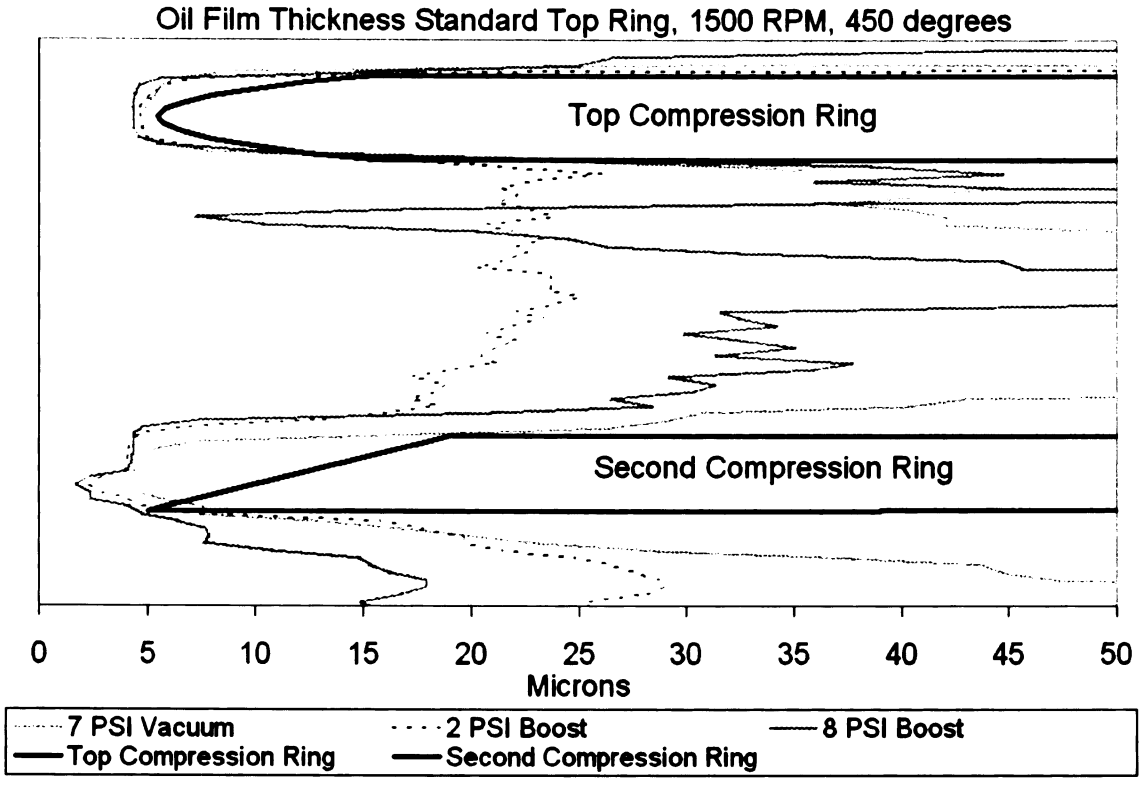

FIGURE 113. Oil film thickness measured at 450 degree CA, 1500 RPM

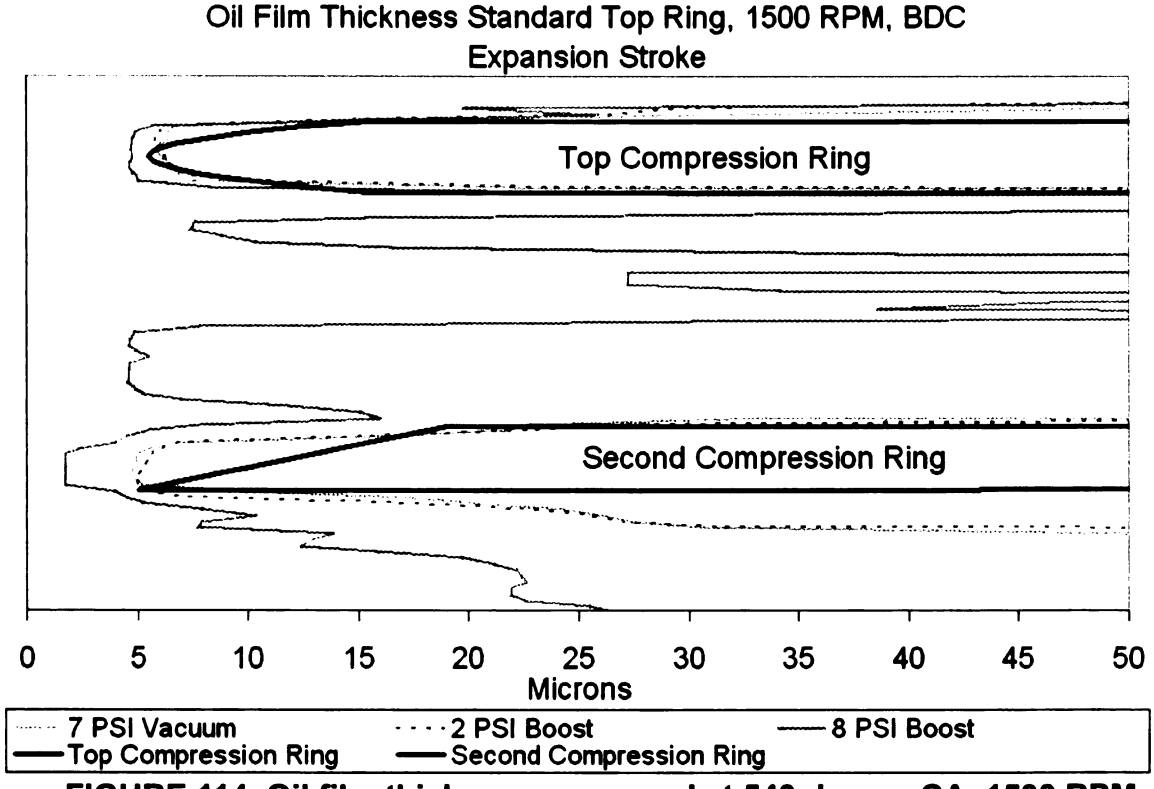

FIGURE 114. Oil film thickness measured at 540 degree CA, 1500 RPM

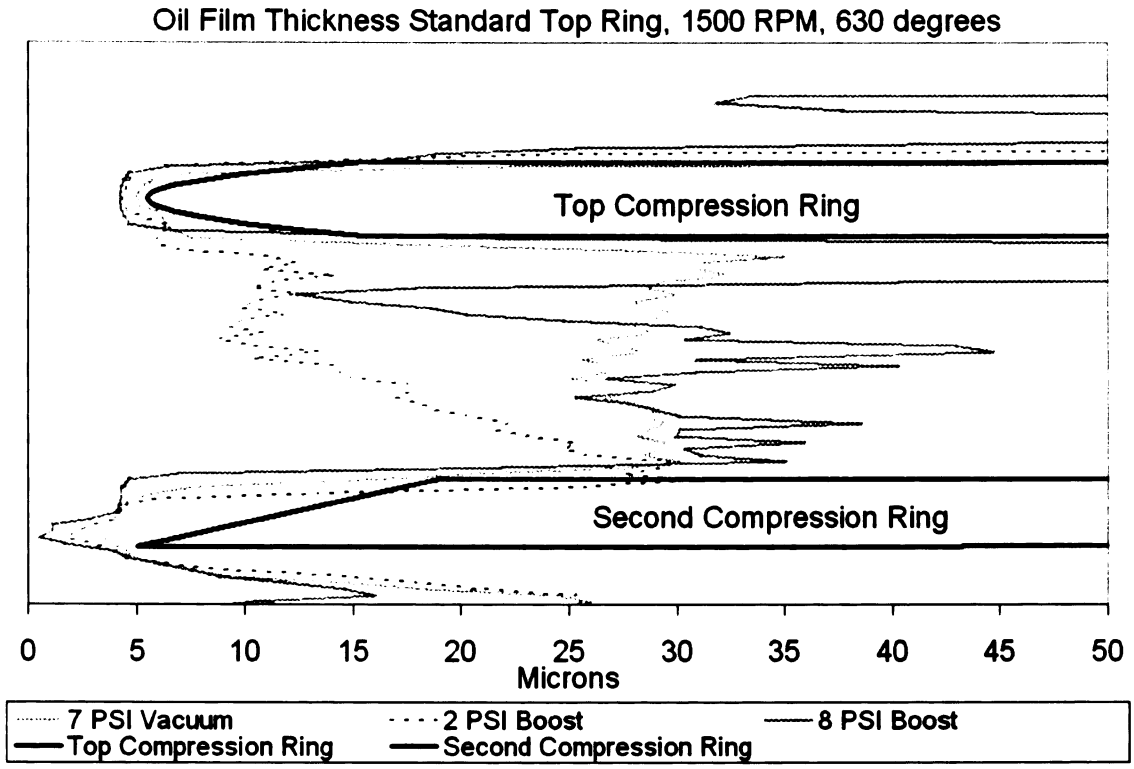

FIGURE 115. Oil film thickness measured at 630 degree CA, 1500 RPM

Figures 116 - 123 show the cyclic variation of oil film thickness of the measurement and of the prediction using the new lubrication model. High discrepancy is observed at the comparison especially at 500 RPM for both the top and second piston rings (Figures 116 to 119). For the top ring oil film thickness at 1500 RPM (Figures 121 and 123), a small degree of similarity in the cyclic variation characteristic is observed except at the BDC, where the model under-predicts the oil film thickness. The sources of error are under investigation for both the experiment and computation. It is to point out here that the amount of data comparison at this stage is rather inadequate to derive conclusive observation. More measurements and comparisons are recommended. The resolution of the

measured oil film thickness needs to be increased in order to capture the detail of cyclic oil film variation. At this stage, only 8 measurements are made over a four-stroke engine cycle, at crank angles of 0, 90, 180, 270, 360, 450, 540 and 630 degree (720 is the same as 0 degree) for the preliminary comparison with the predicted results. In addition, the technique to determine measured minimum oil film thicknesses and ring edges needs to be improved. The ring edges need to be located more precisely from the recorded LIF images so that the oil film thickness profile across ring faces can be determined.

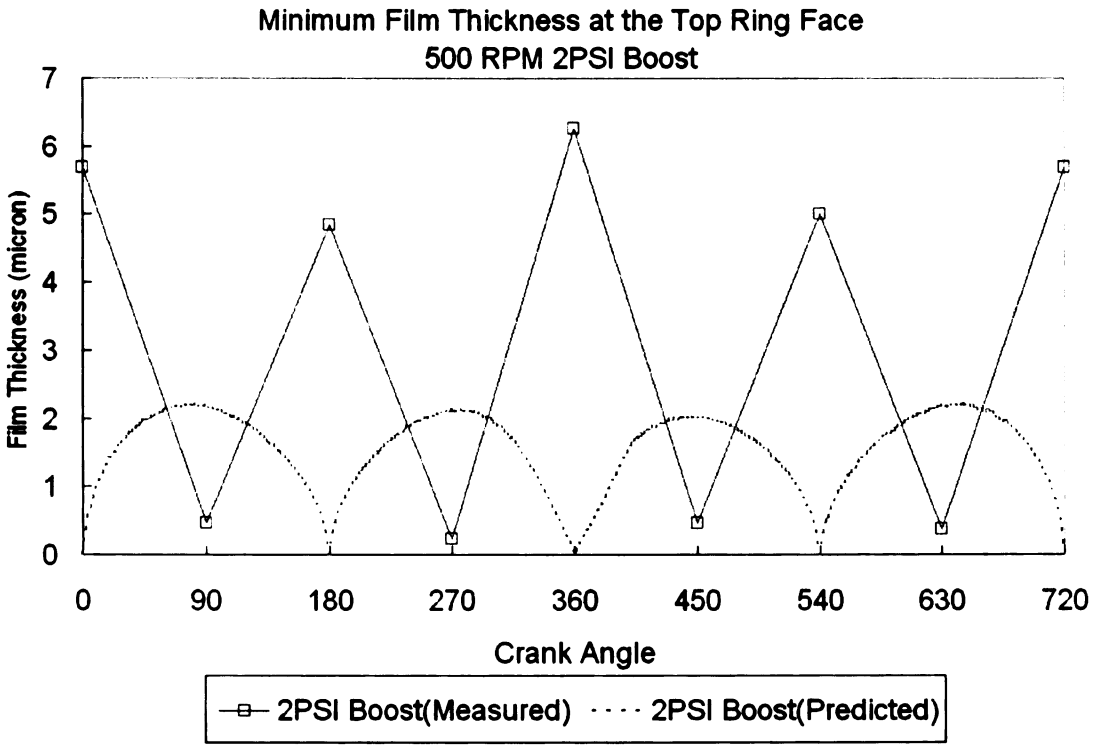

FIGURE 116. Cyclic top ring oil film thickness at 500 RPM 2 PSI Boost

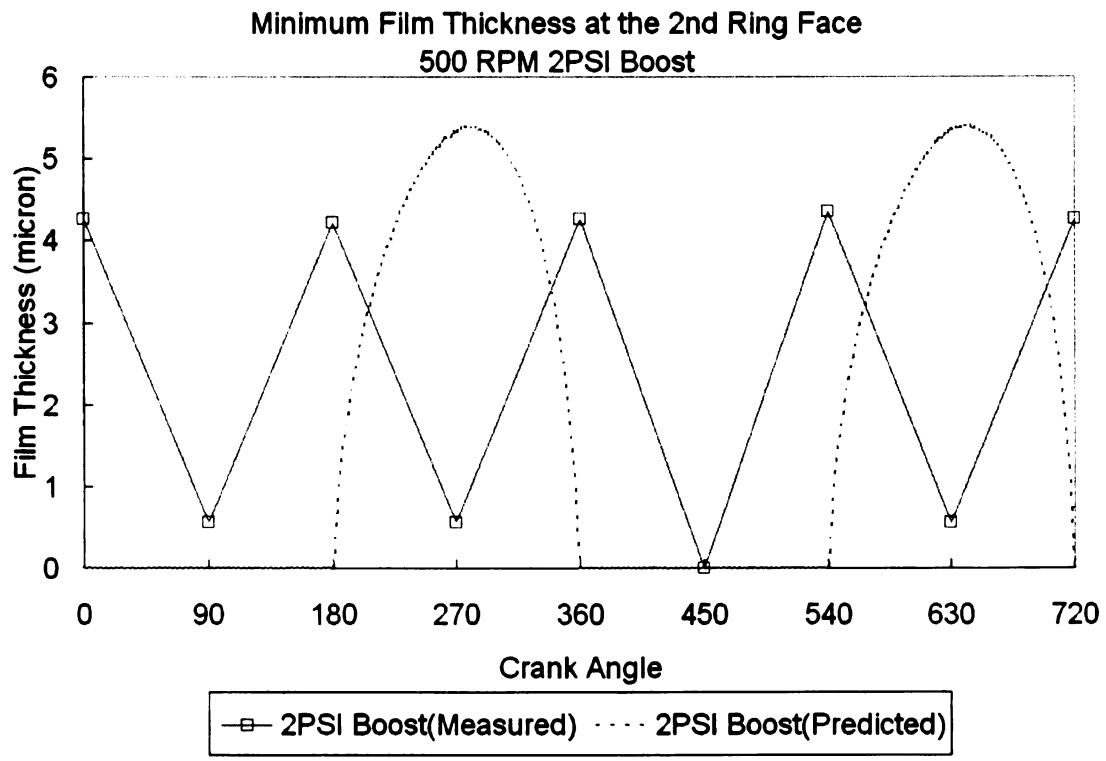

FIGURE 117. Cyclic 2nd ring oil film thickness at 500 RPM 2 PSI Boost

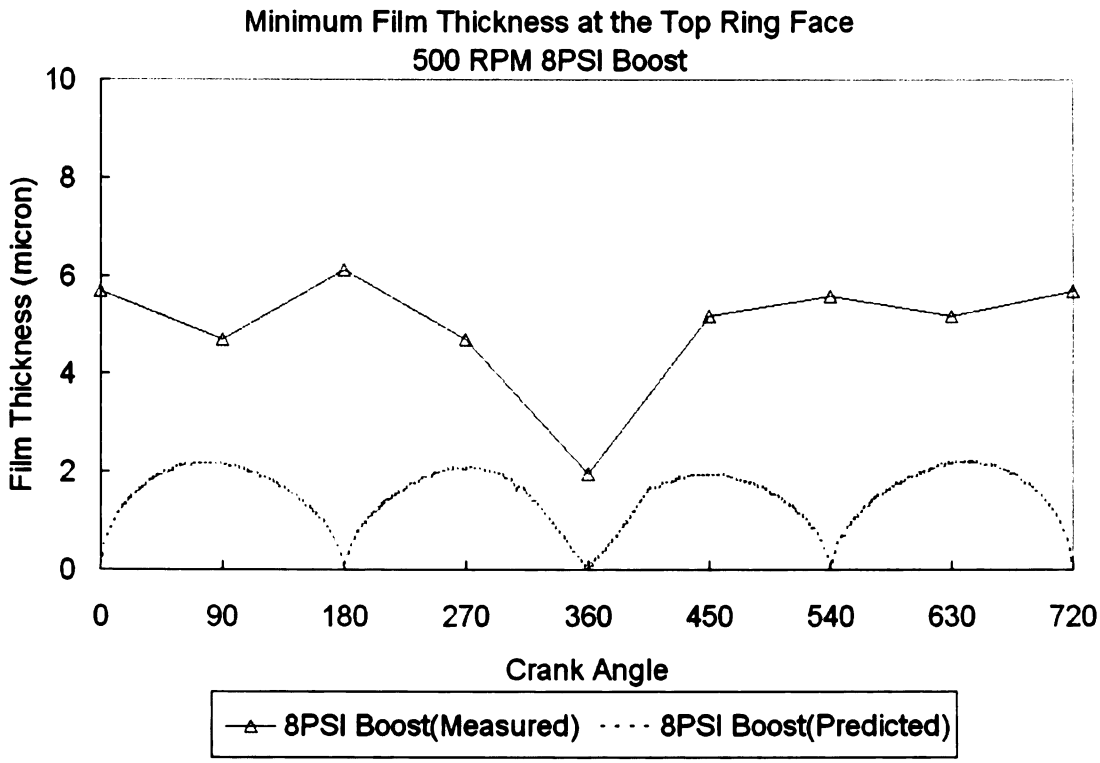

FIGURE 118. Cyclic top ring oil film thickness at 500 RPM 8 PSI Boost

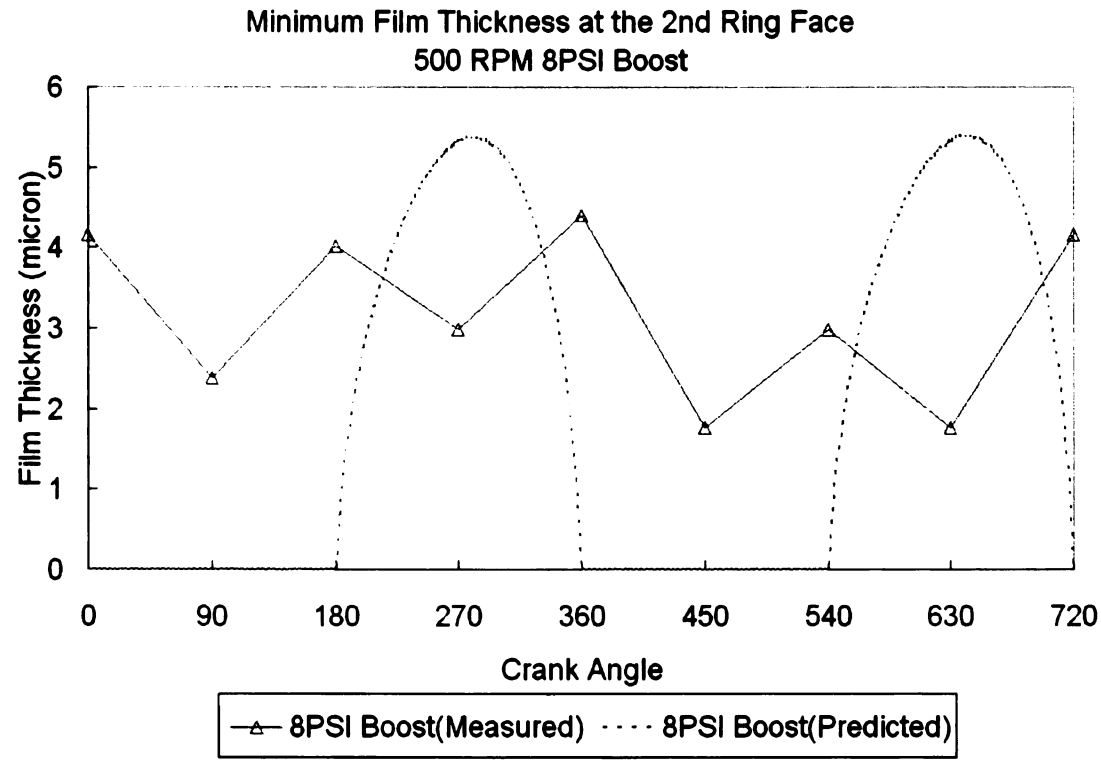

FIGURE 119. Cyclic 2nd ring oil film thickness at 500 RPM 8 PSI Boost

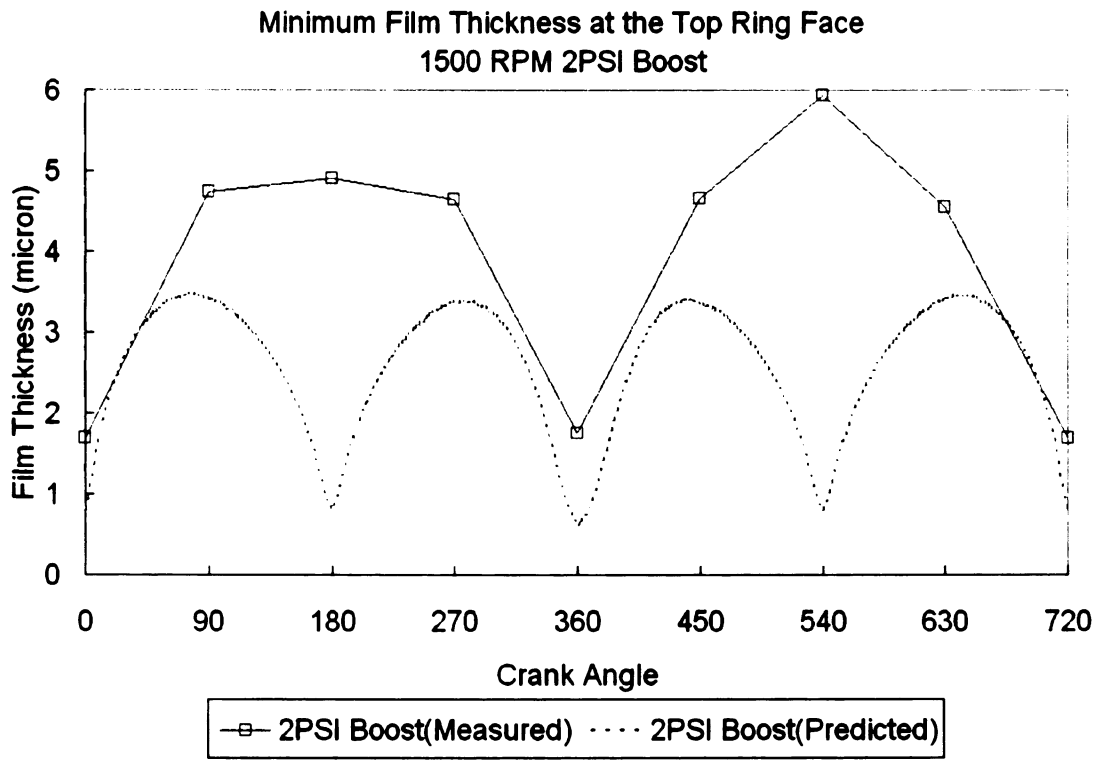

FIGURE 120. Cyclic top ring oil film thickness at 1500 RPM 2 PSI Boost

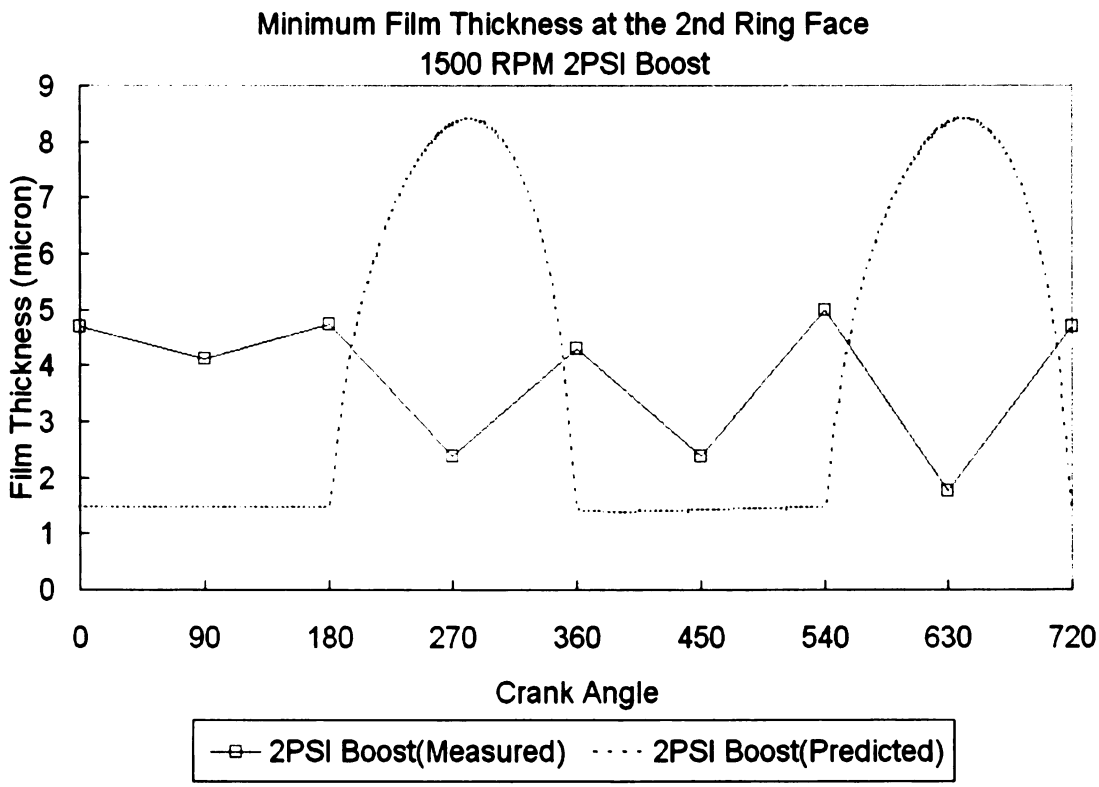

FIGURE 121. Cyclic 2nd ring oil film thickness at 1500 RPM 2 PSI Boost

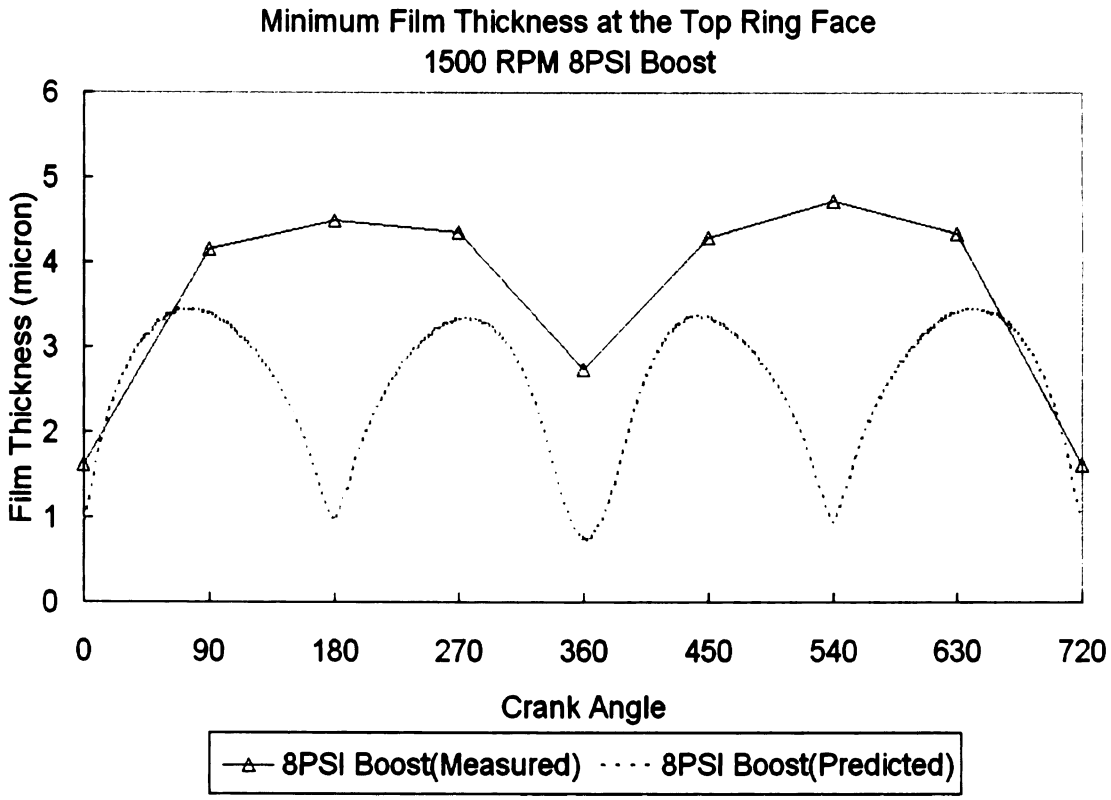

FIGURE 122. Cyclic top ring oil film thickness at 1500 RPM 8 PSI Boost

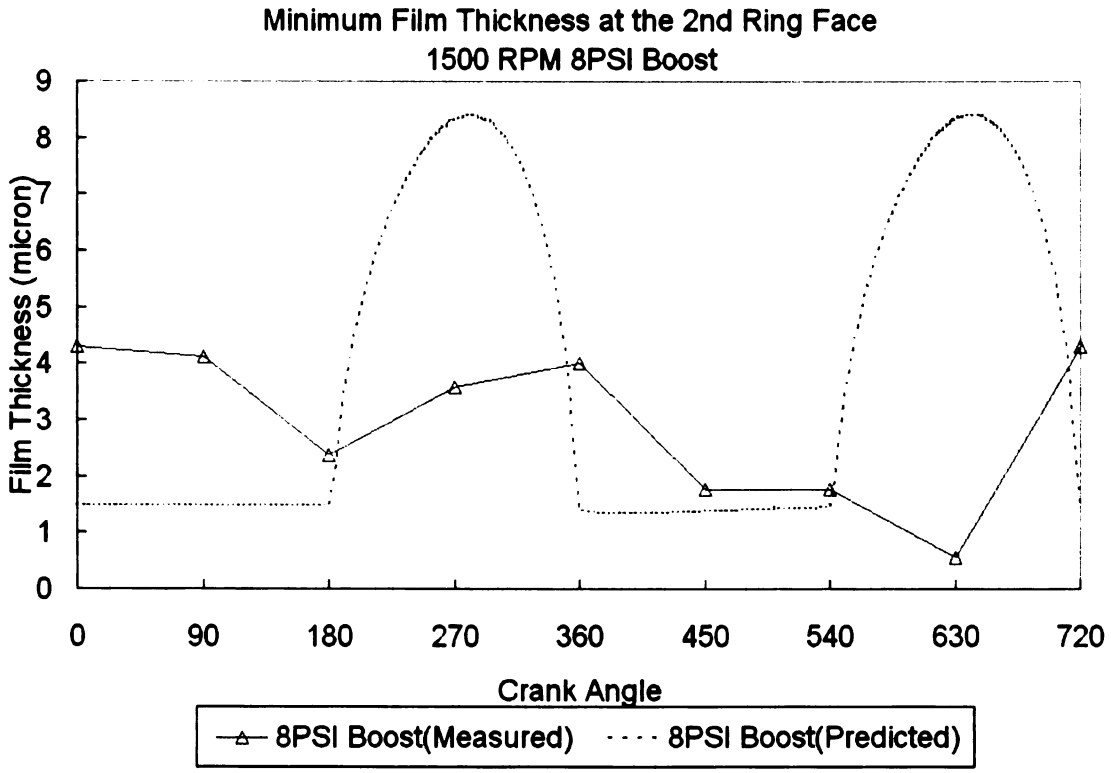

FIGURE 123. Cyclic 2nd ring oil film thickness at 1500 RPM 8 PSI Boost

CHAPTER 7 SUMMARY

Theoretical models have been developed to address the engine tribological phenomena that occur at the conjunction between the cylinder bore and the piston skirt, and between the cylinder bore and the piston rings. These models were implemented in a computational engine simulation system, CASE, and its capabilities were demonstrated in simulating comprehensive engine performances that couple the analyses of ring/bore wear, oil consumption, blowby and backflow, and piston dynamics/elastohydrodynamics (EHL). This chapter provides the conclusions and recommendations of each part of this work, and comments on the importance of integrating them together in order to develop an effective computational tool for engine study.

7.1 Partially Flooded Lubrication

7.1.1 Conclusions

A new piston ring/bore lubrication computational model has been developed, replacing an existing model that only accounts for the fully flooded condition. As was demonstrated here, this model now accounts for a wider range of lubrication conditions that could exist in a piston ring/bore system. Five distinct lubrication regimes are accounted for by this model:

1. Fully flooded hydrodynamic

2. Partially flooded hydrodynamic

3. Fully flooded mixed

4. Partially flooded mixed, and

5. Full boundary (metal-to-metal).

The three-dimensional feature of this model has the ability to account for asymmetrical variation of ring/bore wear and physical boundary conditions. Such variations are commonly found in operating engines due to phenomena such as piston secondary motion (tilt), bore distortion, and bore temperature distribution.

7.1.2 Recommendations

Even though the new lubrication model satisfies both the lubricant flow continuity and force equilibrium at piston/ring bore interaction, some results show abrupt or "step-wise" change from one node to another due to the limited resolution and computational simplifications. Therefore, future recommendations for this model will be to include higher nodal resolution particularly across the ring circumference, or to include detailed numerical flow continuity analysis across the entire ring surface that also involves the trailing edge film attach/detach interaction. This partially flooded lubrication model should be ultimately implemented into a multi-ring piston assembly system for a more realistic engine simulation. Considering the high dynamic ring/groove interaction, especially in diesel engines, the wear phenomenon at the ring/groove region needs to be included.

7.2 Oil Vaporization Effect on Partially Flooded Lubrication

7.2.1 Conclusions

A coupled model of oil vaporization and partially flooded mixed lubrication has been presented along with its application on a modern diesel engine system. In its application on a diesel engine system, unique results have been predicted by this model in comparison with other piston ring lubrication models. Results with CASE demonstrate its uniqueness and the importance of including oil evaporative analysis in partially flooded analysis. Simulations successfully show the appearance of local bore wear pockets induced from locally concentrated higher-than-surrounding bore temperature, which potentially represents the wear-inducing interactions between the fuel injection plumes and the bore wear. The application is further conducted in temperature-sensitive bore wear analysis in order to determine the range of critical temperature that will cause excessive bore wear. Observation from the analysis shows a drastic increase of the bore wear pocket at a small degree of temperature rise at the critical temperature range (about 50^{o}C increase from the surrounding). This finding is very critical in the development of diesel engine injection spray systems, considering the potential of temperature-induced high wear from the injection plumes on the cylinder bore that can disrupt the entire engine performance and structure strength.

Examination of the results also offers useful information regarding the factors that contribute to the thinning of oil film. The first analysis uses the same bore temperature distribution where hot spot temperature is about 280^{o}C (100^{o}C

higher than surrounding area). Here, all results, with and without the oil evaporation analysis, show a different degree of wear increase at hot spots, indicating the increase of local asperity contact pressure. The increase of asperity contact implies that ring/bore surfaces are interacting with a thinner oil film. Without evaporative influence, the thinning of oil film thickness is minimal because it is attributed merely to the oil viscosity reduction at high temperature. By including evaporation analysis, the result indicates substantial oil film thickness loss due to evaporation. The dominant effect of evaporation on oil film loss at high temperature, in comparison to viscosity reduction, implies that a piston ring/bore lubrication model with oil evaporation analysis can better capture the tribological behavior of an engine operating in extreme conditions. One sees the same behavior in most modern diesel engines, which have a higher compression ratio than gasoline engines.

7.2.2 Recommendations

The evaporation analysis can be improved to represent the physics of the heat transfer system more closely. For example, one can include transient heat conduction analysis on the heat source and bore temperature interaction and perform continuous engine cycle analysis to verify if the prediction from the evaporation-coupled analysis is realistic in comparison with practical engine operation. The evaporation analysis can also be extended to account for composite oil instead of single-specie oil if oil data are available. For the diesel engine application, experimental effort is necessary to verify the predicted results on the temperature-induced bore wear pocket.

7.3 Piston EHL Model

7.3.1 Conclusions

A stand-alone model for the three-dimensional piston simulation has been developed to be used in the study of piston design and analysis. This model improves on other piston models (seen in publication) that usually do not have all built-in finite element tools for a complete piston analysis to be conducted automatically. The present model is considered a more advanced and efficient CAE tool: it comprises built-in modules that automatically construct the piston finite element solid model, solve for the thermal and static analysis, and simulate the entire cyclic analysis of piston dynamics coupled with piston skirt elastohydrodynamic lubrication.

Preliminary testing on a production engine demonstrates the capability of this model in performing a comprehensive piston study. The simulation results show that cylinder gas pressure load and engine speed play significant and interdependent roles in determining piston trajectory and skirt elastohydrodynamic lubrication.

7.3.2 Recommendations

A comparison of the finite element analysis results, using the simplified piston model and the actual model, shows that the simplified model must be improved in order to capture the physics more closely, for example including the piston pin holes and a more detailed pin boss geometry. Otherwise, the piston model can be extended to have the capability of including an actual piston

geometry rather than the simplified geometry if computational time is not an issue in a particular analysis. On top of that, the multi-mode lubrication wear model, which has been implemented in the ring model, needs to be extended to the piston skirt lubrication calculation to account for metal-to-metal contact and piston skirt wear.

7.4 Experimental Validation

7.4.1 Conclusions

Experiments have been conducted for the comparison of the piston ring pack gas pressures and the oil film thickness predicted using the computational models. Predictions agree reasonably well with the oil film thickness and inter-ring gas pressure measurements in the optical engine. The experimental data also shows that the fully flooded condition is a valid assumption for piston rings below the top compression ring as it is seen that a substantial amount of oil is trapped at the inter-ring region, suppling oil for full lubrication on those piston rings.

7.4.2 Recommendations

The discrepancy of the inter-ring gas pressure near the bottom of the piston ring pack can be improved by incorporating the input of measured crankcase pressures or a new model that can estimate the crankcase dynamic pressures. This will provide accurate boundary conditions for the computation of the inter-ring gas pressures.

The current measurements of oil film thickness over an engine cycle are only conducted at eight different degree crank angles (0,90,180,270,360,450,540 and 630). As a result, any conclusive observation with respect to the prediction is difficult to make. More measurement need to be acquired for further validation of the new lubrication model.

7.5 Closure

The developments of several engine tribological models, from theory to computational module, have been presented in this dissertation. Even though each model represents an important subsystem of an engine, proper integrating of these tribological models into a main engine system, along with other subsystems of gas dynamics, heat transfer and structural mechanics and dynamics, proves to be a more crucial step in arriving a comprehensive engine simulation system that can better represent a real engine performance. Hence, every subsystem is essentially dependent on other subsystem for it to be applicable in the engine analysis. The computational efficiency, accuracy, and the applicability of the improved CASE system have been validated through various practical engine applications. The uniqueness of this developed engine system can be summarized as follows:

1. its advanced technology in predicting three-dimensional ring/bore wear (from literature survey: it is the only known model in the engine research field capable of doing this),

2. its advanced technology in integrating major built-in modules (finite element and dynamic) into a single simulation so that a complete comprehensive piston EHL performance can be performed automatically,

3. its capability of simulating five lubrication regimes at the ring/bore interface,

4. its capability of simulating four piston kinematic modes, and

5. experimental verification using the optical engine system.

The robustness and validation of the new engine system CASE potentially allows it to be a very crucial tool in the engine design, particularly when it is integrated into an optimization system. Consider its computational efficiency in which an engine simulation can be conducted at a relatively short time (about 15 minutes per engine operating condition on a 2.4 GHz Pentium 4 PC), a parametric study to arrive an optimized configuration of engine system for desired performance output, or an engine performance study over a range of engine speeds and loads, can be accomplished within a period of days. This essentially implies that the application of CASE can help in reducing a significant amount of time and cost in the conventional design process (usually takes months or years) and contribute to the ultimate production of modern engines with higher durability, higher efficiency and lower emission.

BIBLIOGRAPHY

1.) Allen, D.G., Dudley, B.R., Middleton, V. and Parker, D.A., 1975, "Prediction of Piston Ring-Cylinder Bore Oil Film Thickness in Two Particular Engines and Correlation with Experimental Evidence," *Proc IMechE Conference on Piston Ring Scuffing*, Paper No. C73/75.

2.) Archad, J.F., 1953, "Contact and Rubbing of Flat Surfaces," *J. of Applied Physics*, Vol. 24, No. 8, pp. 981-988.

3.) Audette, W.E. III, and Wong, V.W., 1999, "A Model for Estimating Oil Vaporization from the Cylinder Liner as a Contributing Mechanism to Engine Oil Consumption," SAE Paper 1999-01-1520.

4.) Audette, W.E. III and Wong, V.W, 2000, "Oil Transport Along the Engine Cylinder Liner - Coupling Vaporization and Film Thickness Analysis," 12th International Colloquium Tribology, Tribology 2000 - Plus, January 11th - 13th, 2000, W. J. Bartz (publisher), Vol. 1.

5.) Baker, A.J.S., Dowson, D. and Strachan, P., 1973, "Dynamic Operating Factors in Piston Rings," International Symposium of Marine Engineers, Paper 256, Tokyo, Japan.

6.) Barkman, D.A., 1992, " An Evaluation of the Parameters Involved in Developing A Radiotracer Based Wear Diagnostics System," M.S. Thesis, Mechanical Engineering Department, Michigan State University, East Lansing, MI, USA.

7.) Bishop, I.N., 1960, "Effect of Design Variables on Friction and Economy," from *Engine Oil Effects on Vehicle Fuel Economy - Progress in Technology,* Series No. 27, SAE Paper No. 812A.

8.) Brombolich, L.J., 1988, "Effect of Cylinder Distortion and Piston Ring Design on Oil Consumption and Friction Losses in Automotive Engines," Contract No. DE-AC02-86CE-90236, Report to US Department of Energy.

9.) Brown, S.R. and Hamilton, G.M.,1977, "The Partially Lubricated Piston Ring," *J. Mech. Eng. Sci.*, Vol. 19, No. 2, pp. 81-89.

10.) Bush, A.W. and Gibson, R.D., 1980, "The Effect of Surface Roughness and Elastic Deformation in Hydrodynamic Lubrication - A Perturbation Approach," *Surface Roughness Effects in Hydrodynamics and Mixed Lubrication*, ASME Publication, pp. 51-73.

11.) Cameron, A., 1966, *Principles of Lubrication*, John Wiley and Sons Inc. New York.

12.) Cameron, A., 1971, *Basic Lubrication Theory*, Harlow, Longman.

13.) *CASE Theoretical Manual*, 2003, Mid Michigan Research, Okemos, MI.

14.) *CASE User's Manual*, 2003, Mid Michigan Research, Okemos, MI.

15.) Castleman, R.A., 1936, "A Hydrodynamic Theory of Piston Ring Lubrication," *Physics*, Vol. 7, pp. 364-367.

16.) Chow, P.L. and Saibel, E.A., 1978, "On the Roughness Effect in Hydrodynamic Lubrication," Trans. of the ASME, Vol. 100, pp. 176-180.

17.) Christensen, H., 1972, "A Theory of Mixed Lubrication," *Proc. IMechE.* Vol. 186, pp.421-430.

18.) Chui, B.K., 2001, "Computational Analysis of Oil Consumption and Piston Ring Wear," M.S. Thesis, Mechanical Engineering Department, Michigan State University, East Lansing, MI, USA.

19.) Chui, B.K. and Schock, H.J., 2002, "Computational Analysis of Piston-Ring Wear and Oil Consumption for an Internal Combustion Engine," Proceedings of the 2002 Fall Technical Conference of the ASME Internal Combustion Engine Division, September 2002, New Orleans, Louisiana, Paper No.: ICEF2002-529, pp. 461-469.

20.) Chung, Y.S., 1992, "Development and Analysis of a Fire Ring Wear Model for a Piston Engine," Ph.D. Thesis, Mechanical Engineering Department, Michigan State University, East Lansing, MI, USA.

21.) Chung, Y.S., Schock, H.J., and Brombolich, L.J., 1993, "Fire Ring Wear Analysis for a Piston Engine," SAE Paper 930797.

22.) .Cleveland, A.E. and Bishop, I.N., 1960, "Several Possible Paths to Improved Part-load Economy of Spark-ignition Engines," SAE Paper 150A.

23.) Dowson, D., Economou, P.N., Ruddy, B.L., Strachan, P.J., and Baker, A.J. S., 1979, "Piston Ring Lubrication - Part 2. Theoretical Analysis of a Single Ring and a Complete Ring Pack," *Energy Conservation Through Fluid Film Lubrication Technology: Frontiers in Research and Design*, Winter Annual Meeting of ASME, pp. 23-52.

24.) Dowson, D., Ruddy, B.L., and Economou, P.N., 1983, "The Elastohydrodynamic Lubrication of Piston Rings," *Proc. R. Soc. Lond.*, Ser. A, Vol. 386, pp. 409-430.

25.) Dursunkaya, Z. and Keribar, R., 1992, "Simulation of Secondary Dynamics of Articulated and Conventional Piston Assemblies," SAE Paper 920484.

26.) Dursunkaya, Z., Keribar, R. and Ganapathy, V., 1994, "A Model of Piston Secondary Motion and Elastohydrodynamic Skirt Lubrication," *ASME J. of Trib.*, Vol. 116, October, pp. 777-785.

27.) Eilon, S. and Saunders, O. A., 1957, "A Study of Piston-Ring Lubrication," *Proc. Inst. Mech. Engrs.*, Vol. 171, pp. 427-443.

28.) Ejakov, M.A., 1998, "Ring Pack Behavior and Oil Consumption Modeling in IC Engines," Ph.D. Thesis, Mechanical Engineering Department, Michigan State University, East Lansing, MI, USA.

29.) Ejakov, M.A., Schock, H.J., Brombolich, L.J. and Williams, R.L., 1996, "Comparison Between Predicted and Measured Inter-Ring Gas Pressures and Analysis of Factors Affecting Them," DAR 96-00858, Ford Design Analysis Report, November.

30.) Ejakov, M. A., Hascher, H. G., Schock, H. J., Brombolich, L. J., Trinker, F. H., and LoRusso, J. A., 1996, "Simulation Analysis of Ring Pack Behavior in a Deactivated Cylinder," ICE-Vol. 27-2, 1996 Fall Technical Conference, Vol. 2, ASME.

31.) Ejakov, M. A., Schock, H. J., Brombolich, L. J., Carlstrom, C. M., and Williams, R. L., 1997, "Simulation Analysis of Inter-Ring Gas Pressure and Ring Dynamics and Their Effect on Blow-by," ICE-Vol. 29-2, 1997 Fall Technical Conference, Vol. 2, ASME Paper No.: 97-ICE-50.

32.) Ejakov, M.A., Schock, H.J. and Brombolich, L.J., 1998, "Modeling of Ring Twist for an IC Engine," SAE Paper 982693

33.) Ejakov, M.A., Diaz, A.R. and Schock, H.J., 1999, "Numerical Optimization of Ring-Pack Behavior," SAE Paper 1999-01-1521

34.) Ejakov, M.A., 2001, "Modeling of Axial and Circumferential Ring Pack Lubrication," ICE-Vol 37-3, 2001 Fall Technical Conference, Vol. 3, ASME Paper No. 2001-ICE-433.

35.) Ejakov, M.A., Yeager, D.A., and Kayupov, M., 2003, "Reliability and Robustness Analysis of Engine Ring-Pack Performance," SAE Paper 2000-01-1221.

36.) Fedewa, A. and Schock, H.J., 2004, "Tribological Phenomena for Advanced Diesel Engines," Contract No. DAAE07-03-C-L021, Report to US Army Tank Automotive Command, November 15.

37.) Fielding, B.J. and Skorecki, J., 1969-1970, "Identification of Mechanical Sources of Noise in a Diesel Engine: Sound Originating from Piston Slap," *Proc. Inst. Mech. Eng.*, Vol. 184, Part I, No. 46, pp. 859-871.

38.) Fuller, D.D., 1978, *Theory and Practice of Lubrication for Engineers,* 2nd Ed., John Wiley & Sons, New York.

39.) Furuhama, S., 1959, "A Dynamic Theory of Piston-Ring Lubrication (1st Report: Calculation)," *Bul. of JSME*, Vol. 2, No. 7, pp. 423-428.

40.) Furuhama, S., 1960, "A Dynamic Theory of Piston-Ring Lubrication (2nd Report: Experiment)," *Bul. of JSME*, Vol. 3, No. 10, pp. 291-297.

41.) Furuhama, S., 1961, "A Dynamic Theory of Piston-Ring Lubrication (3rd Report: Measurement of Oil Film Thickness)," *Bul. of JSME*, Vol. 4, No. 16, pp. 744-752.

42.) Furuhama, S., Takiguchi, M. and Tomizawa, K., 1981, "Effect of Piston and Piston Ring Designs on the Piston Friction Forces in Diesel Engines," SAE Paper 810977.

43.) Glidewell, J., and Korcek, S., 1998, "Piston Ring/Cylinder Bore Friction Under Flooded and Starved Lubrication Using Fresh and Aged Engine Oils," SAE Paper 982659.

44.) Goenka, P.K. and Meemik, P.R., 1992, "Lubrication Analysis of Piston Skirts," SAE Paper 920490.

45.) Greenwood, J.A., and Tripp, J.H., 1971, "The Contact of Two Nominally Flat Surfaces," *Proc. Inst. Mech. Engrs.*, Vol. 185, pp. 625-632.

46.) Grice, N., 1990, "An Experimental and Theoretical Study of Piston Ring Lubrication," Ph. D. Thesis, Lancashire Polytechnic in collaboration with B. P. Research International, UK, October.

47.) Griffiths, W.J. and Skorecki, J., 1964, "Some Aspects of Vibration on a Single Cylinder Diesel Engine," *J. Sound Vibration*, Vol. 1, No. 4, pp. 345-364.

48.) Hamilton, G.M. and Moore, S.L., 1974, "The Lubrication of Piston Rings. First Paper. Measurement of the Oil Film Thickness between the Piston Rings and Liner of a Small Diesel Engine," *Proc. Inst. Mech. Engrs.*, Vol. 188, pp. 253-261.

49.) Hamilton, G.M., Moore, S.L., 1974, "The Lubrication of Piston Rings. Second Paper. Comparison between Measured and Calculated Thicknesses of the Oil Film Lubricating Piston Rings," *Proc. Inst. Mech. Engrs.*, Vol. 188, pp. 262-268.

50.) Hersey, M., 1966, *Theory and Research in Lubrication; Foundations for Future Developments*, John Wiley & Sons Inc., New York

51.) Heywood, J.B., 1988, *Internal Combustion Engine Fundamentals*, McGraw-Hill, Inc., New York

52.) Hoult, D.P. et al., 1988, "Calibration of Laser Fluorescence Measurement of Lubricant Film Thickness in Engines," SAE Paper 881587.

53.) Ishizuki, Y., Sato, R., and Takase, K., 1981, "Effect of Cylinder Liner Wear on Oil Consumption in Heavy Duty Diesel Engines," SAE Paper 810931.

54.) Jeng, Y.R., 1992, "Friction and Lubrication Analysis of a Piston-Ring Pack," SAE Paper 920492.

55.) Kajiwara, H., Fujioka, Y. and Negishi, H., 2003, "Prediction of Temperatures on Pistons with Cooling Gallery in Diesel Engines using CFD Tool," SAE Paper 2003-01-0986.

56.) Keribar, R. and Dursunkaya, Z., 1992, "A Comprehensive Model of Piston Skirt Lubrication," SAE Paper 920483.

57.) Keribar, R., Dursunkaya, Z., and Ganapathy, V., 1993, "An Integrated Design Analysis Methodology to Address Piston Tribological Issues," SAE Paper 930793.

58.) Knoll, G.D. and Peeken, H.J., 1982, "Hydrodynamic Lubrication of Piston Skirts," *J. of Lubrication Technology*, Vol. 104, pp. 504-509, October.

59.) Knoll, G, Peeken, H., Lechtape-Gruter, R. and Lang, J., 1994, "Computer Aided Simulation of Piston and Piston Ring Dynamics," from *Heavy Duty Engines: A Look at the Future,* ASME 1994 Conference, ICE-Vol. 22, pp. 301-309.

60.) Laws, A.M., Parker, D.A. and Turner, B., 1973, "Piston Movement in Diesel Engine," Paper No. 33, CIMAC Conference, Washington D.C., pp. 809-831.

61.) Lee, Y.Z. and Ludema, K.C., 1990, "The Shared-Load Wear Model in Lubricated Sliding Scuffing Criteria and Wear Coefficients," *WEAR*, Vol. 138, pp. 13.

62.) Li, C.H., 1986, "Thermoelastic Behavior of an Aluminum Diesel Engine Piston," SAE Paper 860136.

63.) Li, D.F., Rohde, S.M., and Ezzat, H.A., 1983, "An Automotive Piston Lubrication Model," ASLE Transactions, Vol. 26, No. 2, pp. 151-160.

64.) Liu, S.H., Li, J., Zhou, L.B., Rong, W., 1996, "An Experimental Investigation of the Oil Film Lubricating Piston Rings," SAE Paper 961912.

65.) Lloyd, T., 1968, "The Hydrodynamic Lubrication of Piston Rings," *Proc. Inst. Mech. Engrs*, Vol. 183, pp. 28-34.

66.) Ludema, K.C., 1996, *Friction, Wear, Lubrication, A Textbook in Tribology*, CRC Press, New York.

67.) Ma, Z., Henein, N.A., Bryzik, W., and Glidewell, J., 1998, "Break-In Liner Wear and Piston Ring Assembly Friction in a Spark-Ignited Engine," STLE Preprinted No. 98-AM-3D-1, Presentation at 53rd STLE Annual Meeting, Detroit, MI.

68.) Ma, M-T, Smith, E.H. and Sherrington, I., 1995, "A Three-Dimensional Analysis of Piston Ring Lubrication. Part 1: Modeling," *Proc. Inst. Mech. Engrs.*, Part J, Vol. 209, pp. 1-14.

69.) Ma, M-T, Smith, E.H. and Sherrington, I., 1995, "A Three-Dimensional Analysis of Piston Ring Lubrication. Part 2: Sensitivity Analysis," *Proc. Inst. Mech. Engrs.*, Part J, Vol. 209, pp. 15-27.

70.) Ma, M-T, Smith, E.H. and Sherrington, I., 1996, "Implementation of an algorithm to Model the Starved Lubrication of a Piston-Ring in Distorted Bores; Prediction of Oil Flow and Onset of Gas Blow-by," *Proc. Inst. Mech. Engrs.*, Part J, Vol. 210, pp. 29-44.

71.) Ma, M-T, Sherrington, I. and Smith, E.H., 1997, "Analysis of Lubrication and Friction for a Complete Piston-Ring Pack with an Improved Oil Availability Model. Part 1: Circumferentially Uniform Film," *Proc. Inst. Mech. Engrs.*, Part J, Vol. 211, pp. 1-15.

72.) Ma, M-T, Smith, E.H. and Sherrington, I., 1997, "Analysis of Lubrication and Friction for a Complete Piston-Ring Pack with an Improved Oil Availability Model. Part 2: Circumferentially Variable Film," *Proc. Inst. Mech. Engrs.*, Part J, Vol. 211, pp. 17-27.

73.) McGeehan, J.A., 1978, "Literature Review of the Effects of Piston Ring Friction and Lubricating Oil Viscosity on Fuel Economy," from *Engine Oil Effects on Vehicle Fuel Economy - Progress in Technology,* Series No. 27, SAE Paper 780673.

74.) McGeehan, J.A., 1979, "A Survey of the Mechanical Design Factors Affecting Engine Oil Consumption," SAE Paper 790864.

75.) Moore, S.L. and Hamilton, G.M., 1978, "The Starved Lubrication of Piston Rings in a Diesel Engine," *J. of Mech. Engrg. Sci.*, Vol. 20, No. 6, p. 345.

76.) Munro, R., and Parker, A., 1975, "Transverse Movement Analysis and Its Influence on Diesel Piston Design," SAE Paper 750800.

77.) Munson, B.R., Young, D.F. and Okiishi, T.H., 1998, *Fundamentals of Fluid Mechanics,* 3rd Ed. John Wiley & Sons, Inc., New York.

78.) Nakayama, K., Seki, T., Takiguchi, M., Someya, T., and Furuhama, S., 1998, "Effect of Oil Ring Geometry on Oil Film Thickness in the Circumferential Direction of the Cylinder," SAE Paper 982578.

79.) Oguri, A., Totii, H., Hosokawa, T. and Nakada, M., 1988, "Development of Analysis Model for Piston Movement," SAE Paper 885031.

80.) Oh, K.P., Li, C.H. and Goenka, P.K., 1987, "Elastohydrodynamic Lubrication of Piston Skirts," ASME *J. of Tribology*, Vol. 109, pp. 356-362.

81.) Parker, D.A., 1989, "The Tribology of Automotive Components: Development of Verified Predictive Design Techniques," Fourth BP/IMechE Tribology Lecture, Part D, *J. of Automobile Engineering*.

82.) Patir, N. and Cheng, H.S. 1978, "An Average Flow Model for Determining Effects of Three-Dimensional Roughness on Partial Hydrodynamic Lubrication," ASME *J. of Lubrication Technology*, Vol. 100, January, pp. 12-17.

83.) Patir, N. and Cheng, H.S. 1979, "Application of Average Flow Model to Lubrication Between Rough Sliding Surfaces," Vol. 101, April, pp. 220-230.

84.) Pint, S., and Schock, H.J., 2000, "Design and Development of a Software Module for Analysis of Three Dimensional Piston Ring Wear," SAE Paper 2000-01-0920.

85.) *PISTON DYNAMICS PROGRAM*, 1991, Compu-Tec Engineering, Chesterfield, Missouri.

86.) Ramchandani, M. and Whitehouse, N.D., 1976, "Heat Transfer in a Piston of a Four Stroke Diesel Engine," SAE Paper 760007.

87.) Reddi, M.M., 1969, "Finite Element Solution of the Incompressible Lubrication Problem," *J. of Lubrication Technology*, July, pp. 524-533.

88.) Reddi, M.M. and Chu, T.Y., 1970, "Finite Element Solution of the Steady-State Compressible Lubrication Problem," *J. of Lubrication Technology*, July, pp. 495-503.

89.) Richardo, H. and Hempson, J.G.G., 1968, "The High Speed Internal Combustion Engine," Blackie, London, 5th Ed., pp. 139-141.

90.) Richardson, D.E., 1990, "The Development and Implementation of Theoretical and Experimental Methods for Studying Oil Films in Engine Cylinders," Ph.D. Dissertation, University of Wisconsin, Madison, Wisconsin.

91.) Roehrie, M.D., 1978, "Thermal Effects on Diesel Engine Pistons," SAE Paper 780781.

92.) Rogowski, A.R., 1961, "Method of Measuring the Instantaneous Friction of Piston Rings in a Firing Engine," SAE Paper 379F.

93.) Rohde, S.M., 1980, "A Mixed Friction Model for Dynamically Loaded Contacts with Application to Piston Ring Lubrication," *Surface Roughness Effects in Hydrodynamics and Mixed Lubrication*, ASME Publication, pp. 19-50.

94.) Rosenberg, R.C., "General Friction Considerations for Engine Design," SAE Paper 821576.

95.) Ryan, J.P., Wong, V.W., Lyon, R.H., Hoult, D.P., Sekiya, Y., Kobayashi, Y., and Aoyama, S., 1994, "Engine Experiments on the Effects of Design and Operational Parameters on Piston Secondary Motion and Piston Slap," SAE Paper 940695.

96.) Ruddy, B.L., Dowson, D., Economou, P.N. and Baker, A.J.S., 1979, "Piston Ring Lubrication - Part III: The Influence of Ring Dynamics and Ring Twist," Energy Conservation Through Fluid Film Lubrication Technology: Frontiers in Research Design, Winter Annual Meeting of ASME, December, ASME Publication, New York, pp. 191-215.

97.) Ruddy, B.L., Parsons, B., Dowson, D. and Economou, P.N., 1980, "The Influence of Thermal Distortion and Wear of Piston Ring Grooves Upon the Lubrication of Piston Rings in Diesel Engines," *Proc. 6th Leeds-Lyon Symp. on Tribology: Thermal Effects in Tribology,* Bury St., Edmunds, U.K., pp. 84-94.

98.) Ruddy, B.L., Dowson, D. and Economou, P.N., 1981, "A Theoretical Analysis of the Twin-Land Type of Oil-Control Piston Ring," *J. Mechanical Engineering Science*, Vol. 23, No. 2, pp. 51-62, 1981.

99.) Sander, W., Steidle, W. and Wacker, E., 1979, "Piston Movement and Its Influence on Noise of Automotive Engines," SAE Paper 790272.

100.) Saugerud, O.T., Sandsmark, N. and Veritas, D., 1979, "Strength Analysis of Thermally Loaded Engine Components by Two-Dimensional and Three-Dimensional Finite Element Models," SAE Paper 790820.

101.) Schneider, E.W., Blossfeld, D.H., and Balnaves, M.A., 1988, "Effect of Speed and Power Output on Piston Ring Wear in Diesel Engine," SAE Paper 880672.

102.) Stanley, R., Taraza, D., Henein, N. and Bryzik, W., 1999, "A Simplified Friction Model of the Piston Ring Assembly," SAE Paper 1999-01-0974.

103.) Suguru, S., Masanao, S, Takiguchi, M., Ushijima, K. and Aoyama, S., 2002, "Development of a Small LIF System for Oil Film Thickness Measurement," Proceedings of the 2002 Fall Technical Conference of the ASME Internal Combustion Engine Division, September 2002, New Orleans, Louisiana, Paper No.: ICEF2002-527, pp. 437-443.

104.) Sui, P.C. and Ariga, S., 1993, "Piston Ring Pack Friction and Lubrication Analysis of an Automotive Engine Using a Mixed Lubrication Model," SAE Paper 931937.

105.) Sun, D.C., 1990, "A Subroutine Package for Solving Slider Lubrication Problems," ASME *J. of Tribology*, Vol. 112, January, p. p. 84-91.

106.) Sun, D.C., 1991, "A Thermal Elastica Theory of Piston-Ring and Cylinder-Bore Contact," ASME *J. of Applied Mechanics*, Paper No. 91-APM-8.

107.) *Surface Texture 2000,* Handbook of Wagner's Gage Application Training, Orion, Michigan.

108.) Suzuki, T., Fujimoto, Y., Ochiai, Y., and Fujimura, I., 1987, "A Numerical Study on Piston Slap in Diesel Engine," *JSME Transactions*, Series B, Vol. 53, No. 492, pp. 2610-2618.

109.) Takiguchi, M., Nakayama, K., Furuhama, S., and Yoshida, H., 1998, "Variation of Piston Ring Oil Film Thickness in an Internal Combustion Engine," SAE Paper 980563.

110.) Takiguchi, M., Sasaki, R., Takahashi, I., Ishibashi F., Furuhama, S., Kai, R., and Sato, M., 2000, "Oil Film Measurement and Analysis of a Three Ring Pack in an Operating Diesel Engine," SAE Paper 2000-01-1787.

111.) Taylor, R.I., Brown, M.A., Thompson, D.M. and Bell, J.C., 1994, "The Influence of Lubricant Rheology on Friction in the Piston Ring Pack," SAE Paper 941981.

112.) Tian, T., Noordzij, L.B., Wong, V.W. and Heywood, J.B., 1996, "Modeling Piston-Ring Dynamics, Blowby, and Ring-Twist Effects," ASME 1996 Fall Technical Conference, ICE-Vol. 27-2, Vol. 2, pp. 67-80.

113.) Tian, T., Wong, V.W. and Heywood, J.B., 1996, "A Piston Ring-Pack Film Thickness and Friction Model for Multigrade Oils and Rough Surfaces," SAE Paper 962032.

114.) Tian, T., Rabute, R., Wong, V.W. and Heywood, J.B., 1997, "Effects of Piston-Ring Dynamics on Ring/Groove Wear and Oil Consumption in a Diesel Engine," SAE Paper 970835.

115.) Tian, T. and Wong, V. W., 1998, "Modeling the Lubrication, Dynamics, and Effects of Piston Dynamic Tilt of Twin-Land Oil Control Rings in Internal Combustion Engines," ASME 1998 Fall Technical Conference, Paper No. 98-ICE-130, pp. 9-21.

116.) Tian, T., Wong, V.W. and Heywood, J.B., 1998, "Modeling the Dynamics and Lubrication of Three Piece Oil Control Rings in Internal Combustion Engines," SAE Paper 982657.

117.) Ting, L.L. and Mayer, J.E., 1973, "Piston Ring Lubrication and Cylinder Bore Wear Analysis. Part I - Theory," ASME *J. of Lubrication Technology*, Vol. 96, pp. 305-314, Paper No. 73-Lub-25.

118.) Ting, L.L. and Mayer, J.E., 1973, "Piston Ring Lubrication and Cylinder Bore Wear Analysis. Part II - Theory Verification," ASME *J. of Lubrication Technology*, Vol. 96, Paper No. 73-Lub-27.

119.) Ting L.L., 1980, "Lubricated Piston Rings and Cylinder Bore Wear," ASME Wear Control Handbook, p. p. 609-665, ASME Publication, New York.

120.) Ting, L.L., 1980, "Development of a Laser Fluorescence Technique for Measuring Piston Ring Oil Film Thickness," *J. of Lubrication Technology*, Vol. 102, pp. 165.

121.) Ting, L.L., 1985, "A Review of Present Information on Piston Ring Tribology," SAE Paper 852355.

122.) Tripp, J.H., 1983, "Surface Roughness Effects in Hydrodynamic Lubrication: The Flow Factor Method," ASME *J. of Lubrication Technology*, Vol. 105, July, pp. 458-465.

123.) Treuhaft, M.B., Iddings, F.A., Boyd, G.A. and Sprague, S.R., 1994, "The Use of Radioactive Tracer Technology in Studying Lubricant Chemistry to Enhance Bearing and Ring Wear Control in an Operating Engine," SAE Paper 941982.

124.) Ungar, E. E. and Ross, D., 1965, "Vibration and Noise Due to Piston Slap in Reciprocating Machinery," *J. Sound Vibration*, Vol. 2, pp. 132-146.

125.) Wahiduzzaman, S., Deribar, R. and Dursunkaya, Z., 1992, "A Model for Evaporative Consumption of Lubricating Oil in Reciprocating Engines," SAE Paper 922202.

126.) Wilhoit, R.C., and Zwolinski, B.J., 1971, "Handbook of Vapor Pressures and Heat of Vaporization of Hydrocarbons and Related Compounds," Texas A&M University, College Station, Texas, USA.

127.) Wing, R.D., and Saunders, O., 1972, "Oil Film Temperature and Thickness Measurements on the Piston Rings of a Diesel Engine," Tribology and Combustion Engines Groups, *Proc. Inst. Mech. Engrs.*, Vol. 186.

128.) Wochni, G, 1979, "Determination of Local Heat Transfer Coefficients at the Piston of a High Speed Diesel Engine by Evaluation of Measured Temperature Distribution," SAE Paper 790834.

129.) Wong, V.W., Tian, T., Lang, H., Ryan, J.P., Sekiya, Y., Kobayashi, Y., and Aoyama, S., 1994, "A Numerical Model of Piston Secondary Motion and Piston Slap in Partially Flooded Elastohydrodynamic Skirt Lubrication," SAE Paper 940696.

130.) Wu, H. and Chiu, C., 1986, "A Study of Temperature Distribution in a Diesel Piston - Comparison of Analytical and Experimental Results," SAE Paper 861278.

131.) Yun, J.E., Chung, Y.C., Chun, S.M. and Lee, K.Y., 1995, "An Application of Simplified Average Reynolds Equation for Mixed Lubrication Analysis of Piston Ring Assembly in an Internal Combustion Engine," May, SAE Paper 952562.

132.) Zhang, Y., Chen, G. and Li, B., 1999, "Two Dimensional Numerical Analysis of Piston Ring Lubrication of an Internal Combustion Engine," SAE Paper No. 1999-01-1222.

133.) Zhu, D. Cheng, H.S., Arai, T. and Hamai, K., 1992, "A Numerical Analysis for Piston Skirts in Mixed Lubrication - Part I: Basic Modeling," ASME *J. of Tribology*, Vol. 114, July, pp. 553-562.

134.) Zhu, D. Hu, Y., Cheng, H.S., Arai, T. and Hamai, K., 1993, "A Numerical Analysis for Piston Skirts in Mixed Lubrication - Part II: Deformation Considerations," ASME *J. of Tribology*, Vol. 115, January, pp. 125-133.